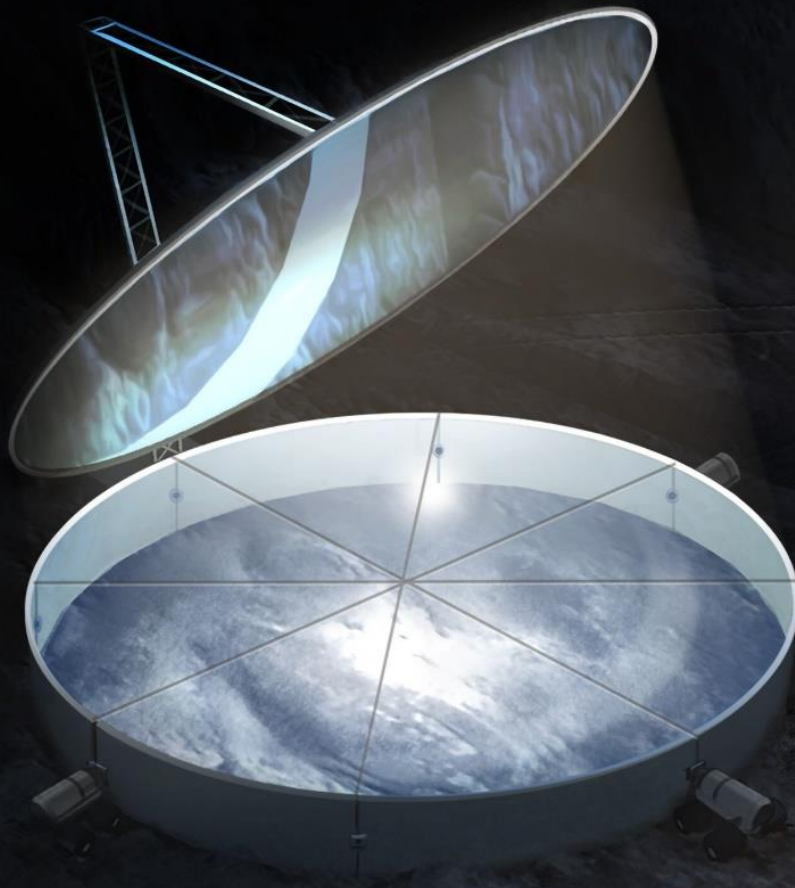


Thermal Mining of Ices on Cold Solar System Bodies



NIAC Phase I Final Report

February 2019

George Sowers

Purpose

This is the final report of the NASA Innovative Advanced Concepts (NIAC) Phase I study: *Thermal Mining of Ices on Cold Solar System Bodies*. It is submitted as partial fulfillment of the obligations of the Colorado School of Mines (CSM) under grant number 80NSSC19K0964.

Table of Contents

	List of Figures	5
	List of Tables	9
1.0	Executive Summary	10
2.0	Introduction	15
3.0	Solar System Survey of Thermal Mining Targets	18
3.1	Potential Thermal Mining Targets	19
3.2	Thermal Mining Beyond the Moon	32
4.0	Thermal Mining Mission Context: Lunar Polar Ice Mining	34
4.1	Lunar Polar Ice Distribution Analysis	36
4.2	System Architecture	39
4.3	Functional Analysis	42
4.4	Ice Extraction Subsystem	46
4.5	Power Subsystem	53
4.6	Deployment and Setup	55
4.7	Operations	59
4.8	Mass and Cost Estimates	66
4.8.1	Subsystem Mass Estimates	66
4.8.2	Total Mass	70
4.8.3	Subsystem Cost Estimates	71
4.8.4	Total Cost	74
4.9	Business Case Analysis	76
4.9.1	The Propellant Market	76
4.9.2	Business Case Scenarios	80
4.9.3	Business Case Results	83
4.9.4	Comparison to Previous Analysis	87
5.0	Proof of Concept Testing	91
5.1	Testing Objectives and Approach	91
5.2	Icy Regolith Simulants	91
5.3	Block 1 Testing	95
5.3.1	Block 1 Apparatus	95
5.3.2	Block 1 Methodology	96
5.3.3	Block 1 Results	97
5.4	Block 2 Testing	105
5.4.1	Block 2 Apparatus	105
5.4.2	Block 2 Methodology	105
5.4.3	Block 2 Results	105
5.5	Test Conclusions	106
6.0	Summary and Conclusions	115
6.1	Bulletized Summary	115
6.2	Conclusions	116
6.3	Recommendations for Future Work	118
7.0	References	121
8.0	Appendix A: Solar System Catalogue	129
9.0	Appendix B: Acronym List	132

Acknowledgements

This report was prepared by George Sowers, Ross Centers, David Dickson, Adam Hugo, Curtis Purrington, and Elizabeth Scott. It was reviewed by Chris Dreyer and Angel Abbud-Madrid. Cover art is by Matt Olson showing the ice extraction system in a lunar permanently shadowed region (PSR).

List of Figures

1.0 Executive Summary

Figure 1.1. Ice extraction on the Moon.	10
Figure 1.2. The inner solar system.	11
Figure 1.3. Ice extraction system concept.	12
Figure 1.4. CSM medium cryo-vacuum chamber.	13

2.0 Introduction

Figure 2.1 Moving from exploration results to a proven reserve. CRIRSCO, 2012.	15
Figure 2.2. Heat applied to an icy regolith simulant sample under cryogenic vacuum conditions.	16
Figure 2.3. Thermal Mining based ice extraction system on the Moon.	17

3.0 Solar System Survey of Thermal Mining Targets

Figure 3.1. The inner and outer Solar System.	18
---	----

3.1 Potential Thermal Mining Targets

Figure 3.2. Mercury, with detected water ice in yellow.	19
Figure 3.3. Mars, widespread glacial ice in blue, detected by MRO radar passes in yellow.	20
Figure 3.4. Mars, example of steep scarps with visible water ice.	20
Figure 3.5. Comet 67P (top right), close-up of two areas of exposed water ice (bottom left).	21
Figure 3.6. 24 Themis, approx. orbit of asteroid (red).	22
Figure 3.7. Ceres, approx. true-color image.	22
Figure 3.8. 65 Cybele, approx. orbit of asteroid (blue).	23
Figure 3.9. Ganymede, surface and subsurface layers, visualized.	23
Figure 3.10. Calisto, approx. true-color image.	24
Figure 3.11. Europa, side view of ice and hydrothermal vents.	24
Figure 3.12. Jupiter Trojans, two groups of Trojan objects (green).	24
Figure 3.13. Titan, exposed water ice on the surface (blue).	25
Figure 3.14. Iapetus, leading hemisphere (left), trailing hemisphere (right).	25
Figure 3.15. Dione, trailing hemisphere (left), leading hemisphere (right).	26
Figure 3.16. Tethys, trailing hemisphere (left), leading hemisphere (right).	26
Figure 3.17. Enceladus, side view of ice and hydrothermal vents.	27
Figure 3.18. Mimas, image of moon (left), heat map of daytime temperatures (right).	27
Figure 3.19. Phoebe, the irregular moon.	28
Figure 3.20. Hyperion, seen here with its porous and sponge-like exterior.	28
Figure 3.21. Chariklo, Hubble Space Telescope image of the largest centaur.	28
Figure 3.22. Titania, Voyager 2 image of the largest moon of Uranus.	29
Figure 3.23. Triton, Voyager 2 image of the largest moon of Neptune.	29
Figure 3.24. Relative locations of Neptune's L4 and L5 Trojans.	30
Figure 3.25. Relative sizes, colors, and albedos for some of the large Trans-Neptunian objects.	30
Figure 3.26. Orcus & moon Vanth, Hubble Space Telescope image of the dwarf planet Orcus (center) and its moon (center-bottom).	31

Figure 3.27. Pluto & moon Charon, image of Pluto (left), enlarged image of Pluto's moon Charon (right).	31
Figure 3.28. Eris & moon Dysnomia, Hubble Space Telescope image of the most massive dwarf planet (center) and its moon (center-left).	32
<u>4.0 Thermal Mining Mission Context: Lunar Polar Ice Mining</u>	
Figure 4.0.1. Ice exposures at the North Pole and South Pole of the Moon.	34
Figure 4.0.2. Resource exploration (prospecting) roadmap.	35
<u>4.1 Lunar Polar Ice Distribution Analysis</u>	
Figure 4.1.1. Initial results from the CSM model.	37
Figure 4.1.2. Comparison of ice concentration vs depth for three lunar terrain types.	38
<u>4.2 System Architecture</u>	
Figure 4.2.1. High-Level Space Supply Chain.	39
Figure 4.2.2. Propellant Production Architecture.	40
Figure 4.2.3. Ice extraction concept.	41
Figure 4.2.4. Ice extraction subsystem.	41
Figure 4.2.5. IHOP Water Processing Overview (Paragon Corp.)	42
<u>4.3 Functional Analysis</u>	
Figure 4.3.1. Capture tent functional tree.	43
Figure 4.3.2. Cold trap hauler functional tree.	44
Figure 4.3.3. Secondary optics functional tree.	45
<u>4.4 Ice Extraction Subsystem</u>	
Figure 4.4.1. The Capture Tent.	46
Figure 4.4.2. Capture Tent product tree.	47
Figure 4.4.3. Capture tent legs in lowered tent (left) and raised tent (right) positions.	49
Figure 4.4.4. Cold trap hauler.	50
Figure 4.4.5. Cold trap hauler product tree.	50
Figure 4.4.6. Secondary optics.	51
Figure 4.4.7. Secondary optics product tree.	52
Figure 4.4.8. Secondary optics mirror geometry.	52
<u>4.6 Deployment and Setup</u>	
Figure 4.6.1. The Vulcan/Centaur rocket.	55
Figure 4.6.2. Centaur 5.	55
Figure 4.6.3. XEUS, the Centaur 5 stage equipped with a landing kit.	56
Figure 4.6.4. Deployment and setup sequence.	57
<u>4.7 Operations</u>	
Figure 4.7.1. Overall process flow.	59
Figure 4.7.2. Ice collection and transport flow.	59
Figure 4.7.3. Notional mining site map.	60
Figure 4.7.4. Tent placement pattern.	60
Figure 4.7.5. Ice hauler transit time.	61

Figure 4.7.6. Ice hauler duty cycle.	62
Figure 4.7.7. Tent repositioning flow.	63
Figure 4.7.8. Capture Tent and ice hauler in the towing configuration.	63
Figure 4.7.9. The capture tent being moved across the PSR.	64
<u>4.8 Mass and Cost Estimates</u>	
Figure 4.8.1. Propellant production system architecture.	66
Figure 4.8.2. Subsystem mass comparison.	71
Figure 4.8.3. Development and production cost by subsystem.	73
<u>4.9 Business Case Analysis</u>	
Figure 4.9.1. Benefits of refueling with space sourced LO ₂ /LH ₂ propellants.	77
Figure 4.9.2. ΔV map of cislunar space.	77
Figure 4.9.3. Propellant prices in cislunar space.	78
Figure 4.9.4. Propellant production program plan.	83
Figure 4.9.5. Cumulative cash for the Propellant Production Company.	84
Figure 4.9.6. Scenario 1. IRR sensitivity with propellant price and non-recurring cost.	85
Figure 4.9.7. Scenario 2. IRR sensitivity with propellant price and NASA investment.	86
Figure 4.9.8. Scenario 3. IRR sensitivity with propellant price and NASA investment.	86
Figure 4.9.9. Cumulative cash for NASA.	87
<u>5.2 Icy Regolith Simulants</u>	
Figure 5.2.1. Lunar Highlands Simulant –1 Spec Sheet, Exolith Labs.	92
Figure 5.2.2. Granular Icy Regolith Simulant, 12% Water Weight.	93
Figure 5.2.3. Sample Container submerged in LN with LN feed through.	93
Figure 5.2.4. ‘Mud Pie’ icy regolith simulant, 12% water weight.	94
Figure 5.2.5. Frost Layer Production, Simulant and Container at 77K.	94
<u>5.3 Block 1 Testing</u>	
Figure 5.3.1. Left: Adiabatic Boundary Condition, Right: Isothermal Boundary Condition.	95
Figure 5.3.2. View from Vacuum Chamber port during an adiabatic boundary test.	96
Figure 5.3.3. Mud Pie Surface Condition after a 5-hour test.	97
Figure 5.3.4. Cross-Section diagram of Mud Pie Icy Regolith physical analysis results.	98
Figure 5.3.5. Temperature profile response of various ice grain configurations at depth of 2cm with a 12wt% water.	98
Figure 5.3.6. General physical subsurface structure of granular fine simulant with isothermal boundary condition with an initial water of 5.6wt% or 12wt%.	99
Figure 5.3.7. General physical subsurface structure of granular fine simulant with adiabatic boundary condition with an initial water of 5.6wt% or 12wt%.	100
Figure 5.3.8. General physical subsurface structure of granular fine simulant, using a thermal conducting rod with adiabatic boundary condition with an initial water of 5.6wt%.	100
Figure 5.3.9. Temperature profile: 12% Granular Ice, 23-hour test, Isothermal BC.	102
Figure 5.3.10. Temperature profile: 5.6% Granular Ice, 20-hour test, Isothermal BC.	102
Figure 5.3.11. Temperature Profile: 12% Mud Pie, Adiabatic BC.	103
Figure 5.3.12. Temperature profile: 5.6% Granular, Adiabatic BC.	103

Figure 5.3.13. Temperature profile during cryogenic cooling of different icy regolith configurations.	104
<u>5.4 Block 2 Testing</u>	
Figure 5.4.1. The Block 2 testing apparatus.	105
<u>5.5 Test Conclusions</u>	
Figure 5.5.1. Granular Sublimation rates for 5.6% and 12% scaled down per cm ² , with adiabatic boundary conditions.	107
Figure 5.5.2. Lens Zone removed from a granular test.	108
Figure 5.5.3. Typical lens found in 5.6% and 12.0% granular tests.	109
Figure 5.5.4. Thermal Conductivity of Icy Regolith as a function of Temperature and Water wt%.	110
Figure 5.5.5. Water Vapor Pressure as function of Temperature, derived from Andreas, 2006.	111
Figure 5.5.6. Simple Model describing water vapor flow rate as a function of Temperature and Depth of Overburden.	112
Figure 5.5.7. Thermal Conducting Rod inserted into granular icy regolith.	113
Figure 5.5.8. Top View Thermal Conducting Rod Grid Layout.	113
Figure 5.5.9. Side View Thermal Conducting Rod Grid Layout.	114
<u>6.3 Recommendations for Future Work</u>	
Figure 6.1. Thermal Mining risk square.	119
Figure 6.2. The large (2.7 m ³) cryogenic vacuum chamber at CSM.	120
Figure 6.3. Block 3 test apparatus.	120

List of Tables

4.0 Thermal Mining Mission Context: Lunar Polar Ice Mining

Table 4.0.1. Volatiles in LCROSS Ejecta.	34
--	----

4.6 Deployment and Setup

Table 4.6.1. Deployment launch and landing campaign details.	56
--	----

4.7 Operations

Table 4.7.1. Point design assumptions.	60
--	----

Table 4.7.2. Point design derived requirements.	61
---	----

Table 4.7.3. Cold trap design parameters.	61
---	----

4.8 Mass and Cost Estimates

Table 4.8.1. Capture tent mass.	67
---------------------------------	----

Table 4.8.2. Secondary optics mass.	68
-------------------------------------	----

Table 4.8.3. Heliostat mass.	69
------------------------------	----

Table 4.8.4. Power system mass.	70
---------------------------------	----

Table 4.8.5. Subsystem masses by lunar location and total mass.	70
---	----

Table 4.8.6. Subsystem development cost estimates.	72
--	----

Table 4.8.7. Subsystem production cost estimates.	73
---	----

Table 4.8.8. Launch data.	74
---------------------------	----

Table 4.8.9. Launch costs.	74
----------------------------	----

Table 4.8.10. Propellant production system non-recurring cost.	75
--	----

Table 4.8.11. Propellant production system non-recurring cost.	75
--	----

4.9 Business Case Analysis

Table 4.9.1. Benefits of lunar-sourced propellants.	78
---	----

Table 4.9.2. Propellant demand and price.	82
---	----

Table 4.9.3. Key business case parameters.	84
--	----

Table 4.9.4. Thermal Mining comparison with Charania and DePasquale (2007).	88
---	----

Table 4.9.5. Thermal Mining comparison with Jones et al., (2019).	90
---	----

5.2 Icy Regolith Simulants

Table 5.2.1. Granular Ice Grain Distributions.	92
--	----

Table 5.2.2. Granular simulant water weight % vs density.	93
---	----

5.3 Block 1 Testing

Table 5.3.1. Mud Pie Results.	97
-------------------------------	----

Table 5.3.2. Comparison of Granular Ice Grain sizes (12% Water weight).	98
---	----

Table 5.3.3. Granular Icy Regolith Tests Results (Fine).	99
--	----

Table 5.3.4. Thermal Conducting Rod Test Results.	100
---	-----

Table 5.3.5. Frost Layer Test Results.	101
--	-----

Table 5.3.6. Ice Distribution Data.	101
-------------------------------------	-----

6.3 Recommendations for Future Work

Table 6.1. Top Thermal Mining Risks.	118
--------------------------------------	-----

1.0 Executive Summary



Figure 1.1. Ice extraction on the Moon. Secondary optics, capture tent and ice hauler. Art by Matt Olson.

Volatiles such as water and methane are key to the sustainability of space exploration and will underpin most economic activities in space. Volatiles are essential for life and can be used as rocket propellants. Volatiles are common throughout the solar system, existing in many places, often in the form of ices, frozen on cold bodies. Developing sources of volatiles in space will dramatically lower the cost of exploration and enable robotic and human spaceflight missions not currently possible and/or affordable.

Extracting volatiles from cold solar system bodies will be challenging. Traditional excavation methods require heavy machinery capable of operating in extreme cold, vacuum and dust exposure. Small bodies entail very low gravity. Excavation approaches will be costly to build, deploy and maintain. However, direct heating of volatile bearing materials via Thermal Mining can save the cost and weight of excavation systems as well as eliminate most of the active components of the system, enhancing reliability and maintainability.

Thermal Mining applies heat directly to frozen volatile bearing materials to allow extraction of the volatile without the cost, mass and complexity of excavation. Heat is applied directly to the surface in the form of redirected sunlight or subsurface via conducting rods or heaters emplaced in boreholes. Vapor is captured within a tent-like structure and refrozen in cold traps for processing. Our mission context applies this concept to the extraction of water-ice from permanently shadowed regions near the poles of the Moon. The Moon is the closest and most accessible source of resources beyond Earth. This was eloquently stated by the late John

Marburger, Science Advisor to US President George W. Bush, in a speech to the 2006 Goddard Symposium [Marburger, 2006]:

The Moon has unique significance for all space applications for a reason that to my amazement is hardly ever discussed in popular accounts of space policy. The Moon is the closest source of material that lies far up Earth's gravity well. Anything that can be made from lunar material at costs comparable to Earth manufacture has an enormous overall cost advantage compared with objects lifted from Earth's surface. The greatest value of the Moon lies neither in science nor in exploration, but in its material.

Utilization of the Moon's resources, especially the polar water ice for propellant, will dramatically reduce the cost of exploring and developing cislunar space and the rest of the solar system.

This report documents the work performed by the Colorado School of Mines (CSM) under the Phase I NASA Innovative Advanced Concepts (NIAC) grant titled *Thermal Mining of ices on cold solar system bodies*. The activities performed as part of this study were organized into three main tasks. Task 1 was a survey of the solar system to identify promising targets for Thermal Mining. Task 2 was the development of an architecture to apply Thermal Mining to extracting water ice from the permanently shadowed regions (PSRs) near the lunar poles. Task 3 was proof of concept testing of the effectiveness of direct heat in sublimating ice from within icy regolith simulant samples.

One of the great discoveries of planetary science over the past few decades is that water ice and other frozen volatile materials are ubiquitous in the solar system. We performed a comprehensive survey of the solar system to identify potential targets for Thermal Mining. Our emphasis was the inner solar system (Figure 1.2) due to proximity and likelihood to be utilized in the next several decades. We developed a detailed catalogue of these bodies capturing attributes such as possibility of surface or near-subsurface ices, accessibility, gravitational acceleration, distance from the sun and many others.

Besides the Moon which is the subject of Task 2, some of the most promising Thermal Mining targets are Mars, Ceres and the asteroids 24

Themis and 65 Cybele. Recent discoveries have revealed Mars to be rich in water ice resources. Surface ice exists near the poles and there are near-surface glacial sheets in the mid latitudes. Ceres is the largest object in the main asteroid belt and is classified as a dwarf planet. Unambiguous evidence exists of water ice at or near the surface. Ceres releases 6kg per second of water vapor,

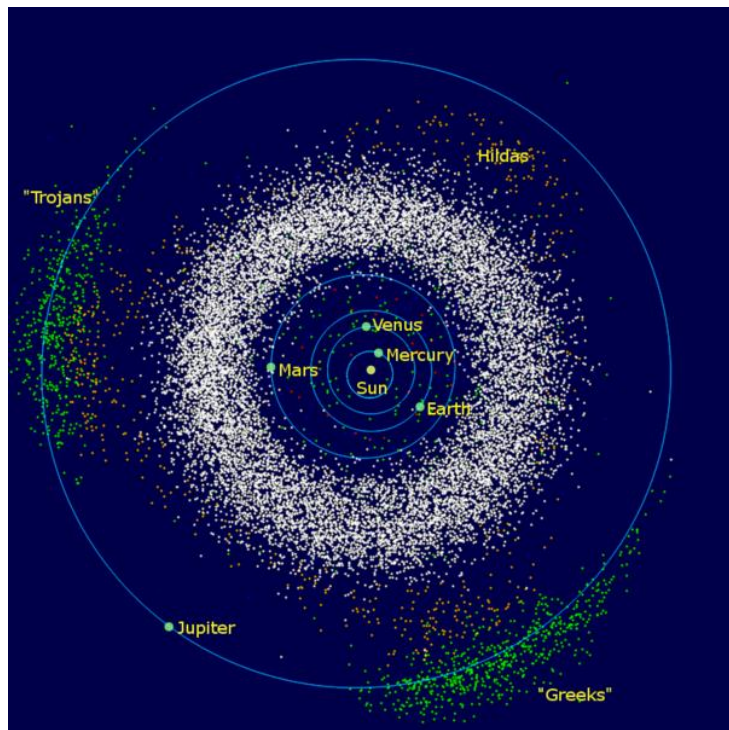


Figure 1.2. The inner solar system. Wikipedia.

originating from localized mid-latitude surface sources. The main belt asteroid 24 Themis is extremely intriguing. The surface of the asteroid appears to be completely covered in ice. As this ice layer sublimates, it may be getting replenished by a reservoir of ice under the surface. Organic compounds have also been detected on the surface. The main belt asteroid 65 Cybele also has indications of surface ice.

In addition to these promising targets within the inner solar system, many of the moons of Jupiter (Ganymede, Calisto, Europa), Saturn (Titan, Rhea, Iapetus, Dione, Tethys, Enceladus) and Neptune (Triton, Nereid) appear to be covered in ices. These bodies are difficult to access due to the gravitation attraction of their host planets, but can be utilized as fuel sources in the more distant future. Finally, Pluto, its moons and nearly every object in the Kuiper belt appears to harbor ice of some form. The solar system is rich in ices. Low cost, reliable methods to extract this ice, like Thermal Mining, will be a cornerstone of future space exploration development and settlement. Details of our solar system survey are discussed in Section 3 and Section 8 (Appendix A) contains our detailed catalogue.

The closest source of water ice and other frozen volatiles beyond Earth is the Moon. There is increasing evidence that water ice exists in the lunar PSRs on or near the surface. Task 2 of our study developed a detailed architecture for the Thermal Mining of water ice in the PSRs near the lunar poles. The lunar Thermal Mining system is at the front end of an in-space supply chain for propellant, purified water, oxygen and other commodities. The overall architecture consists of many elements: extraction, processing, distribution, storage and delivery to the customer. A space architecture based on space sourced materials dramatically lowers the cost of almost every space activity beyond low Earth orbit by eliminating the need to deliver materials from Earth.

The Thermal Mining ice extraction system (Figures 1.1 and 1.3) uses heat from reflected sunlight directed into the PSR by heliostats mounted near the crater rim to warm the icy regolith, sublimating the ice and releasing it in the form of vapor. If surface heating is insufficient, subsurface heating can be accomplished by driving conducting rods into the subsurface. The ice extraction system consists of three subsystems: the Capture Tent, the secondary optics and the cold trap/ice hauler assemblies. The secondary optics consists of a large flat elliptical mirror that receives sunlight from heliostats at the crater rim and redirects it to the lunar surface. The Capture Tent is a large cylindrical structure, with openings 90 degrees apart around the circumference to allow for the passage of sublimated vapor into the cold traps. The cold trap is a cylindrical aluminum tank mounted to an ice hauler vehicle.

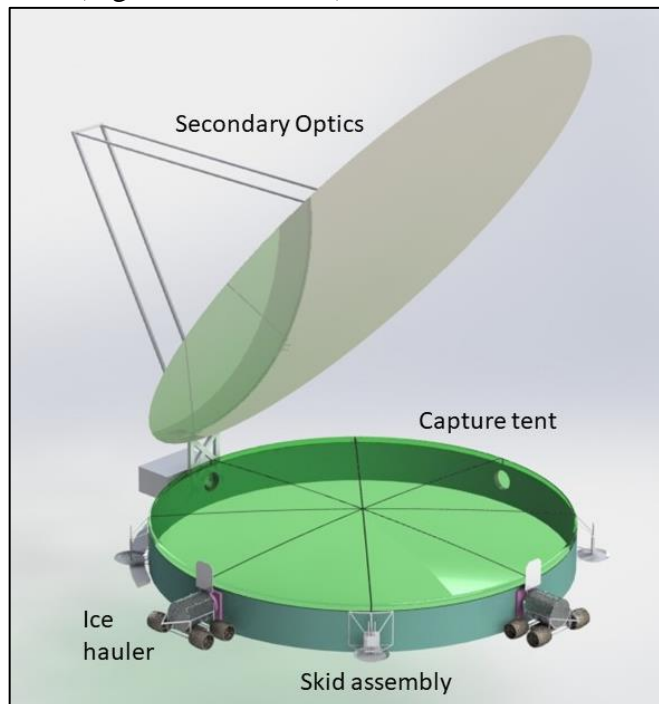


Figure 1.3. Ice extraction system concept.

The ice extraction system is positioned over the ice field and the heliostats and secondary optics are positioned. Heating begins driving sublimation and ice collection in the cold traps. When the cold traps are full, they detach and travel to the processing facility where they unload their ice and recharge batteries. Once the icy regolith under the Capture Tent has been depleted, the ice extraction system is moved to a new location, assumed to be adjacent to the previous location.

In addition to the design and operations concepts detailed above, we have also developed initial mass estimates for the ice extraction system and the overall propellant production system. These mass estimates enabled us to develop a preliminary deployment plan as well as estimate costs for development, production and launch/landing. The propellant production facility weighs a bit over 26 tons, produces 1100 tons of propellant per year, and can be developed and deployed to the Moon for around \$2.5B. A preliminary business case shows that positive returns can be generated based on both commercial and government demands for propellant assuming a productive life of the operation of at least 10 years. Details of the evidence for ice on the Moon, our analysis of the formation and evolution of this ice, the lunar propellant production system architecture, the ice extraction system, deployment to the Moon, the operations concept, mass and cost estimates and the business are all described in Section 4.

Entering into the study, the most significant risks to the success of Thermal Mining on the Moon were the nature of the icy regolith and the effectiveness of the various heating methods in sublimating requisite amounts of ice. We have mitigated these risks through a test program where we created a number of icy regolith simulants and tested the effectiveness of surface heating under cryogenic vacuum conditions.

The first step was to create icy regolith simulants deemed to be representative of what we may encounter on the Moon. Investigations into the nature of icy regolith on the Moon led us to develop the granular mix simulant. This simulant is created by shaving block ice, sieving the shavings into small grains and then mixing the grains with dry regolith. The result is a sand-like material where some of the grains are regolith and some are ice. Though a few tests were conducted with other simulant types, most of our testing focused on the granular mix.

The majority of our testing during the Phase I study relied on the Block 1 test apparatus. This apparatus held a small coffee cup sized sample of simulant in a liquid nitrogen bath. The sample was placed into the CSM medium vacuum chamber shown in Figure 1.4. A lamp, sized to produce one sun of flux, then illuminated the surface of the sample. Dwell times were varied up to a maximum of 23 hrs. At the conclusion, the sample was removed and weighed. The difference in weight is



Figure 1.4. CSM medium cryo-vacuum chamber.
Graduate student Curtis Purrington.

representative of the amount of ice sublimated during the test.

Although we are seeing measurable ice yield from just surface heating, the yield is limited by two phenomena, one an artifact of our apparatus, the other potentially representative of the actual lunar situation. First, the small size of our sample brings the liquid nitrogen bath very close to the heat source. Much of the applied heat is thus boiling nitrogen, not sublimating ice. This situation will be corrected by the Block 2 test configuration with a larger sample size relative to the lamp size. Although we have designed and fabricated the Block 2 test apparatus, testing will take place in the future. Second, heating creates a desiccated layer at the top of the sample that inhibits heat conduction into the sample and blocks vapor flow to the surface. To mitigate this effect, we developed a hollow, perforated conducting rod. Use of the conducting rod improved ice yields by a factor of 2-3 in the Block 1 test configuration. Our test program is discussed in detail in Section 5.

Our Phase I NIAC activities have developed a catalogue of Thermal Mining targets throughout the solar system, developed a detailed concept for ice extraction within a lunar PSR and mitigated the most critical risk, sublimation via surface heating. Based on our results, the Thermal Mining method has enormous promise for the development some of the most valuable resources in the solar system.

In the near term, this method is applicable—even profitable—for developing the water-ice resources of the Moon, the first economically viable space resource and the key to unlocking the remainder of the solar system. The efficiency of Thermal Mining far exceeds any method based on excavation. This high efficiency is gained by targeting surface ice, using reflected sunlight and avoiding excavation. The use of commercial methods, a highly efficient commercial transportation system and a public Private Partnership (PPP) business model also result in much lower costs. Of course, much work remains to retire the risks inherent in Thermal Mining on the Moon. But the promise is astounding: tens of billions of dollars in savings for the Moon to Mars program and opening up the Moon and cislunar space to economic development, delivering trillions of dollars into Earth's economy.

Our study conclusions are outlined in Section 6.

2.0 Introduction

Volatiles such as water and methane are key to the sustainability of space exploration and will underpin most economic activities in space. Volatiles are essential for life and can be used as rocket propellants, breaking the tyranny of the rocket equation. Volatiles are common throughout the solar system, existing in many forms such as ices frozen on cold bodies. Developing sources of volatiles in space will dramatically lower the cost of exploration and enable robotic and human spaceflight missions not currently possible and/or affordable.

Water, in particular, is ubiquitous in the inner solar system. It exists on Mercury, the Moon, many asteroids and Mars. Recent findings [Li, et. al. 2018] indicate water ice is present on the surface of the Moon within the permanently shadowed regions (PSRs) in concentrations up to 30% by mass. The presence of rich ice deposits on Earth’s nearest extraterrestrial neighbor is a potential game changer in the exploration and development of the solar system.

Water has many uses in the context of space exploration and development. It is essential for human life and agriculture. Oxygen, one of its constituents, is a necessary component of breathing air. It is one of the most effective substances for radiation shielding on a per mass basis. But perhaps its most valuable use is as rocket propellant. It can be used directly in the form of steam or plasma for low to medium thrust application. When split into hydrogen and oxygen and liquefied, it produces LO₂ and LH₂, the most efficient chemical propellants known. *Water is truly the oil of space.* And like oil on Earth, water will be the foundation of the space economy.

Our knowledge of extraterrestrial volatile resources is based on several decades of truly impressive scientific space missions. But we are a long way from being able to characterize any space resource as a proven reserve with quantifiable economic benefit. The process of moving from a scientific indication of a resource to a proven mineral reserve is well established by the terrestrial mining industry. As shown in Figure 2.1, developed by the Committee for Mineral Reserves International Reporting Standards (CRIRSCO, 2012), there are two dimensions. The vertical dimension corresponds to increased geologic knowledge and confidence. This knowledge is a prerequisite to developing any space resource and is gained through a resource exploration campaign. The horizontal dimension embodies the modifying factors, one of which is extraction (mining) technology.

Adapting the proven technologies of terrestrial extractive industries may prove challenging or have limited utility. For example, the terrestrial mining industry employs massive machines, which often depend on Earth’s high gravity for mechanical force and are impractical to be

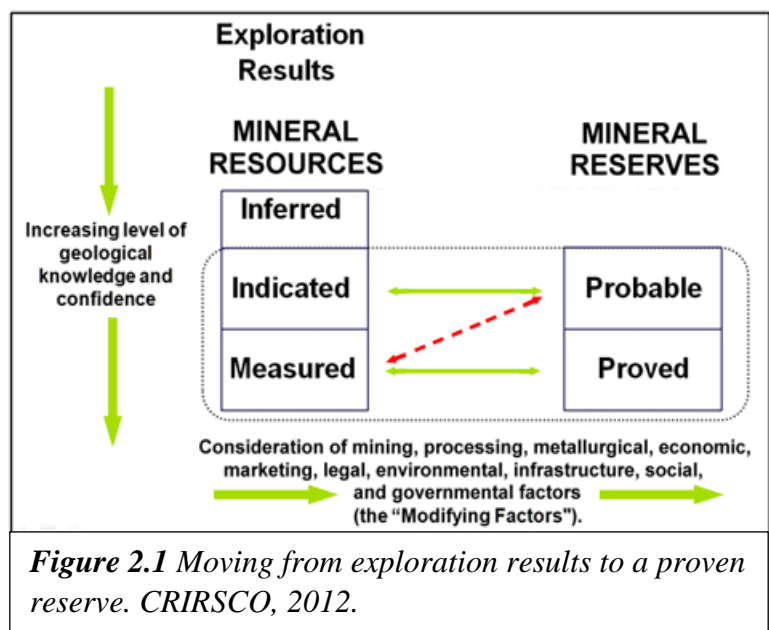


Figure 2.1 Moving from exploration results to a proven reserve. CRIRSCO, 2012.

launched into space. The extractive techniques of the oil and gas industries are uniquely tuned to the geology of the Earth and the nature of fossil fuel deposits, conditions which are unlikely to be found elsewhere in the solar system.

To make progress in space resources, we must find new methods and look for other analogies to adapt terrestrial technologies. One such analogy comes from the terrestrial environmental remediation industry. In particular, the method of thermal desorption [Foster Wheeler, 1998] shows promise for the extraction of an important class of space resources, volatile materials frozen in the form of ices often mixed with non-volatile rocky materials. In the environmental remediation application, thermal desorption uses heat to increase the volatility of contaminants so they can be removed from a solid matrix, often soil. Our proposed technique of Thermal Mining will use heat to extract useful volatiles for processing and utilization for space exploration or space commerce.

The most promising techniques for Thermal Mining are those that apply heat in-situ to the volatile bearing material. This avoids the cost, mass and complexity of the more traditional excavation methods. A recent study [Sowers & Dreyer, 2019] indicates a 65% mass savings for in-situ Thermal Mining compared

to excavation for the lunar application. The effectiveness of direct heat in sublimating ice from within icy regolith samples has been demonstrated during our NIAC Phase I study, *proving that Thermal Mining can work*. Figure 2.2 shows heat in the form of simulated sunlight being applied to an icy regolith simulant sample under cryogenic vacuum conditions in our laboratory at the Colorado School of Mines (CSM).

During our NIAC Phase I investigations, we identified many bodies throughout the solar system where Thermal Mining can be applied. This will be discussed in Section 3. We also developed an architecture for Thermal Mining in the permanently shadowed regions (PSRs) of the Moon, discussed in Section 4. Using proven system engineering processes, we developed a functional and physical architecture for a LO₂/LH₂ propellant production system anchored by a Thermal Mining based ice extraction system. Figure 2.3 shows an artist's concept of our ice collection concept on the Moon. We performed operations analysis to derive requirements for the industrial scale production of propellant and developed a design concept for the ice extraction system. Most importantly, we developed simulants of icy lunar regolith and demonstrated the effectiveness of direct heat in sublimating ice from the simulants under cryogenic vacuum conditions, discussed in Section 5. These critical proof of concept experiments demonstrate that Thermal Mining on the Moon is feasible, opening the way to low cost sources of water and



Figure 2.2. Heat applied to an icy regolith simulant sample under cryogenic vacuum conditions.

propellant for future lunar exploration and development. Finally, Section 6 summarizes our work, presents the major conclusions, and provides recommendations for future work.

Our overarching goal is to develop a roadmap for the implementation of Thermal Mining on the Moon, including the requisite technology development, to enable NASA or commercial companies to plan for full scale production of propellant within a decade.

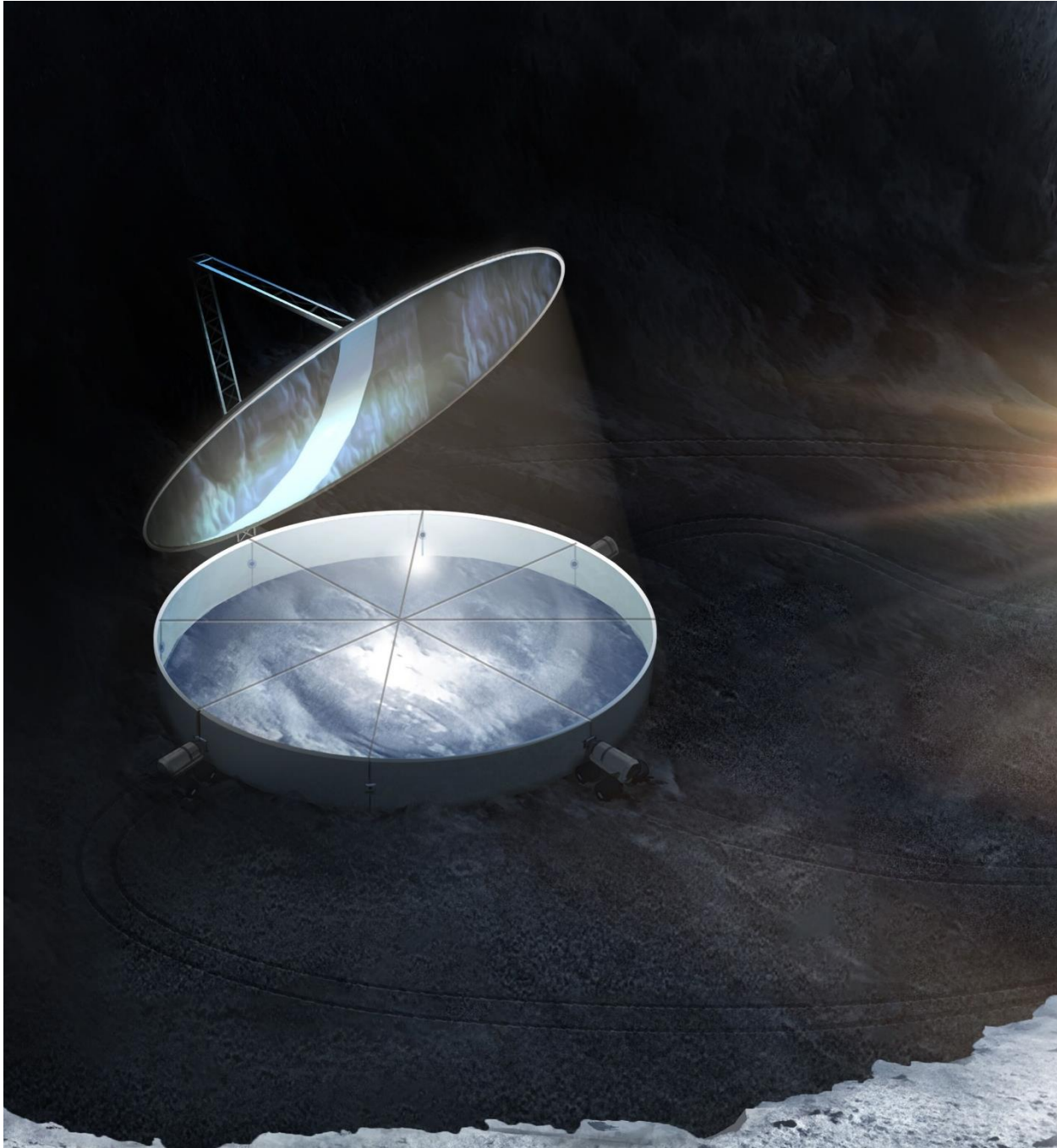


Figure 2.3. Thermal Mining based ice extraction system on the Moon. Art by Matt Olson.

3.0 Solar System Survey of Thermal Mining Targets

The Solar System is rich in volatile resources potentially amenable to extraction using one of the many possible variations of the Thermal Mining technique. The inner Solar System, outer Solar System, and beyond each contain an enormous number of potential targets (Figure 3.1). The objective of this Solar System survey is to identify objects beyond Earth’s Moon that would make good targets for Thermal Mining.

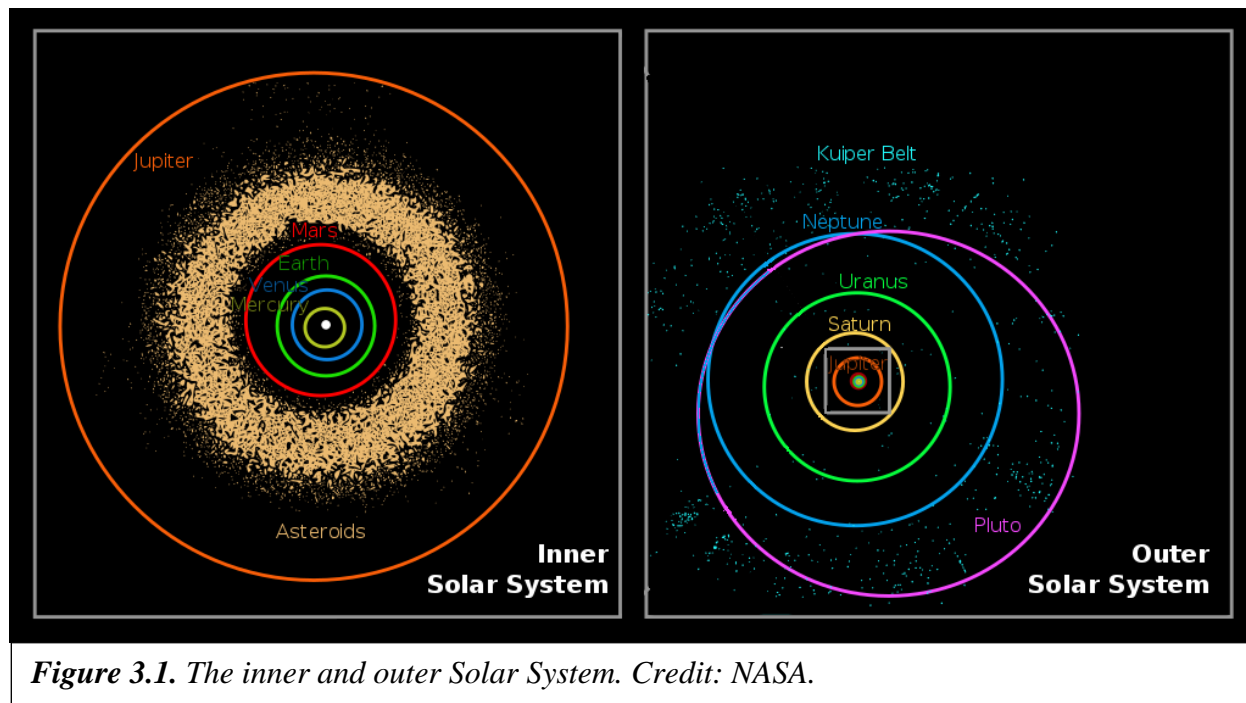


Figure 3.1. The inner and outer Solar System. Credit: NASA.

Because Thermal Mining is best utilized to extract volatiles from ice, the Solar System survey looked for objects containing water ice at their surface. Hydrated minerals can also contain water, but they were not the focus of this survey. Material covered in this survey is extensive but not comprehensive and it should be noted that future discoveries will lead to both additional Thermal Mining targets and a better understanding of the identified prospects.

Our survey reviewed literature about most Solar System objects including planets, moons, comets, trojans, centaurs, asteroids, and Kuiper belt objects. Due to the vast number of objects, more focus was given to larger objects while smaller objects were analyzed as groups. Over the course of the survey, a table of data on objects was created which includes object characteristics that may be useful for future analysis (See Section 8, Appendix A). Future analysis of objects where Thermal Mining is feasible will utilize the collected data for individual analysis and comparison. Due to the large number of objects this data is not comprehensive but will be built on in future work. The database contains objects not currently identified as containing water ice. This is because future data may reveal the presence of ices.

For each potential target, we performed an initial assessment of the presence of ice. The assessment included research on many Solar System objects in addition to planets and the largest moons. There are a huge number of bodies that exist in the main asteroid belt, as small moons of planets beyond Mars, as trojans, or in the Kuiper belt and beyond. In cases where these large

groups of smaller objects didn't have direct measurements or high detail information they were treated as groups for analysis. The assessment noted cases where groups were found to have high ice content, and cases where small objects have had direct measurements of ice.

The assessment of Thermal Mining viability first focused on whether an object has confirmed water ice. After ice was confirmed, details relevant to Thermal Mining were studied to determine an order of priority for future study. The factors given priority were energy required for landing on and transiting to the object and distance from Earth. Economic activities in space, that would justify development of early Thermal Mining operations, are expected to first involve the Earth-Moon, and potentially Earth-Mars regions. Due to this, objects with water ice nearest Earth and Mars are given priority. While many objects don't fit that criteria, future activity in those regions would shift priority.

The availability of sunlight was not used as criteria for judging Thermal Mining viability. This is because Thermal Mining technology can be adapted to utilize other sources of thermal energy, such as chemical or nuclear. Objects effected by this consideration reside in the outer Solar System, reducing their priority for that reason. Most near-term Thermal Mining research will focus on objects with more available solar energy. As objects further from the Sun become a higher priority, the development of Thermal Mining systems optimized for more distant objects with less sunlight will become an important focus.

3.1 Potential Thermal Mining Targets

Mercury

The MESSENGER spacecraft detected water in north pole permanently shadowed regions of Mercury (Figure 3.2). A layer observed as tens of centimeters thick is believed to be ice, which is covered by a layer of another material 10-30 centimeters thick. Based on observations it has been inferred that Mercury's polar shadowed craters contain 2×10^{15} kilograms of water [Lawrence, et. al. 2013].

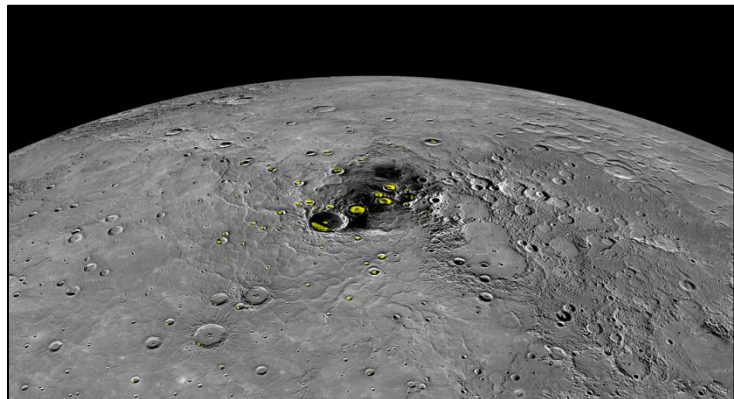


Figure 3.2. Mercury, with detected water ice in yellow. Credit: NASA.

The planet Mercury is almost always further from Earth than Mars at opposition and has a similar gravitational field of roughly 3.7 m/s^2 [Mazarico, et. al. 2014]. The planet also has no atmosphere to help with landing. All these

factors mean both transit from Earth and Entry, Descent, and Landing (EDL) is propulsively expensive. Mercury's ice will likely be an important component to support future activity on its surface, but because no significant surface activity is planned, it is not a priority for Thermal Mining system development.

Mars

There is widespread evidence of water ice on Mars from multiple spacecraft. Both the north and south poles have exposed water ice of extreme purity [Grima, et. al. 2009, Titus, et. al. 2003]. However, not just the poles of Mars have water ice; it is also found in mid-latitude regions where human exploration and habitation is likely to occur. The Shallow Radar instrument on the Mars Reconnaissance Orbiter (MRO) has observed widespread deposits of glacial ice in the mid-latitudes of Mars (Figure 3.3).

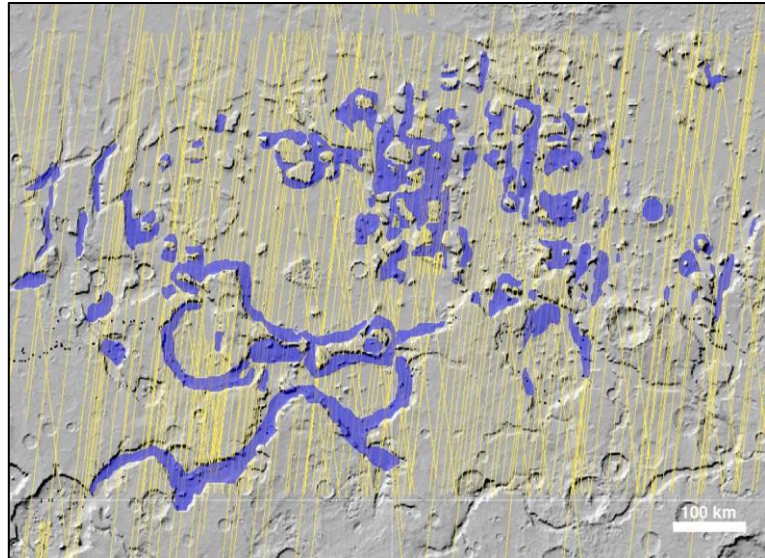


Figure 3.3. Mars, widespread glacial ice in blue, detected by MRO radar passes in yellow. Credit: NASA.

Follow up analysis with the HiRISE instrument on MRO has found eight locations where ground ice is visible as steep scarps (Figure 3.4). Some of these water ice scarps are over 100 meters thick, revealed by erosion. In many of these locations the top of the scarp is within one meter of the surface meaning ice begins at those shallow depths. The simple structure of exposed ice matches interpretations of radar passes that indicate regional sheets of ice hundreds of meters thick in many places on Mars, covered in thin surface material under 20 meters in thickness. Additionally, comprehensive radar study of lobate debris aprons (LDA) in the Deuteronilus Mensae region found a composition of 80% ice. [Dundas, et. al. 2018, Petersen, et. al. 2018].

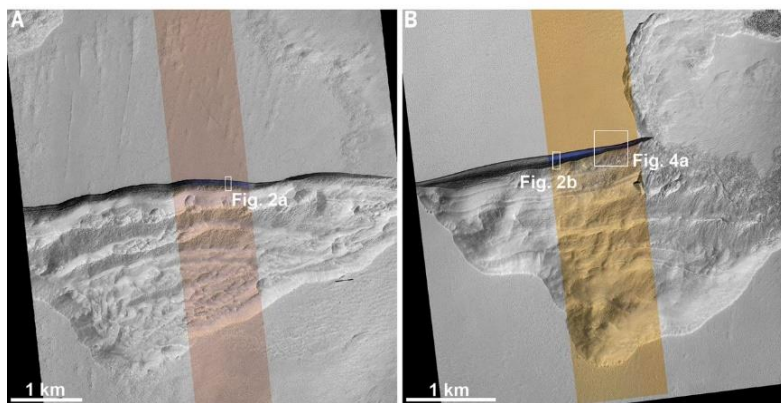


Figure 3.4. Mars, example of steep scarps with visible water ice. Credit: NASA/Dundas, C.M.

Mars is the closest planet to Earth at opposition, other than Venus which also doesn't have water ice. The planet also has a surface gravity of roughly 3.72 m/s^2 and a thin atmosphere to help EDL [Konopliv, et. al. 2011]. Water ice at poles and mid-latitude near-surface glacier sheets in very large volume and high

purity, combined with near term exploration plans before or shortly after a return to the Moon, makes Mars a priority for developing Thermal Mining.

Comet, 67P/Churyumov-Gerasimenko

A major portion of a cometary nuclei is composed of water, and water vapor is often abundant in a comet's coma. Despite this, for the many comets observed so far, it has been common to observe a lack of exposed water ice. Most comets appear coated in dark debris that is refractory, dehydrated, and organic. However, on one observed comet called 67P/Churyumov-Gerasimenko, exposed water ice was detected (Figure 3.5) on walls where recent debris falls had occurred and at their base [Filacchione, et. al. 2016]. The comet 67P is 18.7 cubic kilometers in size and composed of mostly hard ice covered in about 20 cm of debris, according to measurements made by the Philae lander [Patzold, et. al. 2016, Emily, et. al. 2014]. While it is unknown if all comets have a similar composition, the presence of water in other comet coma suggests similarity. There are numerous comets in our Solar System, many of which pass near Earth. The problem with comets, including 67P, is that despite their water ice content they require long and difficult maneuvers for spacecraft rendezvous due to their unique orbits. For 67P this meant a 10-year journey with four gravity assists, since no launcher was capable of the large ΔV needed for a direct injection [ESA Rosetta FAQ 2020]. Because of difficult rendezvous, Thermal Mining of comets is not the best near-term choice since other objects containing water ice are far quicker and less expensive to reach. However, as future needs and technologies come to be, the significant quantities of water ice on comets such as 67P may become worth the effort.

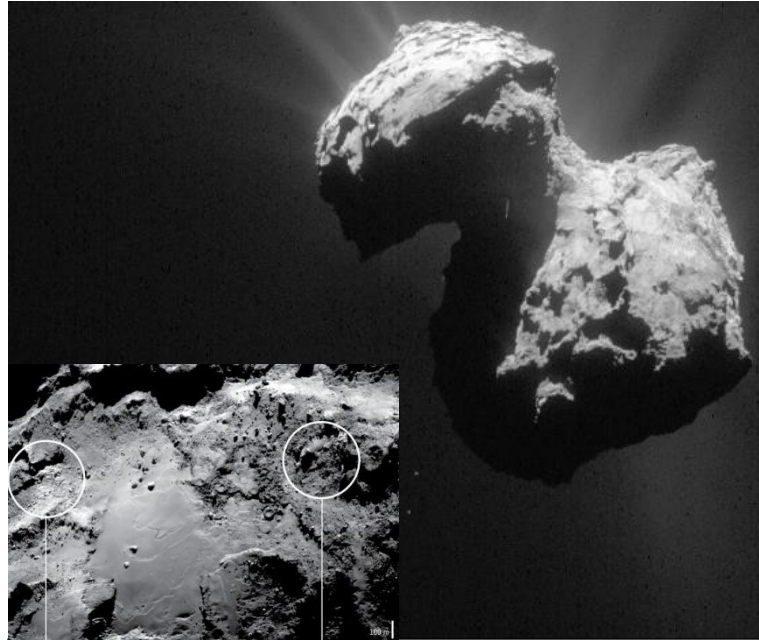


Figure 3.5. Comet 67P (top right), close-up of two areas of exposed water ice (bottom left). Credit: ESA/Rosetta.

Main Asteroid Belt

While objects in the main asteroid belt are significantly further from Earth than Mars, often nearly half-way to Jupiter, they present a great destination for Thermal Mining. Despite the distance involved to reach these objects, they are reachable in a few years with current ion propulsion technology [NASA Dawn 2019]. The benefit of these asteroids is that, other than planetary destinations like the Moon, Mars and Mercury, they are the nearest objects to Earth that contain water ice. Unlike planets, these asteroids don't have huge gravity wells that require heavy equipment for EDL, which means they can be reached using low mass electric propulsion. Thermal

Mining systems adapted to exploit these asteroids could supply water and propellant to a wide area of the Solar System using efficient propulsion, without ever expending propellant to leave a large gravity well.

Main Asteroid Belt, 24 Themis

24 Themis is located near the outer portion of the main asteroid belt and is a D type asteroid (Figure 3.6). It was discovered in 2009 that the roughly 198 km in diameter asteroid has a surface completely covered in water ice. Because of the Sun’s proximity to 24 Themis exposed ice will be warmed such that the ice sublimates away. The presence of surface ice suggests that water ice is abundant in the interior of 24 Themis in order to allow replenishment of exposed surface ice [Cowen, et. al. 2009]. Possible mechanisms for replenishment of surface ice from a subsurface reservoir include gradual outgassing or sudden release from impacts. Observations of the water ice on 24 Themis has led some to conclude that ice is more common on asteroids, and in their interiors, much closer to the sun than previously thought [Rivkin, et. al. 2010].

Main Asteroid Belt, Ceres

Ceres is located near the outer portion of the main asteroid belt and is a D type asteroid (Figure 3.7). In 2014 water vapor was detected around Ceres. It was discovered that 6kg per second of water vapor is released, originating from mid-latitude surface sources [Küppers, et. al. 2014]. The plumes were unexpected for an asteroid, especially from the largest object in the asteroid belt. These observed emissions gave unambiguous evidence for water ice at or near the surface, of a significant volume to support the large emission of water vapor seen. Ceres is the largest asteroid, and also the only asteroid which is also considered a dwarf planet instead of a small Solar System body (SSSB), due to its huge 939km diameter size and fully ellipsoidal shape [Lang, et. al. 2011]. Because of its huge size, Ceres is differentiated so compressed liquid near its core may occasionally force liquid water to its surface producing cryovolcanism [Sori, et. al. 2018]. These various observations of and sources for water ice on the surface of Ceres pose a great environment for Thermal Mining, and the scale of Ceres makes for a unique destination between average sized asteroids and moons.

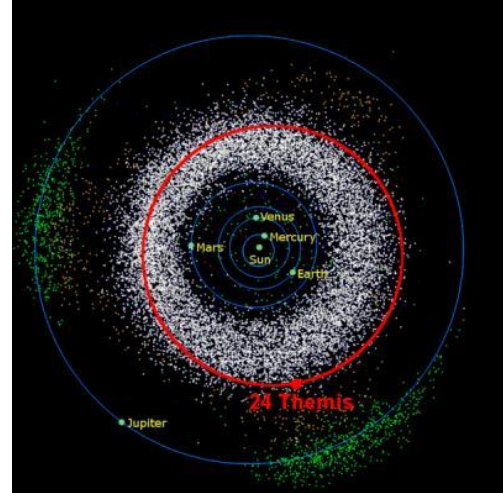


Figure 3.6. 24 Themis, approx. orbit of asteroid (red). Credit: Josh Emery/University of Tennessee, Knoxville.



Figure 3.7. Ceres, approx. true-color image. Credit: NASA/Dawn.

Main Asteroid Belt, 65 Cybele

65 Cybele is located near the outer portion of the main asteroid belt and is a D type asteroid (Figure 3.8). In 2011 water ice in the form of frost was spectroscopically observed [Licandro, et. al. 2011]. This band is the same used to identify water ice on 24 Themis and which was subsequently detected at Ceres. At roughly 250km in diameter, 65 Cybele is somewhat larger than 24 Themis and less than a third the diameter of Ceres. Like 24 Themis, due to the location in the asteroid belt, sunlight should vaporize exposed ice, so mechanisms for replenishment of surface ice must exist to bring ice from the subsurface [Jewitt, et. al. 2011]. Based on this 65, Cybele is expected to have significant subsurface water ice exploitable via Thermal Mining.

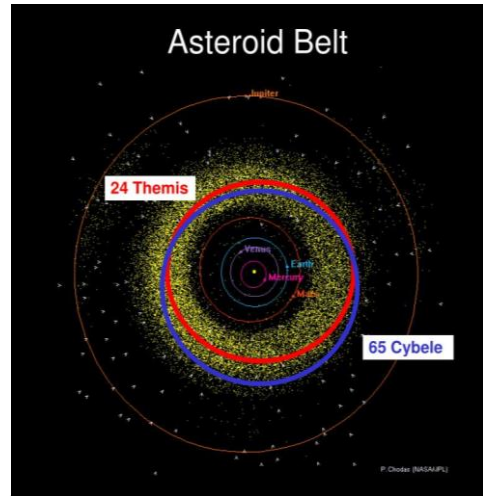


Figure 3.8. 65 Cybele, approx. orbit of asteroid (blue). Credit: P. Chodas/NASA/JPL

Jupiter’s moon, Ganymede

Ganymede has an icy crust up to 100 km thick with 30-50wt % water ice [McCord, et. al. 1998]. Its surface is varied with both older heavily cratered areas and newer more smooth plains [Collins, et. al. 2014]. Beneath the ice shell lies a salty subsurface ocean containing more water than all of Earth's oceans [Tobie, et. al. 2018] (Figure 3.9). With a huge quantity of ice on the surface, of varying composition, the potential for Thermal Mining on Ganymede is huge.

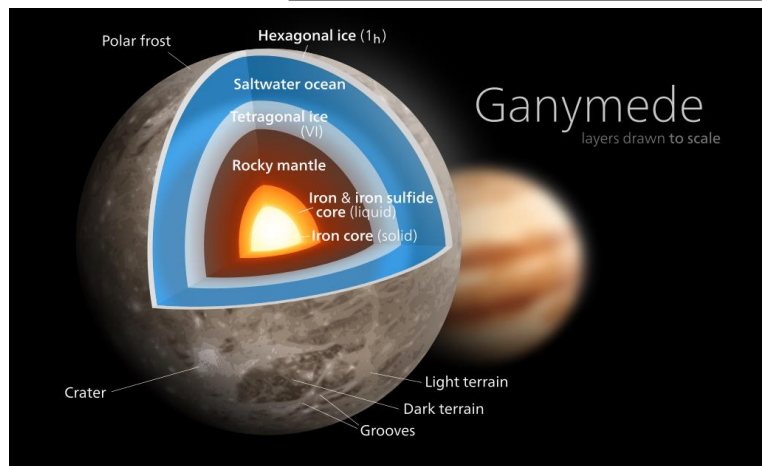


Figure 3.9. Ganymede, surface and subsurface layers, visualized. Credit: NASA

Jupiter’s moon, Callisto

Callisto is comparable in size to the planet Mercury (Figure 3.10), but just a third of the mass [Collins, et. al. 2014]. This mass difference can be attributed to the icy composition of the moon. This moon has a heavily cratered surface and a significant quantity of accessible water ice

and other ices [McCord, et. al. 1998]. Beneath the moon’s ice is a large subsurface ocean, smaller than Ganymede’s but larger than Europa’s. Thermal Mining would be ideal to exploit the large quantity of ice on Callisto.

Jupiter’s moon, Europa

Europa is covered in surface ice that is between 10 to 40 km thick (Figure 3.11). Beneath that ice is a large subsurface ocean which is smaller in volume than those of Ganymede or Callisto [Tobie, et. al. 2018]. Like both Ganymede and Callisto, the potential for Thermal Mining on Europa is huge due to the large quantity of available water ice.

Jupiter’s other moons

Jupiter has a total of 79 known moons and a large percentage of these are thought to contain water ice that would be compatible with Thermal Mining [Sheppard, et. al. 2018]. They range widely in size from quite large to tiny. Since the Galileo mission we have known that all of Jupiter’s moons observed then, except for Io, contain significant water ice [McCord, et. al. 1998]. These various moons have a wide variety of shapes and sizes. Many should be amenable to Thermal Mining, giving us a large set of bodies to choose from.

Jupiter Trojans

In Jupiter’s two trojan points at L4 and L5 there are thought to exist more than one million objects larger than 1km in diameter (Figure 3.12) [Yoshida, et. al. 2005]. Of these, observations have confirmed 7673 to exist [IAU 2020]. While remote measurements have only detected dark

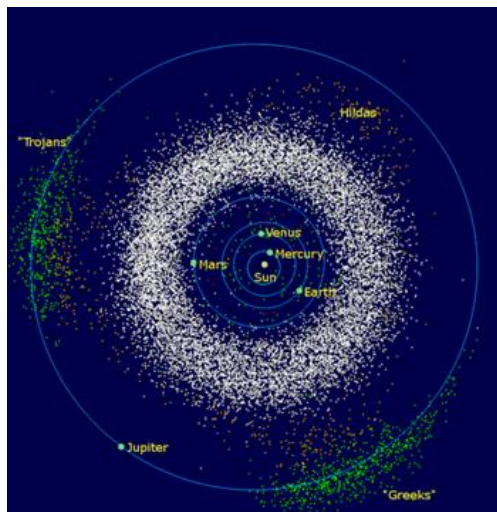


Figure 3.12. Jupiter Trojans, two groups of Trojan objects (green).
Credit: Wikipedia.



Figure 3.10. Callisto, approx. true-color image.
Credit: NASA/Dawn.

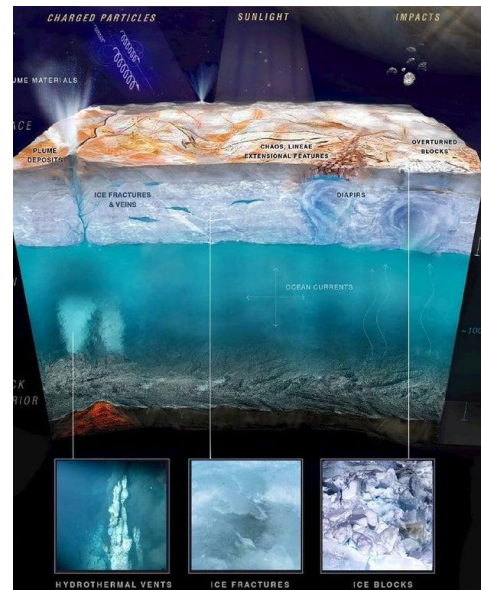


Figure 3.11. Europa, side view of ice and hydrothermal vents.
Credit: NASA.

surface features, the Jupiter Trojans could hold ice rich interiors under a covering of refractory matter, similar to that seen on some main belt asteroids and to the buried ices of comets that sublimate and release the coma. One observation of a Trojan named Ennomos did hint at surface ice. If this surface ice can be explained by a recent

impact revealing icy subsurface ejecta, that would confirm the existence of subsurface water ice on Trojans [Jewitt, et al. 2004].

Saturn’s moon, Titan

The surface of Titan has open lakes and rivers of liquid methane and ethane. Water ice is the moon’s crust which includes exposed water ice that form mountains [Griffith, et. al. 2003]. Titan also has an area of exposed water ice on its surface that is thousands of kilometers long (Figure 3.13). Due to the presence of water ice, methane and favorable atmosphere for EDL, Titan is a great location for resource development in general and Thermal Mining in particular.

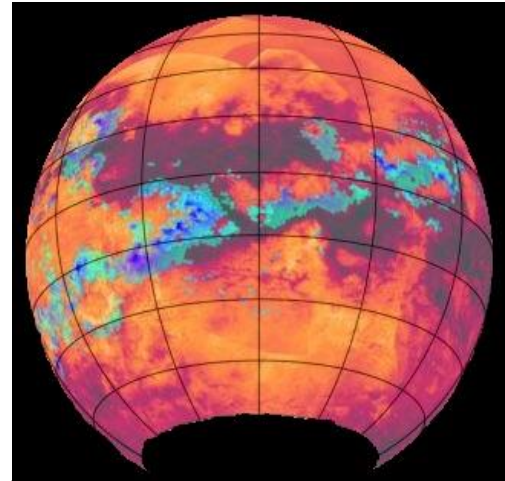


Figure 3.13. Titan, exposed water ice on the surface (blue). Credit: NASA/Cassini.

Saturn’s moon, Rhea

About 60% of Rhea’s mass is likely water ice that behaves like rock due to cold temperatures. It has a heavily cratered surface, with more craters than Dione, hinting at less internal activity. It orbits within the E ring, formed by ice particles from Enceladus. These ice particles become deposited on the surface of Rhea [Dougherty, et. al. 2018]. It possesses a very tenuous atmosphere (exosphere) of oxygen and carbon dioxide due to Saturn irradiating its surface [Teolis, et. al. 2010]. Without the benefit of Titan’s thicker atmosphere, Rhea still is a plentiful source of water ice for Thermal Mining.

Saturn’s moon, Iapetus

Iapetus has a density 1.2 times that of liquid water, and is thought to be 75% ice and 25% rock. It may have methane or ammonia ice in the interior. It has the highest surface brightness of all large objects in the Saturn system. Its leading hemisphere is 25 times darker than the trailing hemisphere and is similar in darkness to cometary nuclei. The dark material is reddish in color with a thin organics-bearing ice layer (Figure 3.14). The dark material exhibits nearly perfect longitudinal symmetry with respect to the direction of orbital motion. The dark dust is an erosion product originating from Phoebe. The dark hemisphere is warmer due to color and the brighter hemisphere is colder. The warm temperature of the dark material allows volatiles to sublime out

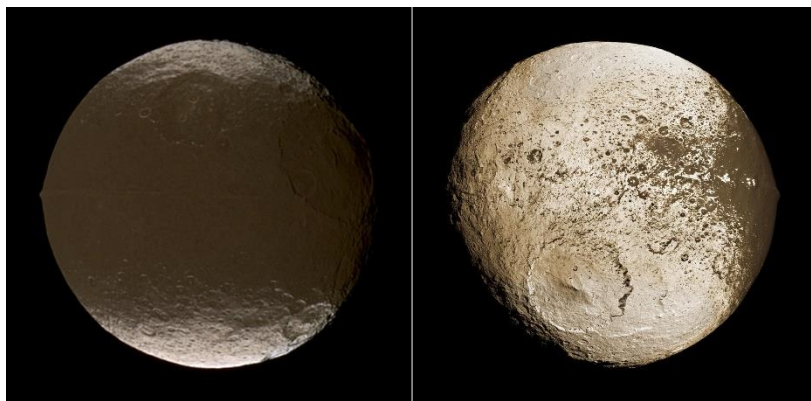


Figure 3.14. Iapetus, leading hemisphere (left), trailing hemisphere (right). Credit: NASA/JPL-Caltech/SSI.

and migrate to the colder hemisphere [Dougherty, et. al. 2018]. Aside from the lack of atmosphere, this moon is primarily made up of water ice and would be a good target for Thermal Mining.

Saturn’s moon, Dione

Two thirds of Dione’s mass is water ice, with a dense core and other ices making up the rest. The moon’s two hemispheres have the highest brightness contrasts of any of Saturn’s moons, besides Iapetus. Dione shows considerable evidence of internal activity and has lower crater population than Rhea, including resurfaced plains and troughs or valleys hundreds of kilometers in length. It orbits within E ring which is formed by ice particles from Enceladus. Some of these ice particles become deposited on the orbital leading hemisphere of Dione (Figure 3.15). Dione also has a very tenuous atmosphere, or exosphere, observed to contain molecular oxygen [Dougherty, et. al. 2018]. With a significant portion of the moon being composed of water ice, and known areas having fewer craters due to resurfacing, this moon looks to be a good target for Thermal Mining despite lacking a significant atmosphere.

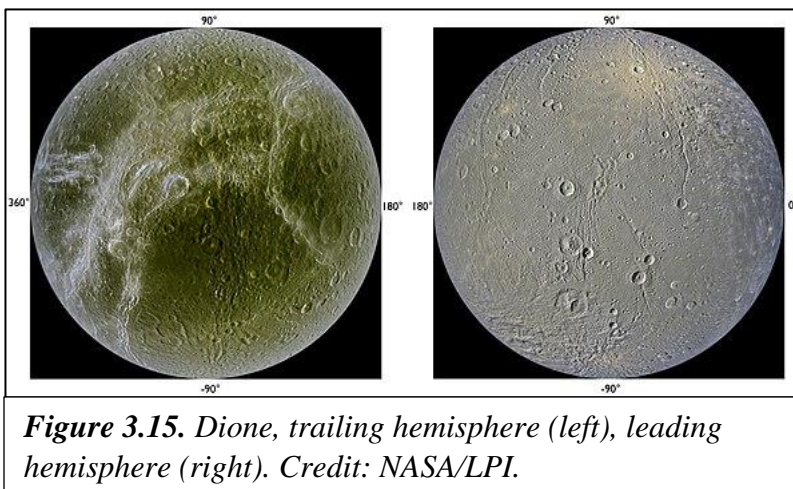


Figure 3.15. Dione, trailing hemisphere (left), leading hemisphere (right). Credit: NASA/LPI.

Saturn’s moon, Tethys

The low density of Tethys indicates that it consists almost entirely of water ice. The moon orbits within Saturn’s E ring which is formed by ice particles from Enceladus which also deposit on the orbital leading side surface of Tethys. Charged particles from Saturn bombard the trailing side which causes chemical alteration and color changes in the surface ice (Figure 3.16) [Dougherty, et. al. 2018]. Like most other Saturn moons, Tethys is largely composed of water ice and would make a good target for Thermal Mining.

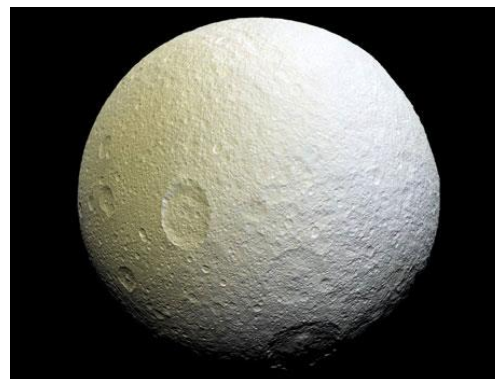


Figure 3.16. Tethys, trailing hemisphere (left), leading hemisphere (right). Credit: NASA/JPL/SSI.

Saturn's moon, Enceladus

Enceladus is the brightest moon in the Solar System and reflects almost 90% of received light. Its low density indicates it is almost entirely ice, with observed extensive water vapor and ice particle plumes. The surface has vast crater-free equatorial smooth plains. The subsurface has a global ocean of liquid water with potential hydrothermal vents on the seafloor evidenced by material in ice plume hard to explain by other means. A heat source from moon interior, focused on south polar tiger stripe region, has continuous release of over 16 gigawatts of energy. Water vapor gas and ice plumes including at least 100 individual jets shoot from the south polar tiger stripe region, composed of 90% water vapor, travelling thousands of kilometers into space, impacting Enceladus and forming Saturn's E ring. Based on wobble as Enceladus orbits Saturn, a liquid ocean is thought to be 10km deep under south polar region with a 26–31km thick ice shell (Figure 3.17) [Dougherty, et. al. 2018]. There is a huge resource of water ice and other liquid and icy materials on Enceladus. The water ice is very appropriate for Thermal Mining technology, which may even be useful for exploring this moon's ocean for potential life.

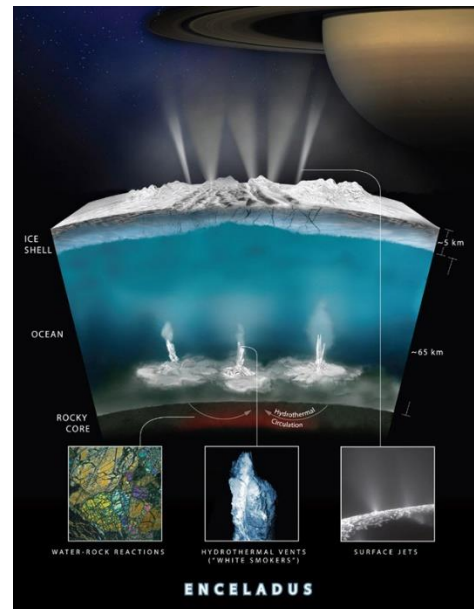


Figure 3.17. *Enceladus, side view of ice and hydrothermal vents. Credit: NASA/JPL/Cassini.*

Saturn's moon, Mimas

The low density of Mimas indicates it is almost entirely ice. Observations confirm the surface is dominated by water ice, with a fairly uniform albedo. It is extremely heavily cratered. Mimas orbits within the E ring whose particles are deposited on the orbital trailing side surface of Mimas. The moon has strange daytime temperatures (Figure 3.18) and a non-uniform interior which leads to greater libration in one part of the moon. This and the older cratered surface suggest that Mimas may lack a subsurface ocean [Tajeddine, et. al. 2014]. This possible lack of ocean despite Mimas being almost entirely water ice means that it is uniquely excellent for intensive Thermal Mining.

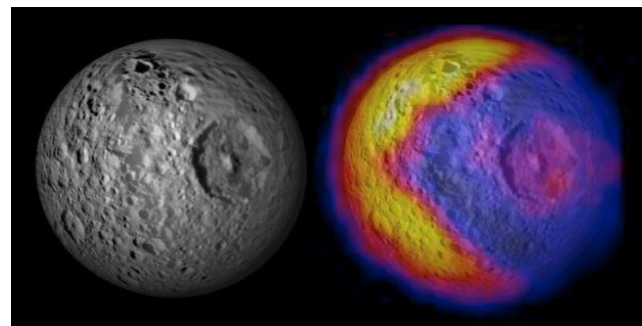


Figure 3.18. *Mimas, image of moon (left), heat map of daytime temperatures (right). Credit: NASA/JPL/Cassini.*

Saturn's moon, Phoebe

Phoebe has a darker surface with lower albedo than Saturn's other moons. The moon only reflects about 4% of the light it receives. It is nearly as dark as Iapetus. Material has been confirmed to erode from Phoebe and transfer to Iapetus as it crosses its orbital path accreting on the leading face of the moon. Phoebe is thought to be a trapped Kuiper belt object, partially due to its unusual shape and the fact that it is the only moon in Saturn's system that orbits in retrograde (Figure 3.19). Water ice was detected on the moon through the near-infrared reflectance spectrum [Owen, et. al. 1999].



Figure 3.19.
Phoebe, the irregular moon.
Credit:
NASA/JPL/Cassini.

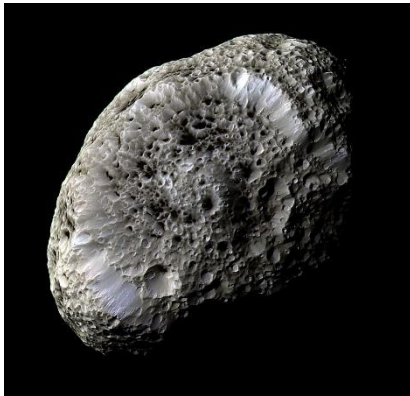


Figure 3.20. *Hyperion, seen here with its porous and sponge-like exterior.* Credit:
NASA/JPL/SSI.

Saturn's moon, Hyperion

Similar to Phoebe, this moon is darker and has lower albedo than most other moons. It has a density of just over half that of water, possibly due to being composed of mostly water ice with porous gaps making up more than 40 percent of its volume. It may also contain lighter frozen materials such as methane or carbon dioxide [Thomas, et. al. 2007]. It has also been observed to contain complex compounds and have an unusual sponge-like appearance, which gives further evidence of high porosity (Figure 3.20). Hyperion is the only moon known to not be synchronously locked with Saturn, meaning one side does not always face Saturn.

Saturn's other moons and Trojans

There are 73 additional currently known moons of Saturn [NASA, 2019]. Many of these are also icy and likely compatible with Thermal Mining, but for brevity these will not be covered in this report. Saturn has no known Trojan asteroids.

Centaur

These objects have characteristics of both asteroids and comets. Water ice has been detected on or in the ring system of many, such as 1997 CU26, 1999 UG5, and Chariklo [Brown, et. al. 1998, Bauer, et. al. 2002]. Of the many found to have water ice, Chariklo (Figure 3.21) is also the largest Centaur known to exist [Braga-Ribas, et. al. 2014]. Centaurs orbit primarily between Jupiter and Neptune. All these targets are compatible with Thermal Mining if an alternative source of energy is used due to distance from the Sun. The unique orbits

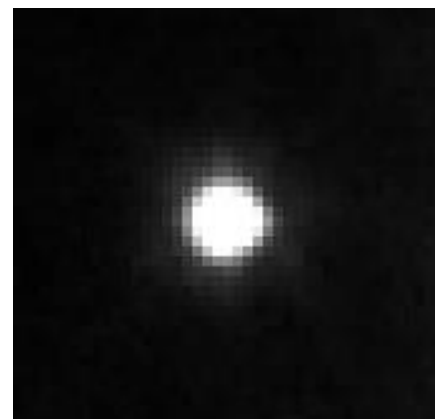


Figure 3.21. *Chariklo, Hubble Space Telescope image of the largest centaur.*
Credit: NASA/Hubble.

of these objects also provide a unique area to produce water and propellant that may become beneficial as activities grow throughout the Solar System.

Uranus's moons

Uranus has 27 known moons. The largest moon of Uranus, in both mass and diameter, is Titania (Figure 3.22). Titania is a bit less than half the diameter of Earth's moon, while having slightly more than half its density. It is thought to be equal parts silica rock and water ice, with a surface covered in water and carbon dioxide ices.

Of the moons of Uranus, water ice is observed to be more prevalent on the leading hemispheres of Ariel through Titania, but more prevalent on the trailing hemisphere of Oberon [Grundy, et. al. 2006]. The moons of Uranus are all great prospects for Thermal Mining once fuel and resources are needed in this region. Energy sources besides the Sun would be optimal due to solar distance.

Uranus Trojan

There is one Trojan of Uranus known to exist, known as 2011 QF99. This object is made of rock and ice, with a diameter of 60 km, and orbits near Uranus's L4 point [UBC 2013]. Thermal Mining of this object's ice would be possible, though further confirmation of surface ice is needed. Existing in a very remote area, this object could provide utility as a refueling location for water and propellant when a future need arises.

Neptune's Moons

Neptune has 14 known moons. The largest moon of Neptune, comprising 99.5% of the entire Neptunian moon system's mass, is Triton (Figure 3.23) [Jacobson 2009]. Triton's surface crust is a primarily frozen nitrogen, with 15–35% water ice, and 10–20% frozen CO₂. Neptune's second largest moon, Proteus, is also thought to have significant water ice, but none has been detected on the surface [Dumas 2003]. Neptune's third largest moon, Nereid, and many others, have had water ice detected on their surfaces [Brown, et. al. 1998]. Due to the prevalence of water ice on the surface of these moons, they would be good candidates for Thermal Mining using non-solar energy sources.

When activities in space reach the Neptune system, Thermal Mining will enable plentiful water and propellant to be made available.

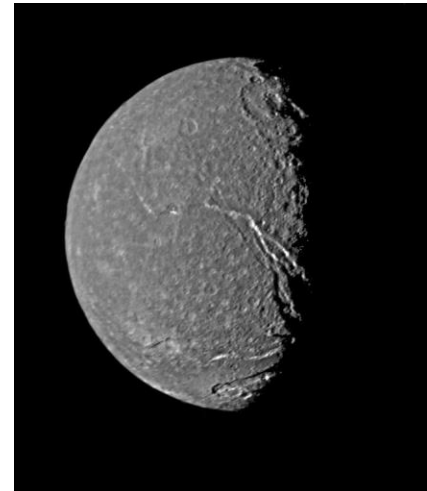


Figure 3.22. *Titania, Voyager 2 image of the largest moon of Uranus. Credit: NASA/Voyager 2.*

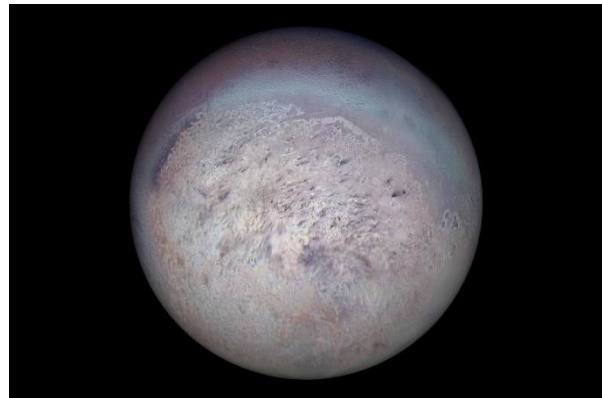


Figure 3.23. *Triton, Voyager 2 image of the largest moon of Neptune. Credit: NASA/Voyager 2.*

Neptune Trojans

Twenty-four Trojans of Neptune have been confirmed to exist [IAU 2020]. Spotting these objects is highly difficult because they are faint, and the observation direction is currently the same as the bright Milky Way. These objects have been observed to look like Jupiter Trojans or comets, meaning surface level water ice is likely to exist. Beyond these 24, Neptune's Trojan asteroids may outnumber Jupiter's Trojans by 5 to 20 times and outnumber even the objects in the Main Asteroid Belt [Sheppard, et. al. 2006]. This vast number of objects (Figure 3.24), potentially in the orbit of Neptune in the Neptune L4 and L5 regions, including the 24 objects currently known, show great promise as targets for Thermal Mining due to the high prevalence of water ice expected to make up objects in the region. As activities in the Neptune system start to occur, targeting these objects and the moons of Neptune for Thermal Mining will be highly useful for developing local sources of water.

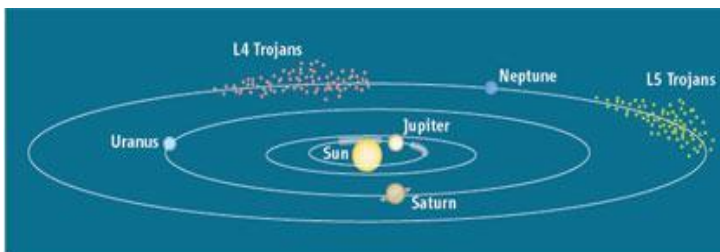


Figure 3.24. Relative locations of Neptune's L4 and L5 Trojans. Credit: Science.

Beyond these 24, Neptune's Trojan asteroids may outnumber Jupiter's Trojans by 5 to 20 times and outnumber even the objects in the Main Asteroid Belt [Sheppard, et. al. 2006]. This vast number of objects (Figure 3.24), potentially in the orbit of Neptune in the Neptune L4 and L5 regions, including the 24 objects currently known, show great promise as targets for Thermal Mining due to the high prevalence of water ice expected to make up objects in the region. As activities in the Neptune system start to occur, targeting these objects and the moons of Neptune for Thermal Mining will be highly useful for developing local sources of water.

Trans-Neptunian Objects

There are 2498 currently known Trans-Neptunian Objects (TNOs), most of which are thought to be icy minor planets (Figure 3.25) [IAU 2020]. The TNOs all orbit the Sun at a greater distance on average than Neptune, with some objects called sednoids whose semi-major axis must be at least 150 AU. This huge group of objects includes other subgroups such as the Kuiper belt objects. The first TNO discovered was Pluto in 1930. These distant objects all are thought to be icy which means there is great potential for Thermal Mining. While such distant objects are not a near term priority, the availability of water and other volatiles from such distant bodies could provide those in the future with a great resource.

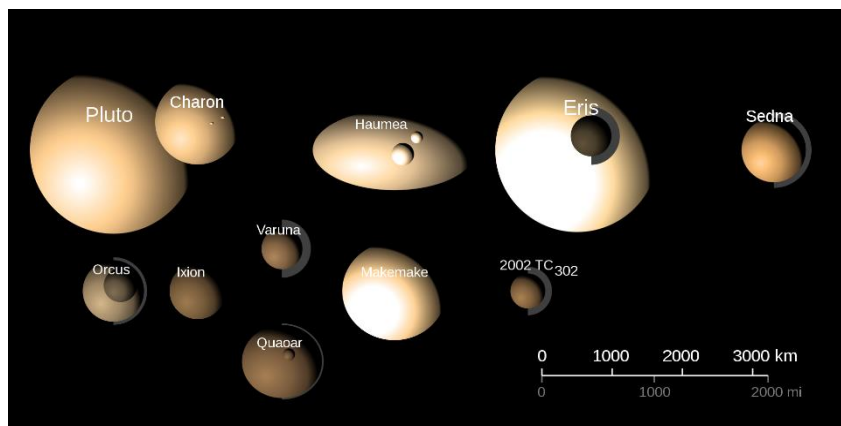


Figure 3.25. Relative sizes, colors, and albedos for some of the large Trans-Neptunian objects. Credit: Eurocommuter~commonswiki.

discovered was Pluto in 1930. These distant objects all are thought to be icy which means there is great potential for Thermal Mining. While such distant objects are not a near term priority, the availability of water and other volatiles from such distant bodies could provide those in the future with a great resource.

Trans-Neptunian Objects, 90482 Orcus & Moon Vanth

Discovered in 2004, this TNO is an icy minor planet whose orbit is very much like Pluto except with an opposite phase and aphelion [IAU 2004 DW]. Orcus is roughly 910 km in diameter and its moon Vanth is quite comparably large at 442 km (Figure 3.26). Orcus has good potential

for Thermal Mining due to a surface rich in crystalline water ice and potentially methane or ammonia [Brown, et. al. 2018].

Trans-Neptunian Objects, Pluto & Moon Charon

Pluto was discovered in 1930 and considered the Solar System’s ninth planet until 2006 (Figure 3.27). The surface is covered in ice that is more than 98% nitrogen. Just below the surface is water ice making up the crust. At a depth of at least 100km a liquid water ocean begins, and at the core is silicate rock [Hussmann, et. al. 2006]. At roughly 2300km in diameter, its size is smaller than Earth’s Moon, but it is hugely rich in ices that make it very compatible with Thermal Mining [Stern, et. al. 2017]. Pluto’s large moon Charon is also covered in water ice, making it a good target for Thermal Mining as well (Figure 3.27).

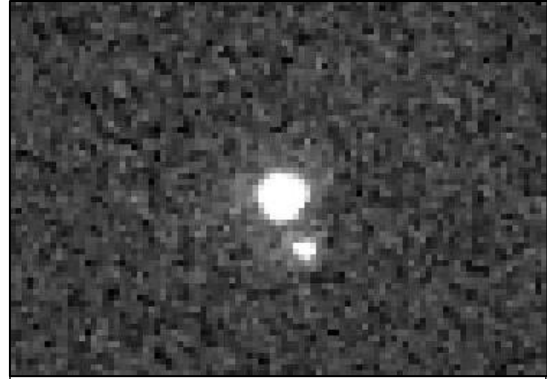


Figure 3.26. Orcus & moon Vanth, Hubble Space Telescope image of the dwarf planet Orcus (center) and its moon (center-bottom). Credit: NASA/Hubble.

Trans-Neptunian Objects, Eris & Moon Dysnomia

Discovered in 2018, Eris is more massive than Pluto and slightly smaller in diameter, making it the most massive known dwarf planet in the Solar System. Its moon, Dysnomia, is also smaller than Pluto’s moon Charon (Figure 3.28). Eris and its moon orbit the Sun such that they can be up to three times further away from the Sun in their orbit than

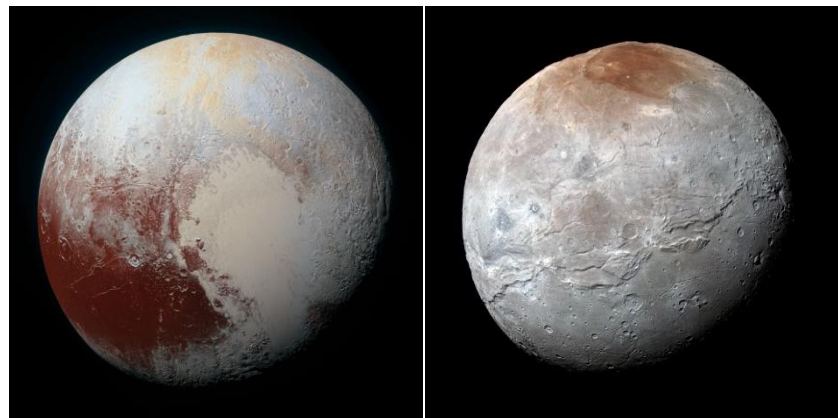


Figure 3.27. Pluto & moon Charon. Image of Pluto (left), enlarged image of Pluto’s moon Charon (right). Credit: NASA/New Horizons.

Pluto. At the time of discovery, it was briefly considered a tenth planet with Pluto being the ninth, before both were designated as dwarf planets along with many other discovered objects [IAU 2016]. Methane ice has been detected on its surface, which hints that the surface may be similar to Pluto [Gemini Observatory 2005]. Due to its density, Eris is thought to be composed largely of rocky materials, so there may be proportionately less water ice in Eris than is found in Pluto [Sicardy, et. al. 2011].

3.2 Thermal Mining Beyond the Moon

Based on information currently available, numerous objects have been identified as having water ice that would be exploitable with Thermal Mining. Since these objects have broadly different locations and traits, it is useful to prioritize which objects to focus on first.

First, objects are ordered based on proximity to Earth, with those closest to Earth given first consideration. This is because Thermal Mining will generate a supply of water and propellant to maintain space operations in a region. Because human activity is expected to expand to other relatively nearby objects after the Moon and cislunar space, initial focus is given to objects within the distance of the main asteroid belt.

Looking at those objects within this inner region, the nearest identified with water ice is the planet Mercury. With no atmosphere and nearly the gravity of Mars (3.7 vs 3.72), the cost of landing surface systems for Thermal Mining using fully propulsive entry-descent and landing (EDL) would be large. Based on this, high ΔV requirements for reaching Mercury, and lack of plans to prioritize significant operations near Mercury, the planet is a low priority until future operations justify it.

Although farther away than Mercury, Mars contains significant water ice and lies next in proximity. While landing has proven historically challenging, it has been accomplished many times, and landing surface systems for Thermal Mining is feasible. Mars is also a significant priority for future study, human exploration, and habitation at increased scale. Due to the quantity of operations foreseen on Mars in the future, it is a priority target.

In a survey of other proximate non-planetary objects, water ice is thought to be absent from the surface of most. There are a few exceptions which should be the next priority for Thermal Mining investigation. The benefit of smaller objects is lack of a significant gravity well which simplifies operations from a ΔV perspective and thus provides a reduced cost of operations. The main objects that fit the near proximity criteria with water ice are comets and objects in the main asteroid belt. Cometary objects are excluded from initial consideration due to the high ΔV required for access. From the second category, greater ice content is known to exist in outer portions of the main asteroid belt. Focus was given to larger objects in the main asteroid belt, not including the furthest portion of the outer belt due to greater distances. Multiple larger objects have confirmed surface water ice, with thousands more theorized.

Of objects in the main asteroid belt identified to contain surface water ice amenable to Thermal Mining, all were identified as type D objects. These include Ceres, 24 Themis, and 65 Cybele. These objects have an approximate range in diameter of 91km to 939km. They are the next priority for Thermal Mining (beyond the Moon and Mars) because they have the benefit of low gravity and require little ΔV to access. Of the asteroids identified, priority was given to objects with the highest degree of certainty around ice content and for which a dedicated conceptual study would bring the most value. With that set of priorities in mind, Ceres is differentiated, and the largest main belt object confirmed with unambiguous evidence of water ice at its surface. It also contains the unique feature of significant release of water vapor (6kg per second). Beyond Ceres,

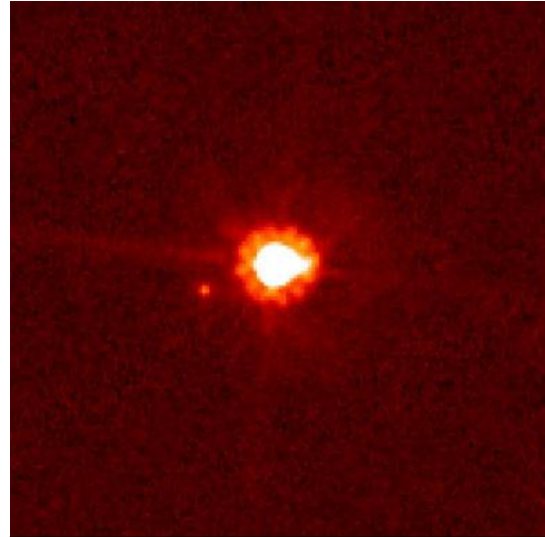


Figure 3.28. *Eris & moon Dysnomia, Hubble Space Telescope image of the most massive dwarf planet (center) and its moon (center-left). Credit: NASA/Hubble.*

the smaller 24 Themis is an ideal target due to a surface that completely covered in ice and a smaller size, roughly one fifth the diameter of Ceres. For the purpose of supporting space activities outside planetary gravity wells, these sources of water ice are the most accessible for Thermal Mining.

While Mars, Ceres, and 24 Themis are identified to be the next priority targets to study for Thermal Mining of water ice, a great number of additional opportunities exist. As more data is obtained on objects in space, additional ice will be found in new locations both near and far. Once initial operations on Mars and in the main asteroid belt have begun, that new proximity and focus will lead to accelerated discoveries of available resources. As more advanced space operations commence, other resources will also become important to extract, and in the realm of those accessible through Thermal Mining there are many volatiles found in ice form other than water. These are present in great quantity on objects near Jupiter and beyond. Based on future need and discovery, these more exotic ices will be a great additional product capable of collection using Thermal Mining technology.

Operations in space will grow over time, driving an ever-increasing demand for resources. But resources contained in objects no further than the asteroid belt are vast. Some of the most valuable resources are volatiles frozen in the form of ices. These volatile commodities can be extracted very efficiently using the techniques of Thermal Mining. Our survey has identified a number of Thermal Mining targets that are well aligned with the expected trajectory of human expansion into the solar system: the Moon and cislunar space → Mars → the main asteroid belt → the moons of Jupiter and Saturn → the outer solar system. Thermal Mining will be critical to unlocking the resources that will underpin this expansion.

4.0 Thermal Mining Mission Context: Lunar Polar Ice Mining

One of the great discoveries in planetary science of the past several decades is that water is ubiquitous in the inner solar system. Water is critical for sustainable space exploration. It is essential for life; one of its constituents is oxygen, a critical component of breathing air; it makes a superb radiation shielding material; and it can be split in hydrogen and oxygen, then liquified into LH₂/LO₂ rocket propellants. In particular, there is mounting evidence that water exists near the poles of the Moon, trapped in permanently shadowed regions (PSRs). Most of this evidence comes from remote sensing observations [Feldman et al., 1998; Nozette et al., 2001; Spudis et al., 2013; Hayne et al., 2015; Fisher et al., 2017; Sanin et al., 2017; Li et al., 2018], although ejecta from the impact of a Centaur upper stage was observed by the LCROSS spacecraft [Colaprete, et al., 2010] indicating $5.6 \pm 1.9 \text{ wt\%}$ water ice. As shown in Table 1, the LCROSS impact plume contained at least a dozen other chemical species, most at much lower concentrations than water.

Table 4.0.1. Volatiles in LCROSS Ejecta. Modified from Colaprete, et al., 2010 and Gladstone, et al., 2010.

Compound	Symbol	Concentration (wt%)
water	H ₂ O	5.5
hydrogen sulfide	H ₂ S	0.92
hydrogen gas	H ₂	0.69
carbon monoxide	CO	0.57
Calcium	Ca	0.4
Ammonia	NH ₃	0.33
Mercury	Hg	0.24
Magnesium	Mg	0.19
Sulfur dioxide	SO ₂	0.18
Ethylene	C ₂ H ₄	0.17
Carbon dioxide	CO ₂	0.12
Methanol	CH ₃ OH	0.09
Methane	CH ₄	0.04

Little is known about the origin of water ice and other volatiles on the Moon. One hypothesis is that much of the ice is ancient, a result of asteroid and comet impacts billions of years ago [Watson et al., 1961; Arnold et al., 1979; Ong et al., 2010; Prem et al., 2015]. Other mechanisms include solar wind implantation combined with cold trapping in the PSRs [Crider &

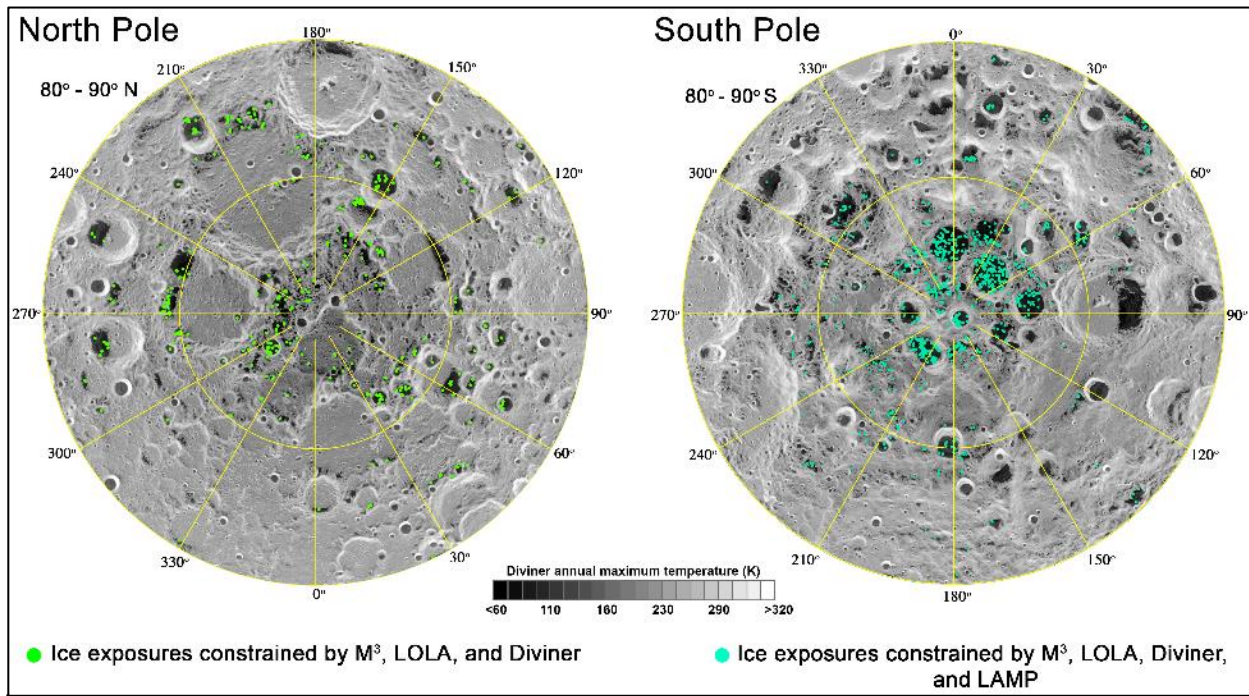


Figure 4.0.1. Ice exposures at the North Pole and South Pole of the Moon [Li et al. 2018].

Vondrak, 2000; Vondrak & Crider, 2003] and water released during volcanic episodes [Needham et al., 2019]. There may be a continuous source of water liberated from lunar regolith by impact gardening [Benna, et al. 2019; Zhu et al., 2019]. Asteroid impactors also contain water and other volatiles chemically bound that could be liberated on impact. It is likely that a combination of all or some of these mechanisms is involved.

Once deposited in the PSRs, the volatile-bearing material is subject to a continuing evolution via a number of space weathering processes. Impact gardening is likely most significant: continuous bombardment of impactors of all sizes vaporizes ice in the crater region and covers ice with the ejecta blanket [Hurley et al., 2012]. In the hard-vacuum conditions of the lunar surface, exposed ice can sublime or desorb if chemically bound to regolith. Both these processes are greatly dependent on temperature. Surface ice can also erode due to sputtering and micro-meteoroid impact [Farrell et al., 2019]. In addition, volatiles may migrate within the subsurface due to thermal or electro-chemical processes [Schorghofer & Taylor, 2007; Schorghofer & Aharonson, 2014].

The first viable application of Thermal Mining will likely be mining water ice at the lunar poles. The effectiveness of Thermal Mining in the lunar PSRs will depend on the nature of the icy regolith as well as the distribution of ice with depth. There is a wide range of possibilities for the nature of the icy regolith. Most believe the bulk of the ice is located on or within the first few meters of the surface. Some believe it is like dirty snow. Others believe it is like frozen concrete. Thermal Mining using reflected sunlight will work best when the ice is at the surface or within the near subsurface. Lunar regolith is a very good insulator and heat penetration through dry regolith to reach buried ice would not be feasible with just surface heating. If the ice concentration is too low, most of the heat is expended warming the regolith and very little goes to sublimate ice. Our analysis indicates that 4wt% is a lower limit of ice concentration for effective Thermal Mining of lunar ice [Sowers & Dreyer, 2019]. However, as shown in Figure 4.0.1, there are indications of surface ice in concentrations of up to 30wt% [Li et al., 2018].

As promising as these data are, they are insufficient for characterizing lunar polar ice as a proven reserve for development into an economic asset (Figure 2.1). What is needed is a resource exploration (prospecting) campaign to identify economically viable locations for extraction and characterize the nature of the ice-bearing lunar material. To address this need, in June 2018, a workshop was held



Figure 4.0.2. Resource exploration (prospecting) roadmap.

at CSM to develop a roadmap for a resource exploration campaign [Sowers & Morris, 2018]. This roadmap is shown in Figure 4.0.2. The information from this campaign should be gathered in parallel with the development of Thermal Mining technology. Fortunately, early missions like the ground truth lander(s) will provide scientifically valuable information and are compatible with NASA’s Commercial Lunar Services Program (CLPS). A recent survey of potential polar sites of interest is provided by Flahaut et al., 2019.

The mission context we examined during this study was the application of Thermal Mining to the extraction of ice from the PSRs near the lunar poles. In this section, we present the details of the results of our investigations. Section 4.1 describes a 3-dimensional discrete element analysis (DEM) formulation we developed to investigate the formation and evolution of ice at the lunar poles due to the physical mechanisms discussed above. The results of this analysis will inform the subsequent development of the Thermal Mining system as well as the much-needed resource exploration campaign. Section 4.2 describes the details of the propellant production system architecture. Section 4.3 shows some of the systems engineering work, in particular the functional analysis focused on the ice extraction system. Section 4.4 discusses the detailed concept design of the ice extraction system while Section 4.5 covers more detail on the power system. Section 4.6 describes our launch and landing concept and Section 4.7 covers the concept of operations for ice extraction. Section 4.8 provides the details of the mass and cost estimates that feed into the business case analysis. The business case is described in Section 4.9.

Our conclusion is that ice extraction from the lunar PSRs for propellant production is not only technically feasible, but can produce favorable business returns.

4.1 Lunar Polar Ice Distribution Analysis

The Moon has been uniquely shaped by its long history. From the early bombardment phase that left it scarred and pockmarked, to the episodes of volcanism that produced the distinct mares, to the constant exposure to the solar wind, space radiation and vacuum, these and more have shaped the Moon we see today. In particular, these events have shaped the nature of the Moon’s poles and the volatile rich regions within the PSR’s. For example, most PSRs exist in large craters formed during the early bombardment of the lunar surface. Elsewhere, large basins filled with mare basalt may have altered the spin axis of the Moon, changing the locations where volatiles can accumulate and persist. Understanding the effects of the various formational and evolutionary events and processes on the PSR’s will greatly enhance our understanding of the volatiles including their sources, abundance, distribution and characteristics and inform the development of the Thermal Mining system for the Moon.

To begin to gain an understanding of these issues, we developed a 3-dimensional discrete element model (DEM) [Dickson & Sowers, 2019]. A similar model has been developed at the University of Central Florida (UCF) by Kevin Cannon [Cannon & Britt, 2020]. At this stage, only very preliminary results are available for simple scenarios.

The mathematical formulation is straightforward. The top D meters of a volatile laden patch of a lunar PSR is represented by a 3-D square grid of elements. Each grid cell is designated by coordinates: i, j, k ; $i = 1, N$; $j = 1, M$; $k = 1, D$. D is the depth of the modeled layer. The volume of each cell is $a \times b \times d$. The top layer has a volume of $a \times b \times \varepsilon$, where ε is a small number. This top layer captures frost-like deposits on the surface and can be used to compare to

remote sensing data as shown in Figure 4.0.1. It is anticipated that $a = b$, for simplicity. Initial trial runs of the simulation model set $\varepsilon = d$, therefore not capturing dynamic surface frosts.

The state of the volume at time, t , is represented by a set of state variables indexed to each discrete element: $S(t) = [\rho(t), \delta(t)]$, where

- $\rho_{i,j,k}(t)$ is the mass density of cell $\{i, j, k\}$ at time t
- $\delta_{i,j,k}(t)$ is the mass fraction of ice in the cell $\{i, j, k\}$ at time t . $0 \leq \delta(t) \leq 1.0$.

In our initial analysis, the ice mass fraction represents a single component, water ice. Future enhancements will include other volatile species from Table 4.0.1 and the state variable $\delta(t)$ will become a vector. Other state variables, for example, temperature, T , will be added in later versions of the model.

The initial state is $S(t_0) = [\rho(t_0), \delta(t_0)]$. For example, at $t = 0$, the state could be initialized with a layer of ice in the top n cells of the vertical dimension, with no ice in the layers below. In other words, the initial state $S(0)$ in the top layer at $t = 0$ and $k = 1, n$ is $[938\text{kg/m}^3, 1.0]$ and the initial state $S(0)$ in layers below is $[1890\text{kg/m}^3, 0.0]$. These ice and regolith density values correspond to dense dry regolith and hard water ice. They will be revisited based on future experimental work and ground truth data from the lunar PSRs.

The transformation of the state at time t to time $t + \Delta t$ is governed by the operator $H(t)$: $S(t + \Delta t) = H(t)S(t)$. A number of external mechanisms or forcings (short for forcing functions) are embodied in the state transition operator H . These can include:

1. *Impact gardening*: Ice is rearranged based on meteor impacts that occur randomly with a distribution of frequency and mass/energy. Each impact vaporizes some ice, moves some ice deeper and moves some deep material to the surface. There are different cratering models in the literature (size, depth, distribution). The one we implemented is due to Arnold [Arnold, 1975].
2. *Solar wind implantation*: Protons, i.e. hydrogen nuclei, that make up the bulk of the solar wind, can collide with oxygen atoms in lunar materials to produce water. [Crider & Vondrak, 2000]. Different PSRs, based on their geography and topography, would likely have different rates of solar wind in-migration and the magnitude of the solar wind itself has varied over the life of the Sun, so this mechanism is implemented by a time dependent rate adding ice to the surface layer.
3. *Sublimation*: Depending on the average temperature, ice is constantly sublimating into space at a general average rate. Certain PSRs, e.g. Shackleton, have a higher average temperature. Others, e.g. Shoemaker, have a higher average variation in temperature [Hayne et al., 2015] We assume for the purpose of this model that

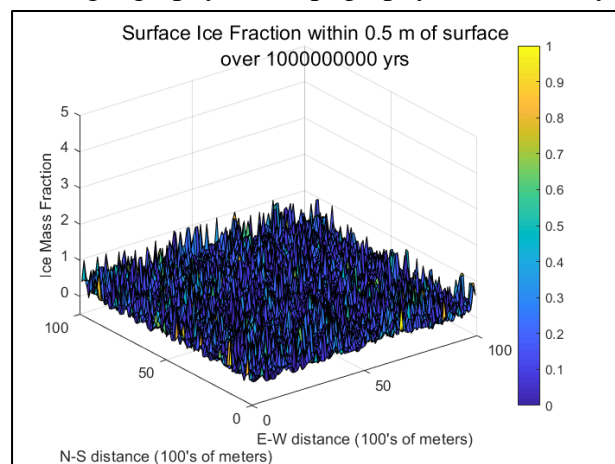


Figure 4.1.1. Initial results from the CSM model. Surface Ice Fraction 1m below the surface after 1B yrs.

the temperature is consistently low enough in the PSRs to render sublimation a negligible factor in the overall variation of ice sublimation [Feistal et al., 2007]. Further, we assume that the cold trap is “deep” enough such that vaporization of ice due to impact gardening ultimately results in re-deposition of some of the ice (mixed with regolith) through even distribution in the crater ejecta.

4. *Sputtering*. Continuous erosional mechanisms like sputtering act to counter solar wind implantation [Farrell et al. 2019]. For the initial analysis, we have neglected these mechanisms. Future iterations of the model will take them into account.
5. *Episodic deposition*. Some asteroid/comet impacts are of such significance as to create a temporary atmosphere on the Moon and deposit a substantial layer of ice in a PSR.
6. *Volcanism*. Volcanic episodes in the Moon’s past could have included the outgassing of water vapor. This water vapor can then migrate to the poles and be trapped in the PSRs. [Needham & Kring, 2017, Needham et al., 2019]

Other discrete events in the Moon’s history such as true polar wander will also be considered [Siegler et al., 2016].

In addition to external forcings, the state can change through the result of internal mechanisms. For example, a temperature gradient in the layer may cause migration of the volatiles or the action of gravity and periodic moonquakes can result in settling and compaction. Modeling this kind of evolution would require the addition of additional state variables like temperature. A set of initial conditions together with a history of external forcings as represented by the state transition matrix H is called a *scenario*.

Results to date have been for very simple scenarios. Figure 4.1.1 shows preliminary results for a scenario with an initial surface ice layer over dry regolith with impact gardening as the only external forcing mechanism. However, the actual history of the Moon is obviously far more complex. Figure 4.1.2 shows preliminary results for the same scenario from the UCF model. This result suggests that the first meter of icy regolith exceeds the preliminary 4% ice concentration threshold for Thermal Mining viability.

As this work progresses and becomes anchored with ground truth data from the lunar PSRs, it will provide valuable insight into the distribution and nature of the volatile deposits and enable the refinement of the Thermal Mining system.

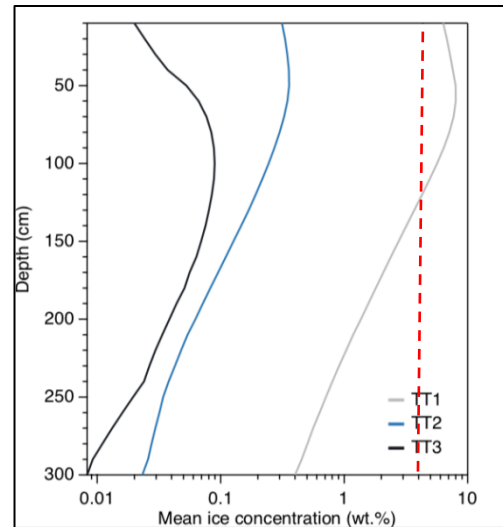


Figure 4.1.2. Comparison of ice concentration vs depth for three lunar terrain types. Terrain Type 1 (TT1) represents a PSR. The red vertical line is the 4wt% threshold of Thermal Mining viability [Cannon & Britt, 2020].

4.2 System Architecture

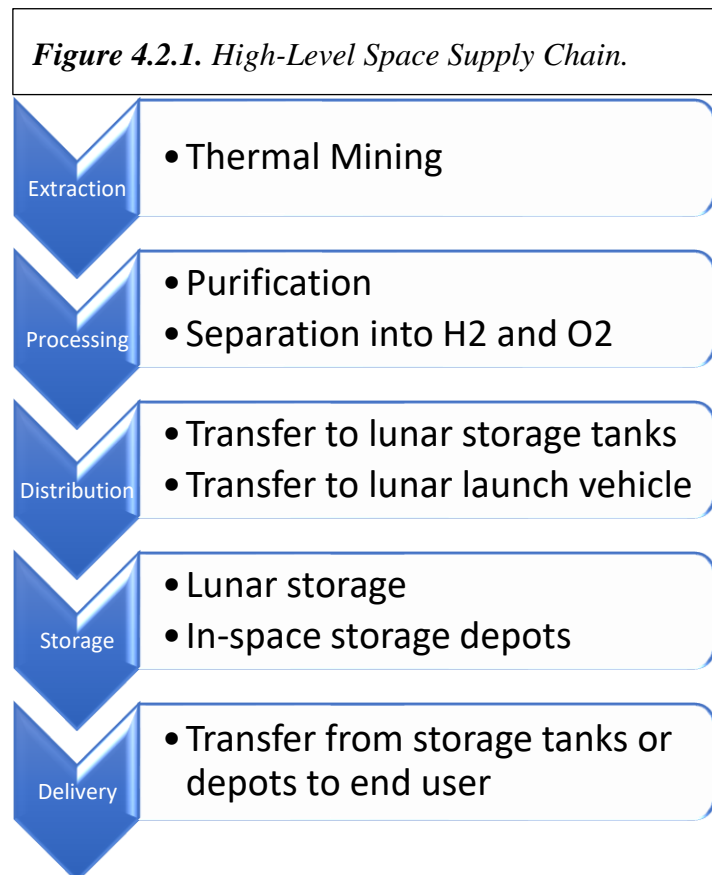
Volatiles such as water and methane are key to the sustainability of space exploration and will underpin most economic activities in space. Volatiles are essential for life and can be used as rocket propellants. Volatiles are common throughout the solar system and exist in many forms, especially ices frozen on cold bodies. Developing sources of volatiles in space will dramatically lower the cost of exploration and enable robotic and human spaceflight missions not currently possible and/or affordable.

Water, in particular, is ubiquitous in the inner solar system. It exists on Mercury, the Moon, many asteroids and Mars. Recent findings [Li, et. al. 2018] indicate water ice is present on the surface of the Moon within the permanently shadowed regions (PSRs) in concentrations up to 30% by mass (Figure 4.0.1). The presence of rich ice deposits on Earth’s nearest extraterrestrial neighbor is a potential game changer in the exploration and development of the solar system.

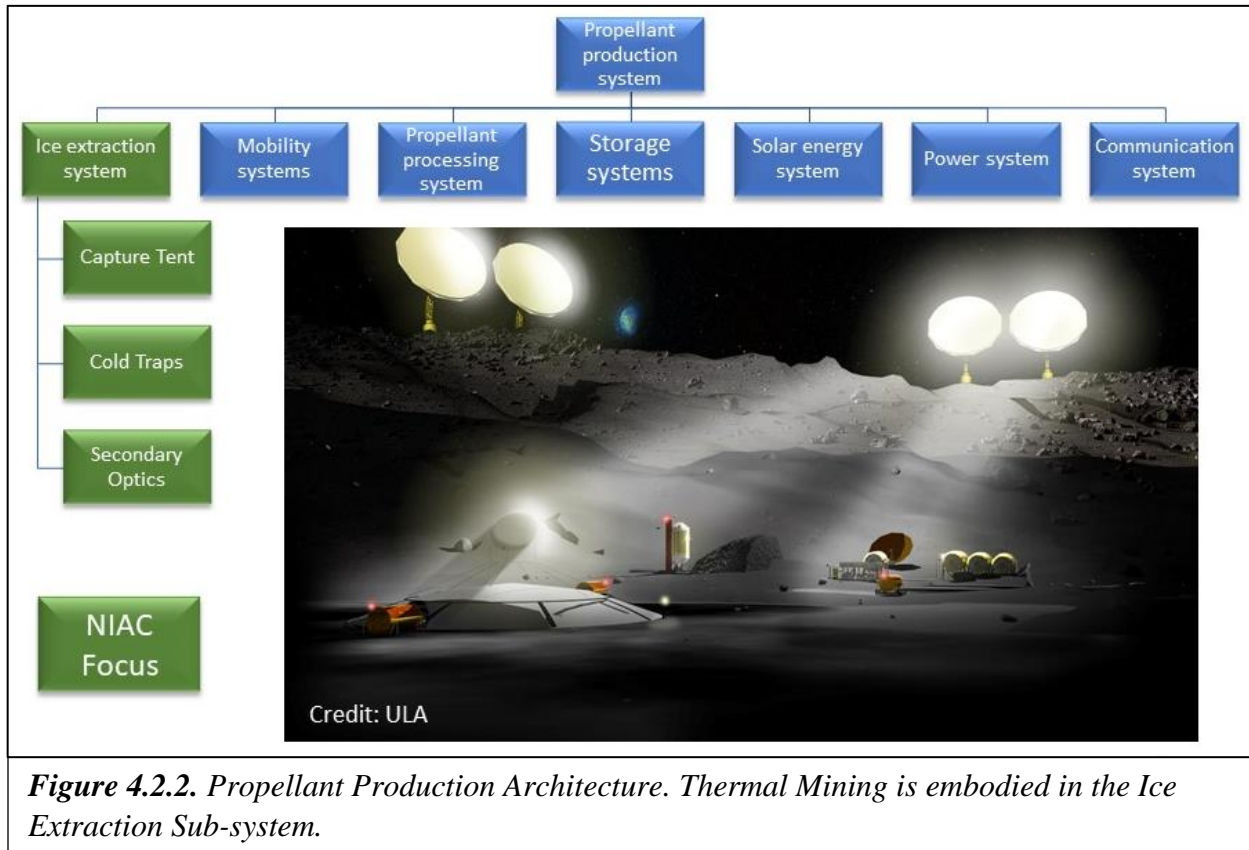
Water has many uses in the context of space exploration and development. It is essential for human life and agriculture. Oxygen, one of its constituents, is a necessary component of breathing air. It is one of the most effective substances for radiation shielding on a per mass basis. But perhaps its most valuable use is as rocket propellant. It can be used directly in the form of steam or plasma for low to medium thrust applications. When split into hydrogen and oxygen and liquefied, it produces LO₂ and LH₂, the most efficient chemical propellants known. Water is truly the oil of space. And like oil on Earth, water will be the foundation of the space economy.

Extracting volatiles from cold solar system bodies will be challenging. Traditional excavation methods require heavy machinery capable of operating in extreme cold, vacuum and dust exposure. Small bodies entail very low gravity. Excavation approaches will be costly to build, deploy and maintain. However, direct heating of volatile bearing materials via Thermal Mining can save the cost and mass of excavation systems as well as eliminate most of the active components of the system, enhancing reliability and maintainability.

Thermal Mining of volatiles exists at the front end of an in-space supply chain for vehicle propellant (liquid hydrogen and liquid oxygen), purified water for life support, oxygen for life support and manufacturing, and other commodities. An in-space supply chain for space-sourced materials will dramatically lower the cost of almost



every space activity beyond low-Earth orbit by eliminating the need to deliver materials from Earth. A high-level space supply chain is shown in Figure 4.2.1.



The supply chain architecture has hardware components on the lunar surface, in cislunar space, and on Earth. The propellant processing system, which was the focus of this NIAC study, is located on the lunar surface and consists of several subsystems. The propellant production system architecture is shown in Figure 4.2.2. The Thermal Mining system is a subsystem of a production facility for oxygen, water, propellant, or other commodities derived from the extracted volatiles. The Thermal Mining system is positioned on an ice-rich location identified and characterized by a resource exploration campaign. Volatile materials are extracted from the site and transported to a processing facility adjacent to a launch and landing facility to enable the processed commodity to be transported to the point of use, either on the lunar surface or in space.

The Thermal Mining ice extraction system uses heat to warm the frozen material to sublimate the volatile, releasing it from the surface in the form of vapor. Heat to warm the material can be applied in many ways depending on the nature of the local geography and the volatile-bearing material. The simplest is to heat the surface directly using sunlight as shown in Figure 4.2.3. The sunlight may or may not be concentrated or reflected depending on the geography, type of material, and required heating rates. In the example shown in Figure 4.2.3, the Capture Tent is located inside a permanently shadowed region (PSR) of a lunar crater. Sunlight is reflected from adjustable heliostats on the rim of the crater to the crater floor to warm the surface. If surface heating is insufficient, subsurface heating can be accomplished by driving conducting rods into the first few meters of the material, which provides a conduction path for heat into the material

and a path for the sublimated vapor to escape. Additional subsurface heating could be applied via electrical heaters emplaced in boreholes or via resistive heating by passing a current through the material. The latter two methods require drilling boreholes into the material, which increases the complexity of the system. Another alternative is to use electrically generated microwaves to heat the surface.

The vapor captured by the Thermal Mining system will not be pure water; other volatiles are present in lunar PSRs. In addition to water, these volatiles include hydrogen sulfide, hydrogen gas, carbon monoxide, calcium, ammonia, mercury, and others (see Table 4.0.1). These volatiles may eventually be valuable enough to collect. Ammonia could be used as fertilizer for hydroponic plants, and carbon could be captured for use in the production of polymers. However, these volatiles are contaminants in the process of producing propellant from water vapor and the collection of them should be minimized. This may be possible through a technique called fractional freezing, which exploits the difference in freezing points of the various volatiles to selectively capture only, or at least mostly, water vapor.

To capture the vapor produced by heating the surface or subsurface, a tent structure called the Capture Tent is placed over the surface where the heating occurs. For the surface heating method, secondary optics are located above the tent to direct sunlight through a transparent top to the surface. The sublimation rate is controlled to keep the pressure in the tent very low and the inner tent surface is reflective to trap as

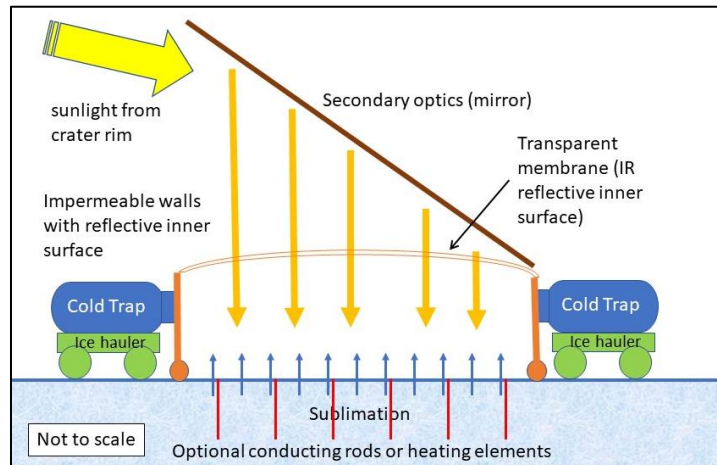


Figure 4.2.3. Ice extraction concept.

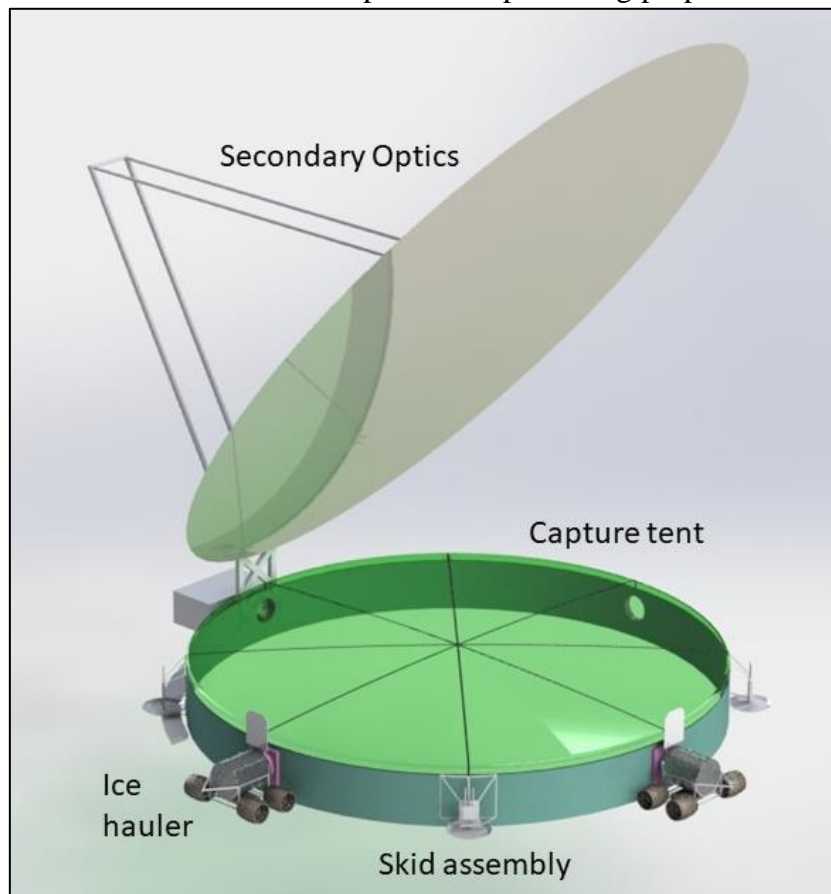
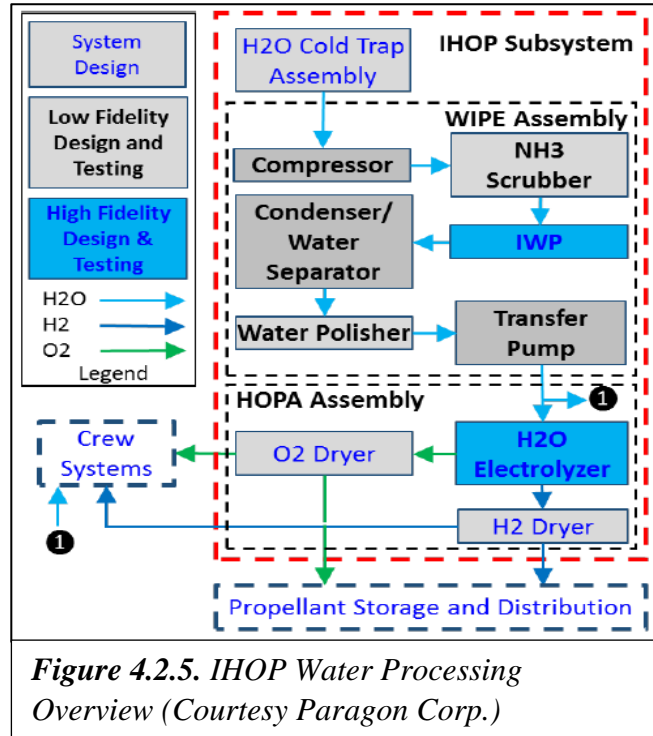


Figure 4.2.4. Ice extraction subsystem.

much heat as possible and to keep vapor from freezing on the inner surface. The vapor migrates from the tent interior into attached cold traps through large openings, where it then refreezes. The ice-filled cold traps are then transported to a central facility for processing. Once the surface under the tent is depleted of volatiles, the tent is moved to a new location. Figure 4.2.4 shows a CAD representation of the ice extraction subsystem.

Once the frozen vapor is deposited into the processing facility, it is processed to purify and electrolyze it into H₂ and O₂. Paragon Space Development Corporation has partnered with Giner Labs Inc. to develop the ISRU-derived water purification and Hydrogen Oxygen Production system, or IHOP, under a NASA NextSTEP-2 Broad Area Announcement (BAA) contract. The IHOP process begins with water purification using a membrane distillation architecture. This step removes any remaining volatiles in the vapor state, before passing the water vapor through an ammonia scrubber, water polisher and condenser, and then a transfer pump to move the liquid water into the electrolyzer. The electrolyzer then uses an electric current to decompose the water into gaseous hydrogen and oxygen, which are separated and dried. The gases can then be cooled to liquify the hydrogen and oxygen, and they are ready for transfer into the storage containers. See Figure 4.2.5 for a schematic of the Paragon IHOP process.



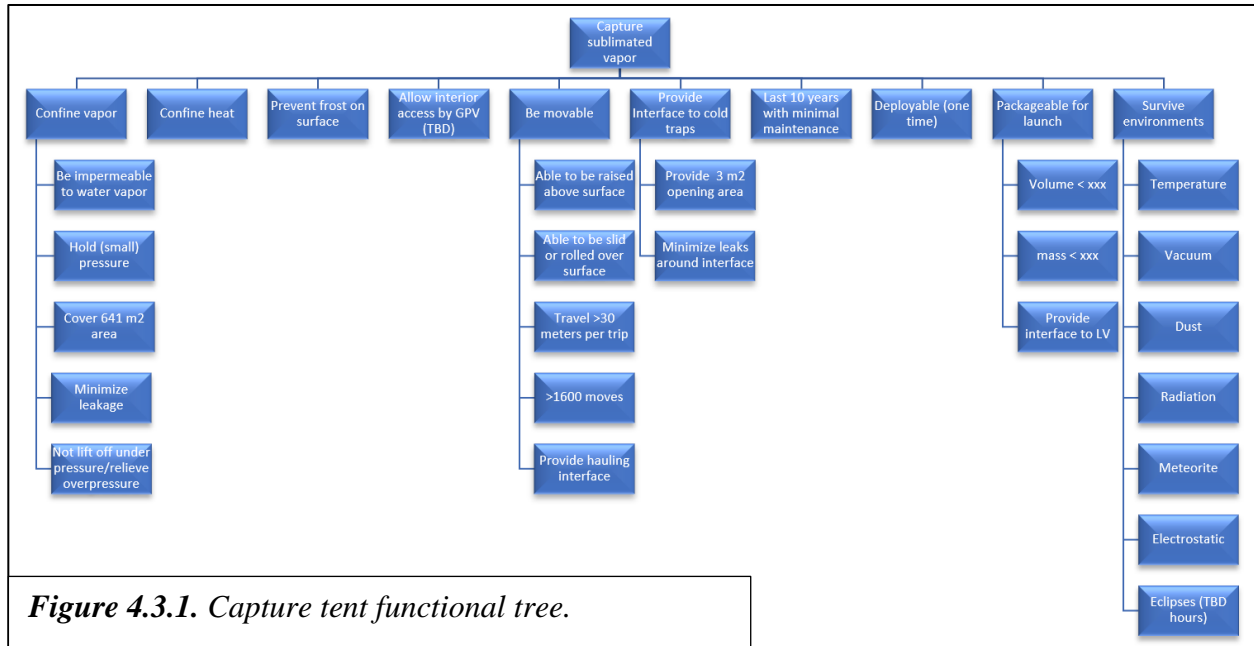
gaseous hydrogen and oxygen, which are separated and dried. The gases can then be cooled to liquify the hydrogen and oxygen, and they are ready for transfer into the storage containers. See Figure 4.2.5 for a schematic of the Paragon IHOP process.

4.3 Functional Analysis

As described in Section 4.2, the Thermal Mining system is the front end of a space supply chain for volatiles, especially water or hydrogen and oxygen for propellant. The ice extraction subsystem is part of the overall volatile or propellant production system (see Figure 4.2.2) and was the focus of this NIAC study. This subsystem is made up of three sub-subsystems: the Capture Tent, the cold trap haulers, and the secondary optics.

Capture Tent

The Capture Tent is a deployable structure that is placed on the lunar surface. Sunlight reflected from heliostats and the secondary optics enters the tent through the transparent top. The sunlight warms the lunar surface, releasing volatiles, which are captured by the Capture Tent. Openings in the tent lead to cold traps, which capture the volatiles. Once the surface under the tent is depleted, the tent is moved to the next location. The functional tree for the capture tent is shown in Figure 4.3.1.



The top-level function for the capture tent is to capture the vapor sublimated from the surface. To confine the vapor, the material of the tent must be impermeable to it. The tent must also be able to hold the small pressure of the volatiles released into the tent without lifting off the surface; this implies that the tent must have some kind of pressure release mechanism but must also minimize inadvertent leak areas. The tent area must cover 641 square meters, based on the economic analysis of a feasible system, which translates into a diameter of 30 meters. The tent must be able to confine the heat provided by the reflected sunlight in order to effectively warm the lunar surface and release volatiles. As vapors are released into the (relatively) warm tent, they will freeze onto the nearest cold surface. The tent must be designed such that the tent walls prevent the vapors from freezing onto them instead of inside the cold traps.

To function as part of the overall ice extraction system, the capture tent has several interface functions. It may be desirable for the general-purpose vehicles (GPVs) to be able to access the interior of the tent to perform maintenance, scrape off desiccated regolith to release additional volatiles, or for other reasons; therefore, the tent will need access provisions for the GPVs. The tent must also be movable. Once the lunar surface in a location is depleted, the tent will be moved to a new location by the cold trap haulers. To allow for mobility over uneven, rocky terrain, the tent must be able to be raised above the surface. It must be able to be moved over the surface, either by rolling or sliding. The tent will be moved a certain distance per trip—likely around 30 meters to a site adjacent to its current location—and will make nearly 1600 moves over its lifetime. Since the tent will not provide its own mobility system, it must have an interface for the cold trap haulers to attach to it and move it. The tent must also have an interface for the cold trap haulers to attach the cold traps so the vapor can be captured. The openings on the interfaces must be 3 square meters (to minimize internal pressure) and leaks between the tent and cold trap must be minimized to preserve as much of the volatile material as possible.

The tent must also be capable of getting to the lunar surface, deploying, and surviving in the lunar environment. Maintenance will be limited, so the tent must be able to survive and function

for at least 10 years with minimal maintenance. The tent must be able to be packaged for launch; the launch vehicle is TBD but it will have to meet mass and volume requirements provided by the launch vehicle, as well as an interface to the launch vehicle. Once the tent arrives on the lunar surface, it must be deployable either on its own or with assistance from the GPV and cold trap haulers. It must also survive the harsh lunar environment, including low temperature, vacuum, dust, radiation, meteorite strikes, electrostatics, and possible eclipses; these environments will be determined by the actual mining location.

Cold Trap Haulers

The cold trap haulers are robotic systems that perform several functions. Their primary function is to remove the vapor captured in the capture tent by providing a cold trap. Once the vapor is frozen inside the cold trap, the cold trap hauler will move the volatiles to a processing facility. The cold trap haulers will also assist with deployment and repositioning of the Capture Tent and secondary optics. The functional tree for the cold trap haulers is shown in Figure 4.3.2.

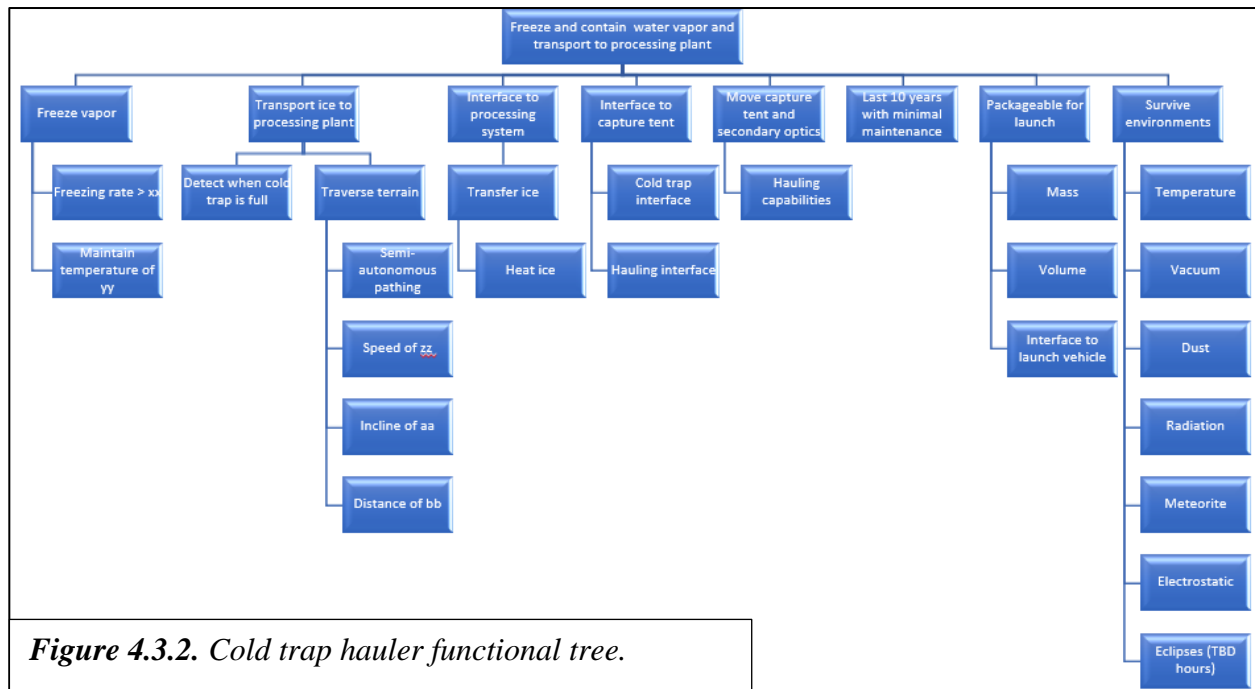


Figure 4.3.2. Cold trap hauler functional tree.

As mentioned, the cold trap haulers’ primary purpose is to extract and freeze volatiles captured by the Capture Tent. The cold traps must maintain a set temperature, which is TBD, to freeze the volatiles at the appropriate rate. The cold trap hauler must also be able to detect when it is full so it can detach from the tent and move the cold trap to the processing facility. The hauler must be able to navigate the terrain around the mining site, which could include rocks or loose regolith and may be on an incline, at a speed that is safe but efficient. Navigation is likely to be semi-autonomous, which implies some level of control from Earth operators. The haulers’ batteries will be charged at the processing facility so they must be capable of making the trip from the processing facility to the tent and back on a single charge; the maximum distance between the tent and the facility is 2000m. See Section 4.7.

The cold trap haulers must be able to interface with both the processing facility and the Capture Tent. At the processing facility, the cold traps must interface with the facility and be able to heat the ice to sublimate it back into vapor for transfer into the processing facility. The haulers must also interface with the Capture Tent at the cold trap interface in order to capture the volatiles. The haulers will also provide mobility assistance to the secondary optics and capture tent so they can be repositioned after depleting each surface location. The haulers must possess towing capability to move the tent and secondary optics; in addition to being able to interface with the tent and optics, this implies requirements for torque and traction on the haulers' mobility system.

As with the Capture Tent, the cold trap haulers must be able to operate on the lunar surface with minimal maintenance. They must be packageable for launch and able to survive and operate in the lunar environment.

Secondary Optics

The secondary optics is a freestanding reflector that directs incoming sunlight from the heliostats into the capture tent. The secondary optics will be positioned next to the capture tent and will be repositioned after site depletion along with the tent. The functional tree for the secondary optics is shown in Figure 4.3.3.

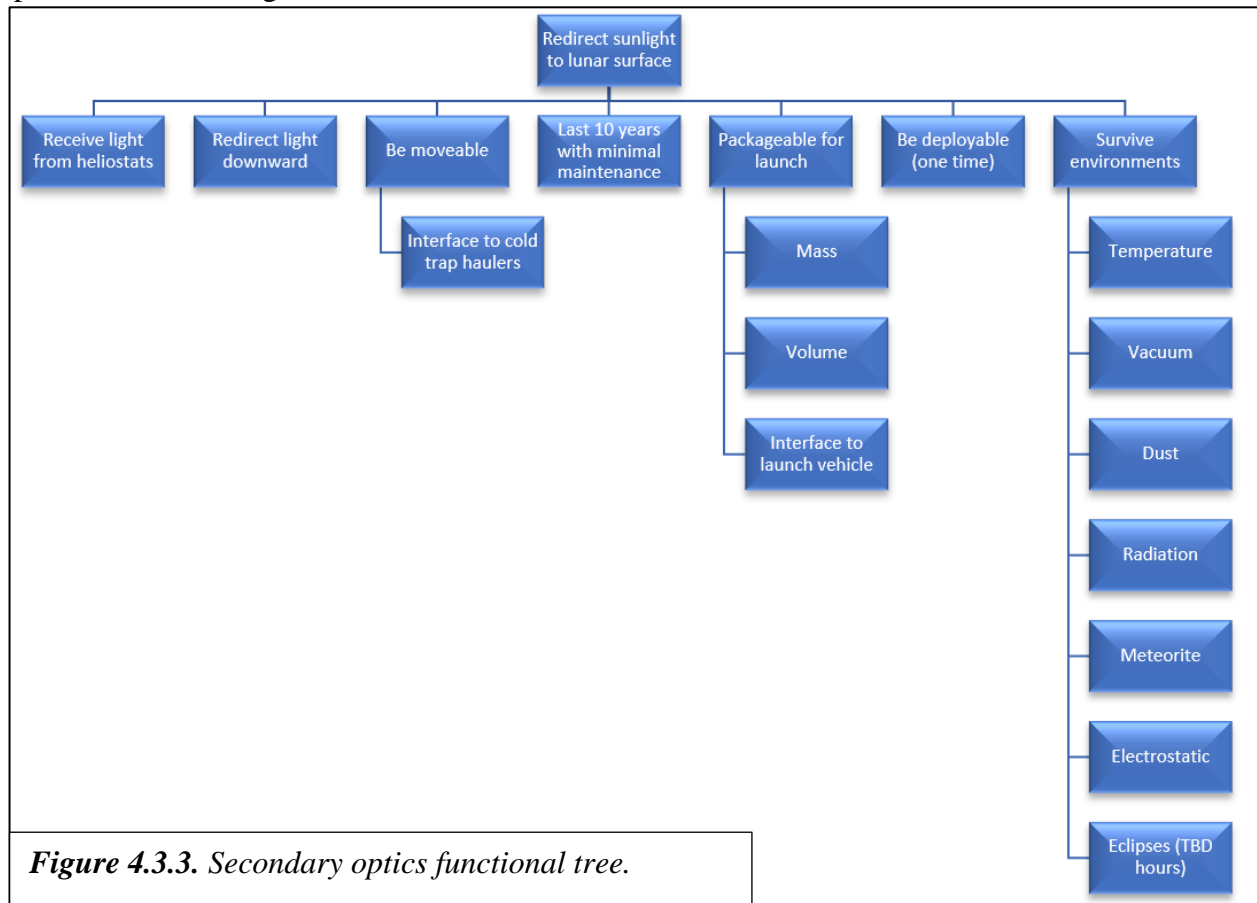


Figure 4.3.3. Secondary optics functional tree.

The secondary optics' primary function is to redirect light from the heliostats into the Capture Tent. It must receive light from the heliostats, which implies that it must be adjustable since the heliostats are stationary on the crater rim and the secondary optics will move around

within the lunar crater. Once the secondary optics have received sunlight, it must reflect it downward into the tent. The shape of the optics must focus the incoming light to approximately the footprint of the tent; this will maximize the heating potential of the surface without spilling outside the tent and releasing volatiles into space.

Since the secondary optics must be positioned next to the capture tent, they must also be moveable. The cold trap haulers will provide mobility for the secondary optics, so the structure must include a towing interface.

Like the other subcomponents, the secondary optics must be able to survive for 10 years with minimal maintenance. This is especially critical for the reflective surface; since the structure is tall and the mirror is very large, robotic maintenance of that surface may be challenging. The optics must be packageable for launch and it must be deployable on the lunar surface. It must also be able to survive the lunar environment.

4.4 Ice Extraction Subsystem

This section will provide more detail about the components of the ice extraction subsystem. This subsystem is comprised of three subcomponents; the Capture Tent, the secondary optics, and the cold trap haulers.

Capture Tent

The first component of the ice extraction system is the Capture Tent. As described in section 4.3, the Capture Tent sits on top of the lunar surface. Reflected sunlight enters the tent, which releases volatiles that are confined within the tent before being frozen on the cold traps, which interface with the tent. Once the lunar surface below the tent is depleted of volatiles, the

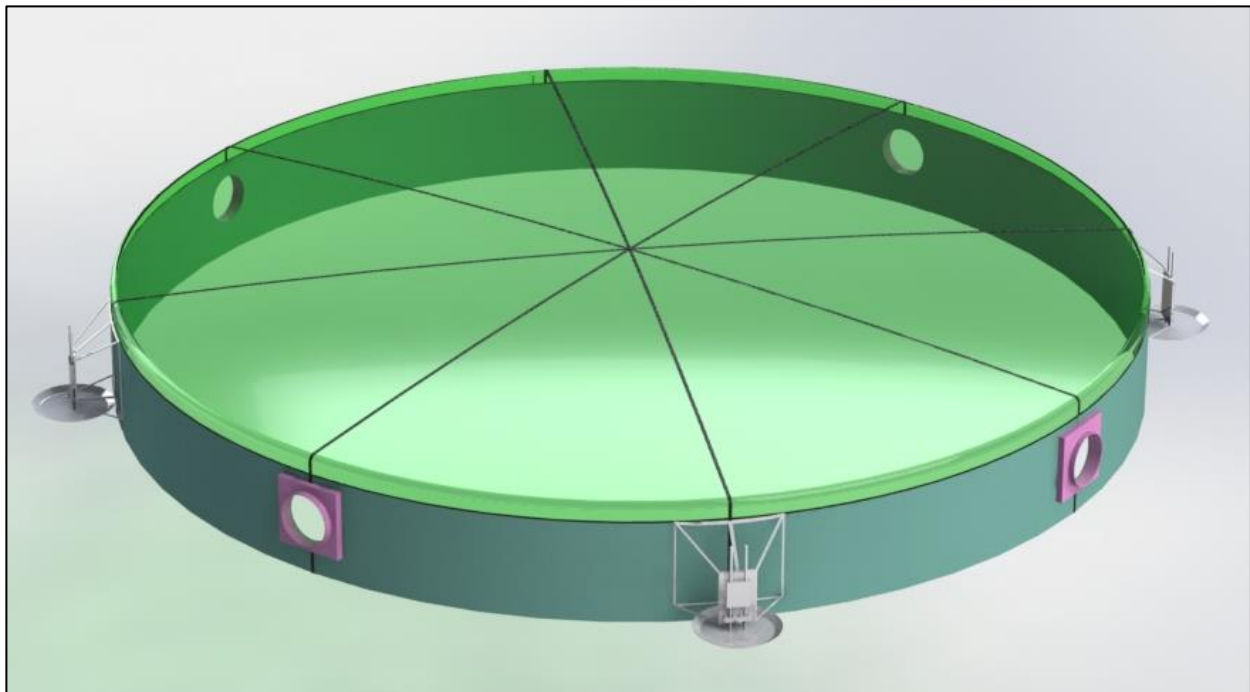
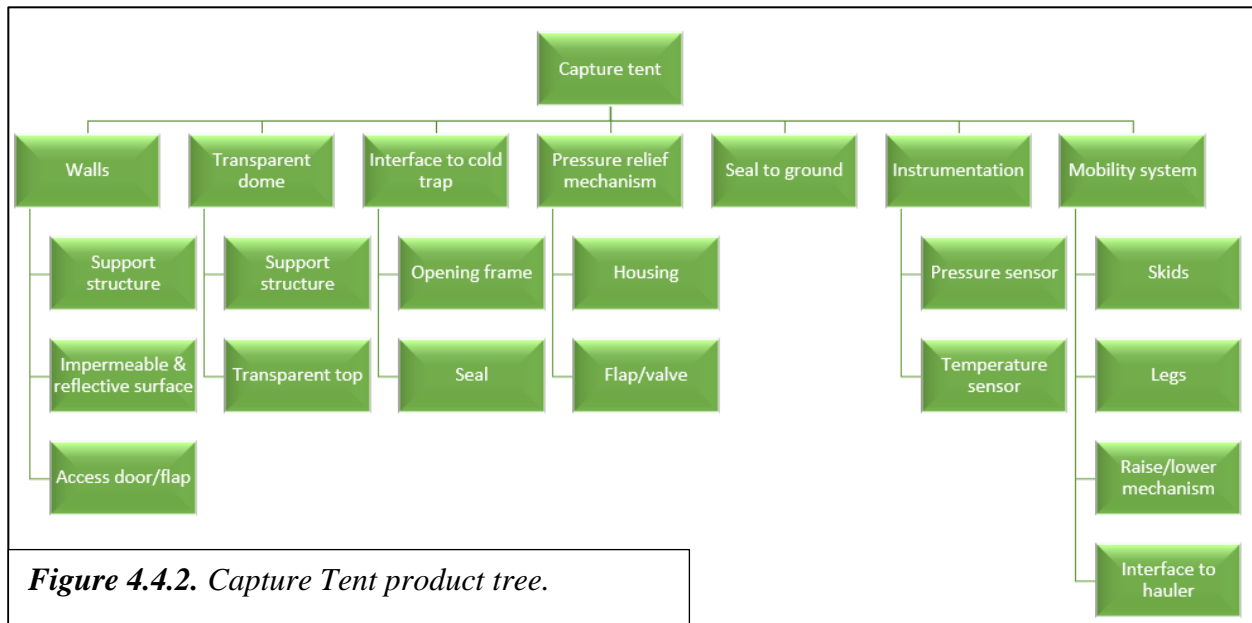


Figure 4.4.1. The Capture Tent.

cold trap haulers drag the tent to a new location. The overall tent diameter is 30 meters and the height in the middle of the dome is 4 meters. Figure 4.4.1 shows a CAD model of the capture tent. Figure 4.4.2 shows the capture tent product tree.



The capture tent walls are comprised of three components: a support structure, the tent wall material, and possibly an access door. The support structure, shown in black in Figure 4.4.1, provides the tent's shape and may be integrated with the support structure of the tent's transparent dome. The structure must be able to be folded to fit inside a launch vehicle fairing and then must deploy on the lunar surface. The design of the deployable structure will be continued by Paragon Corp. in as the project progresses. Some possible structural options include single-use inflatable tubes or umbrella-type deployment seen on some large communication satellite antennas. The deployed structure must provide enough rigidity to maintain the shape of the tent while it is being dragged across the lunar surface by the cold trap haulers. The material for the tent walls is a critical design consideration for the overall effectiveness of the capture tent. The material must be lightweight to minimize launch costs and must be able to be folded to fit inside a launch vehicle fairing. The inside of the material should be reflective to light and thermal energy to retain as much heat as possible to warm the lunar surface. The material must be impermeable or else vaporized volatiles could escape the tent before being captured by the cold traps. The tent must also resist the formation of frost; any frost formed on the tent walls represents water that cannot be captured by the cold traps, and will also add weight to the tent, potentially making it harder to transport. Finally, it may be necessary for the capture tent walls to have an access door or flap so the general purpose vehicle (GPV) can access the interior of the tent. The access door must be able to be opened and closed either on its own or by the GPV and must remain tightly sealed when not in use.

The next subcomponent of the capture tent is the dome structure that forms the top of the tent. Like the tent walls, the dome has a support structure that must be able to be folded to fit inside a launch vehicle and then deployed on the lunar surface. Once deployed, the structure must keep the dome rigid enough to hold its shape during transport to a new tent location. The dome itself

must be transparent to the reflected sunlight coming in from the secondary optics but should be reflective to thermal energy already inside the tent. This combination is commonly used in terrestrial green houses. This will improve the efficiency of the thermal energy captured to more effectively heat the surface and release volatiles. The dome material should also be resistant to the effects of micrometeorite impacts; this could result in a material that is repairable by the GPVs, a ‘self-healing’ material that can re-seal in the event of a puncture, or a material similar to ripstop nylon that will halt the progression of a hole.

Once the volatiles in the lunar surface have been vaporized by the redirected sunlight, they will be captured by the cold traps; therefore, the capture tent must interface to the cold traps. The cold trap interfaces are 1.5 meters in diameter and consist of a large seal and a frame to hold the seal onto the walls of the capture tent. A flap or door to close the interface when not in use may also be necessary if the leak rate of having open interfaces is too great. The cold trap haulers will approach the capture tent and press the opening of the cold trap against the seal to provide a clear path for the vapor to escape the tent and be captured by the cold traps. The current tent design has four interface locations, although the number could be further optimized. Additional interfaces add complexity and mass and may hinder the ability to fold the tent into a fairing for launch. However, more interfaces are useful logistically; the cold trap haulers could use interfaces close to the processing facility instead of having to drive all the way around the tent, and some interfaces may be undesirable in some tent locations due to large rocks, craters, or other terrain features that render an interface inaccessible.

As vapor is released from the lunar surface, the pressure in the tent will increase. Although the pressure will be very low, the light weight of the capture tent coupled with the low lunar gravity could be enough to eventually lift the tent off the lunar surface. To prevent that from happening, the tent must have some way to release pressure. A simple pressure valve or flap would likely be sufficient.

Although the lunar terrain is rocky and uneven, the tent must be able to seal to the ground to limit the amount of valuable volatile vapor lost to the vacuum of space. The GPVs can be used to remove large rocks from the perimeter of the mining area, but some small craters and rocks are unavoidable. The bottom of the tent must be soft to seal as best as possible against the lunar surface. Our current point design contains an allocation for leak area of 10% of the opening area to the cold traps.

The pressure and temperature within the tent are important parameters; the tent will lift off or “burp” if the pressure gets too high and the temperature of the tent walls is important to ensure that frost cannot form on them. The tent must be equipped with simple instrumentation to monitor the pressure and temperature within the capture tent. This information could be used to adjust the amount of sunlight reflected into the capture tent by the secondary optics.

Finally, the capture tent requires a mobility system so it can be moved to new locations as patches of the lunar surface are depleted of volatiles. The tent will be dragged across the surface by the cold trap haulers, so the tent must have skids or wheels to allow it to be moved over the surface. Wheels lower the amount of drag on the tent, but they also add complication; wheels require bearings and lubrication which can become contaminated with lunar dust. Skids are much simpler and, since the tent is lightweight and gravity on the Moon is low, are likely a better option. Circular skids allow the tent to be dragged in any direction, and an angled lip around the skid will

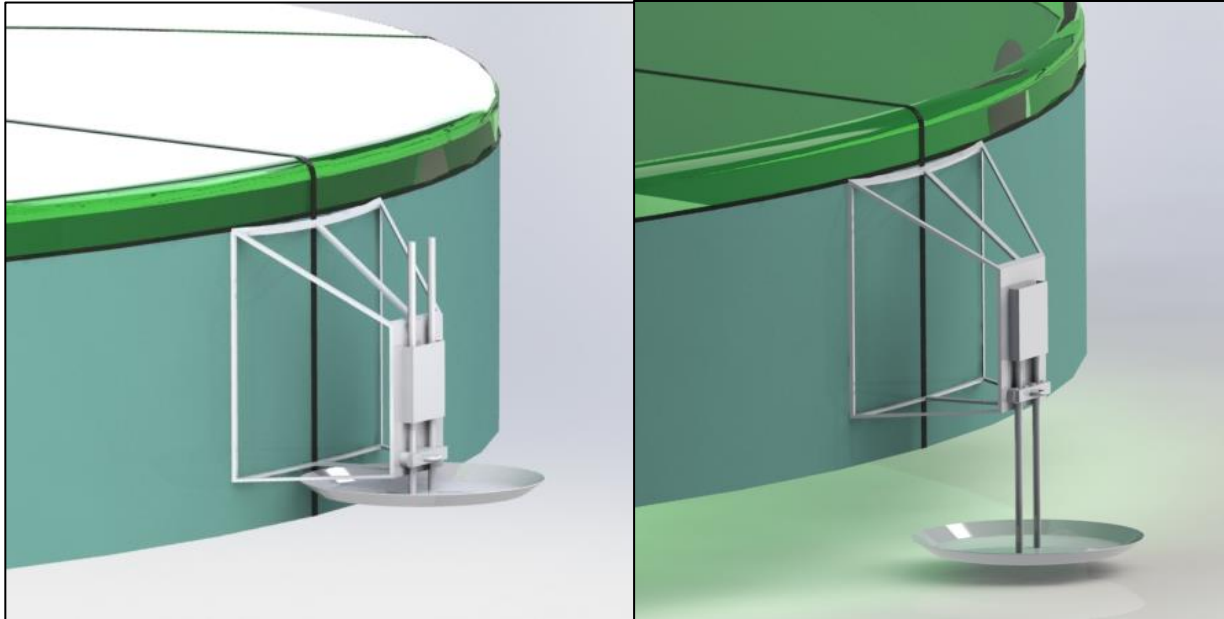


Figure 4.4.3. Capture tent legs in lowered tent (left) and raised tent (right) positions.

prevent it from getting caught on rocks. The bottom of the skid must be smooth to allow it to slide over the lunar surface as easily as possible but must also be robust to withstand the abrasive effects of lunar soil. The skids will attach to the tent via sturdy yet lightweight supports and legs. These supports will hold the skids outside the perimeter of the tent, so the tent doesn't have to seal around the skid. The skid supports will also have interface provisions for the cold trap haulers to attach to the tent so it can be moved. The current design shows a simple hook and ring system, but other attachment structures may be more effective. As mentioned before, the lunar surface is rough so the tent must be able to be raised to allow it to pass over small boulders and small elevation changes, and then lowered to seal once it reaches its new location. This will necessitate some kind of raising and lowering mechanism that can be operated by the GPVs or cold trap haulers. Figure 4.4.3 shows the tent in the lowered (left) and raised (right) position. The raised position puts the bottom of the capture tent seal 1 meter above the lunar surface, but that requirement may be optimized once further assessment of the lunar terrain at the mining site is performed.

Cold Trap Haulers

The second subcomponent of the ice extraction subsystem are the cold trap haulers. The cold trap haulers are multifunction robotic vehicles that house the cold traps, move the cold traps from the capture tent to the processing facility, and move the capture tent and secondary optics to new mining locations. The current system requires three cold trap haulers to reduce downtime (see Section 4.7). Figure 4.4.4 shows a CAD model of a cold trap hauler and Figure 4.4.5 shows the cold trap hauler product tree.

The first component of the cold trap hauler is the cold trap itself. The cold trap is a large cylindrical structure, 2 meters in diameter and 2.5 meters long. The cold trap has an internal structure and an external structure. The inside of the cold trap is where vapor will collect and condense into solid ice for transport to the processing facility, and the more surface area available

for vapor to condense on, the more ice can be transported in a single trip. Therefore, the internal structure of the cold trap is equipped with fins to maximize surface area. The exterior of the cold trap is insulated to maintain the correct temperature inside the cold trap. It also includes a cover that can be opened to interface with the capture tent and the processing facility and closed during transport to prevent dust from contaminating the ice. The opened cover can also provide additional shading for the cold trap during vapor capture; spillover sunlight from the secondary optics could heat the cold traps, reducing their effectiveness. Figure 4.4.4 shows the cold trap cover in the opened position.



Figure 4.4.4. Cold trap hauler.

The mobility system of the cold trap haulers is a critical component. Large, tough wheels will be necessary to traverse the rough terrain of the lunar surface. Wheel bearings must be sealed to prevent dust intrusion. The motor of the cold trap haulers must provide sufficient torque to move a full hauler over the lunar terrain, as well as tow the capture tent and secondary optics. The haulers will be capable of semiautonomous operation but will require at least some input from human operators on Earth. Human operators will need to see the terrain to navigate it, so cameras and lights, located near each wheel as well as on the front and back of the hauler to facilitate interfacing

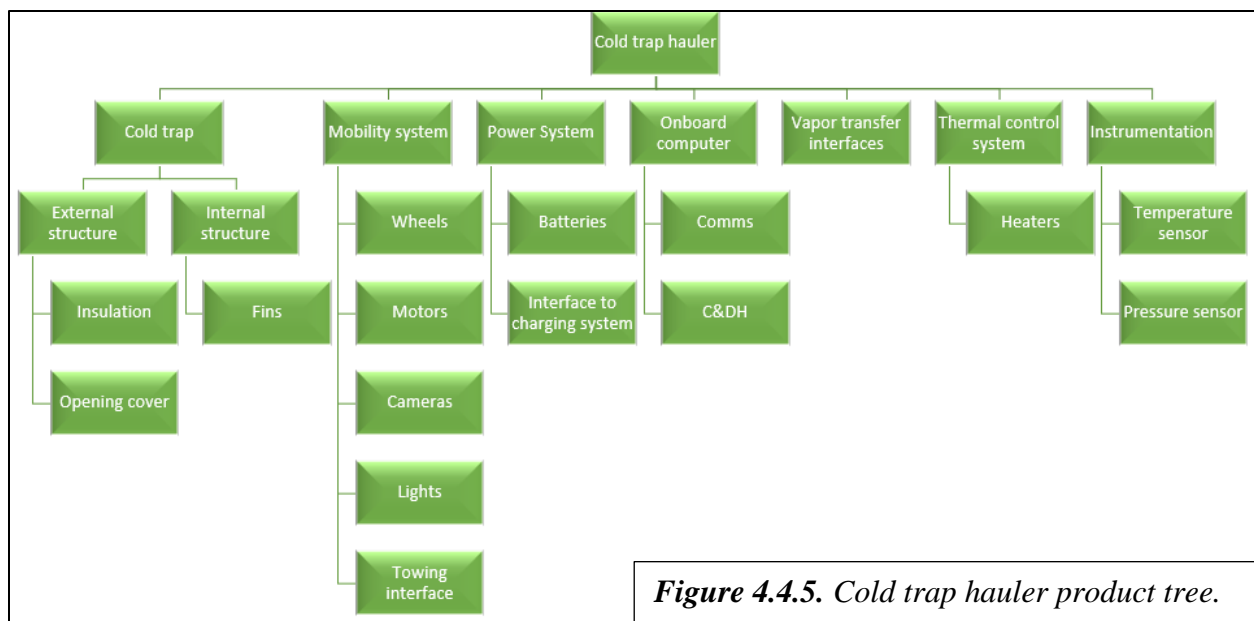


Figure 4.4.5. Cold trap hauler product tree.

with other subsystems, will be necessary. The hauler will also require a towing interface to be able to attach to the capture tent and secondary optics for hauling operations.

The cold trap haulers are the only subcomponent of the ice extraction system to require a substantial power supply. Power will be required to operate the hauler’s motor, cameras, lights, communications, onboard computer, thermal control system, and instrumentation. Since the haulers will be operating in darkness, they will require large batteries to store power. The haulers will charge their batteries at the processing plant while they are offloading ice (see Section 4.7), so an interface to the charger near the vapor transfer interface will be required.

As mentioned, the haulers will be capable of semiautonomous operation. Simple path planning, especially over heavily traversed areas of the mining area, may be able to be performed autonomously using onboard software. However, when the hauler needs to carefully navigate around obstacles, interface with the processing facility, tow the capture tent and secondary optics, or perform other critical functions, human operation may reduce the risk of damage. To accept commands from terrestrial operators, the haulers will require communications.

The vapor transfer interface is the port through which vapor enters the cold trap from the capture tent and exits the cold trap into the processing facility. The opening is 1.5 meters in diameter and will be pressed against the interface on the capture tent or processing facility to form a seal to prevent vapor from escaping into space.

The cold trap hauler thermal control system performs two critical function. First, heaters will likely be required to keep the onboard computer and motors warm enough to function in the cryogenic environment of the PSR. Second, heaters will be necessary to control the temperature of the cold trap. The heaters will be inactive during regolith heating at the capture tent to keep the cold traps as cold as possible to maximize vapor capture. Once the cold trap is at the processing facility, the interior of the cold trap will be heated to sublimate the ice back into vapor for transfer into the processing facility.

Instrumentation will be required to ensure optimal functioning of the cold trap haulers. This instrumentation will include temperature sensors around the haulers and inside the cold trap. A pressure sensor may also be necessary to monitor pressure inside the cold trap.

Secondary Optics

The third subcomponent of the ice extraction subsystem is the secondary optics. The secondary optics redirect light coming in from the heliostats on the crater rim into the capture tent. The secondary optics is a freestanding structure that will be positioned next to the capture tent. The reflective mirror is positioned above the tent, so the reflected sunlight shines directly into the tent,

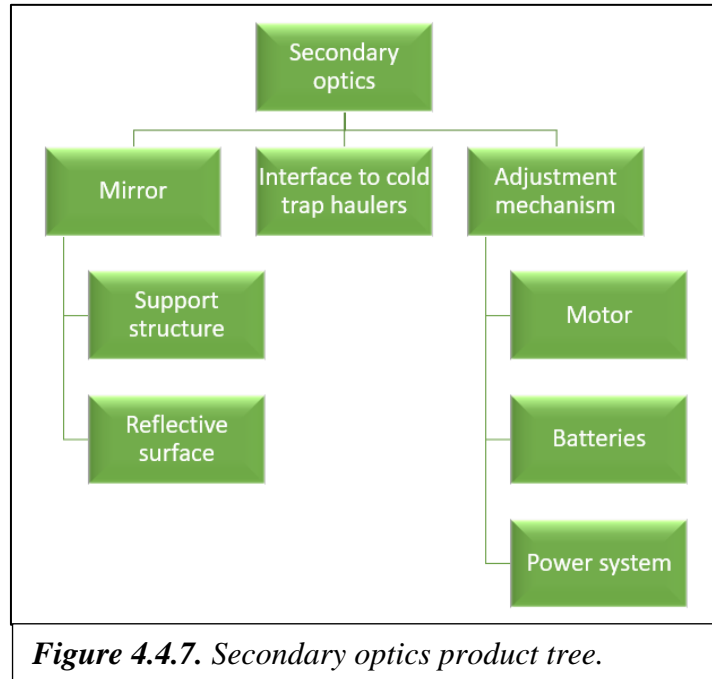


Figure 4.4.6. Secondary optics.

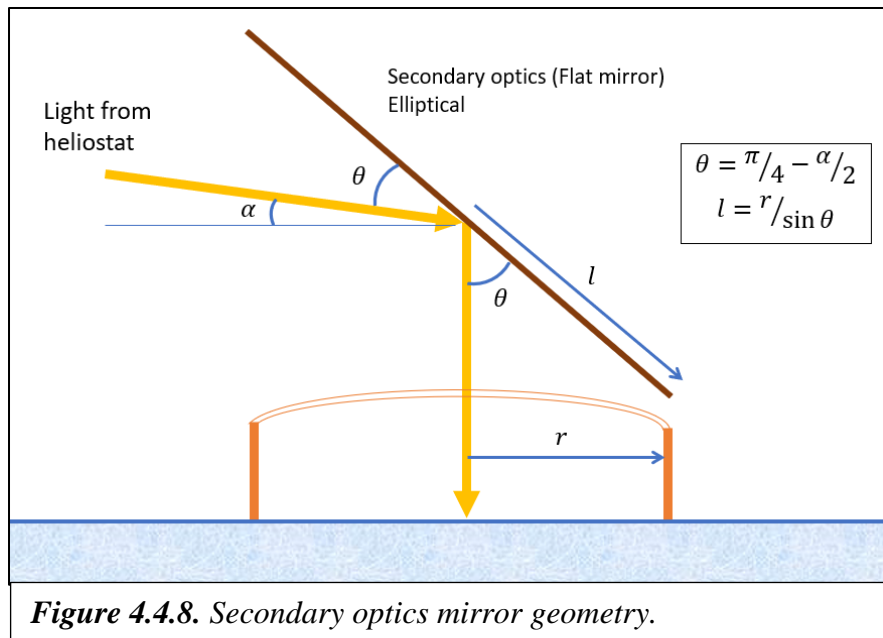
illuminating and heating as much of the lunar surface under the tent as possible. The total height of the secondary optics varies depending on how the reflective mirror is angled but can be over 40 meters tall. Figure 4.4.6 shows a CAD representation of the secondary optics, and Figure 4.4.7 shows the secondary optics product tree.

The first subcomponent of the secondary optics is the reflective mirror. The mirror is shaped like an ellipse, measuring 30 meters wide and 46.6 meters long. The width of the mirror is the same as the diameter of the capture tent. The length of the mirror was determined according to the geometry shown in Figure 4.4.8.

The mirror, like the rest of the ice mining components, must be able to be folded to fit inside a launch vehicle payload fairing. The face of the mirror must be highly reflective to maximize the amount of light directed from the heliostats onto the lunar surface. The material must also be able to withstand micrometeorite impacts, either by self-healing small punctures or by preventing small holes from becoming large tears. Since the secondary optics is so large, repairs by the GPV will be challenging; the material must be able to function without repairs for as long as possible. The material must also be lightweight, both to minimize launch costs and to ease the requirements for towing on the cold trap haulers. Since the mirror is cantilevered over the capture tent, the secondary optics structure must be weighted to



prevent it from tipping over; a lighter mirror will lower the weight of the secondary optics structure. One possibility to lower the weight is for the secondary optics structure to include a provision for holding lunar rocks; this provision is shown in Figure 4.4.6 as a box on the base of the structure. This container would be launched empty to reduce weight and then filled with lunar rocks and



regolith to provide additional weight to the structure without increasing launch costs. The secondary optics structure must be tall enough to hold the mirror above the capture tent and rigid and heavy enough to keep the secondary optics from tipping over. The base of the structure must allow the optics to sit right up against the perimeter of the tent to maximize the area under the tent warmed by the reflected light.

Like the Capture Tent, the secondary optics must move to new locations as the lunar surface is depleted. Therefore, the structure of the secondary optics must include a provision to interface with the cold trap haulers for towing. One possible design could involve the cold trap haulers removing the rock container from the base of the structure to lower the weight for towing. The cold trap hauler could jack up the apex of the curved base, thus tipping the optics forward slightly, and dragging it across the surface to the new location. Skids may also be included under the base to facilitate towing.

The final component of the Capture Tent is the adjustment mechanism. The secondary optics must be able to adjust the angle of the mirror to face the heliostats; the cold trap haulers can place the optics to roughly face the heliostats, but some slight side-to-side adjustment will be necessary to maximize the efficiency of light transmission. The mirror must also be able to tip up and down to accommodate the angle between the heliostat and the local lunar surface. The secondary optics could be accepting light from any of the three heliostat locations, which could be at different elevations on the crater rim. The secondary optics itself might also not be perfectly level due to variations in the terrain. The adjustment mechanism will need to be powered, so the secondary optics should include a small photovoltaic array that can power the motor from sunlight coming in from the heliostats. Batteries will also be necessary since the secondary optics will need to adjust to acquire sunlight while in the dark.

4.5 Power Subsystem

Power requirements for Thermal Mining are substantial. Heating the icy regolith beneath the Capture Tent is one of the major sources of power demand. Purification, electrolysis and liquefaction drive are the other main demand. The Commercial Lunar Propellant Architecture [Kornuta et al., 2019] study determined that 800kWt is required for heating and sublimation and that 2.0MWe is needed for the remaining functions. The same study also conducted a broad survey of power options including nuclear power, reflected sunlight, and wired and wireless means of collecting and transmitting photovoltaic energy into the PSR. Though the power subsystem was not the focus of this Phase I study, it is critical for the overall architecture.

For this mission context we further develop reflected sunlight power transmission as the simplest and lightest means of delivering power to mines in reasonably sized PSRs. Highly illuminated terrain surrounding PSRs offers superlative solar capacity factors for large vertically oriented collectors [Gläser et al., 2018]. Wireless transmission is favored because laying cable is fraught with operational complexity over steep terrain between multiple landing sites, and because cable mass is high, scales linearly with distance and is hard to relocate. We desired to minimize mass and operational complexity.

The most direct way of transferring solar energy is to simply reflect it [Stoica, et al., 2016, Stoica et al., 2017]. Heliostats along the rim of the PSR focus sunlight onto the Capture Tent's secondary optics for heating and sublimation, and onto a photovoltaic array for electrical power

generation. The changing angle of incident sunlight throughout the lunar day means that single-mirror heliostats suffer periodic cosine efficiency losses. Emplacing three heliostat sites spaced by 120° along the crater rim ensures that regardless of the solar azimuth, nominal illumination can be supplied to the mine site. Having two heliostats at each rim location ensures that the capture tent and the processing plant can be simultaneously illuminated. See Section 4.8 for mass and cost estimates for this concept.

An alternative heliostat arrangement that we considered resembles a periscope, with two reflectors stacked atop each other, each angled at 45° to the horizon. The top mirror rotates to track the sun and maintains constant illumination on the bottom mirror which is aimed at the mine site. Periscope heliostats have the advantage of not requiring triplication to mitigate cosine losses, but also feature disadvantages regarding their mass and operational complexity. First, two mirrors are required instead of one, and each mirror features an elliptical profile increasing surface area by $\sqrt{2}$, meaning one periscope heliostat has a surface area 94% the size of three simple heliostats combined. Second, their angle relative to the gravity field means that substantially more support mass would be required to provide surface curvature than for the case of a nearly vertical simple heliostat. Third, construction and deployment are more complicated and reliance on a single, complex heliostat would create a prominent single point of failure.

Heliostats are limited in range due to their large beam divergence angle. The principles of geometric optics dictate that no lens can generate a lower beam divergence than the angular diameter of the source it is focusing. The sun's angular diameter of 9 milliradians at 1AU means that a perfect concentrating reflector could focus illumination on a 28m receiver no farther than 3.1km. The beam divergence of current state of the art heliostats is about 30mrad, placing a lower bound of the effective range at this scale at around 900m. With three heliostat sites along the crater rim, PSRs with areas up to $2.5\text{--}30\text{km}^2$ can be mined. Due to these limitations, we continue to evaluate other power options.

Microwave transmission from thin film phased arrays presents an attractive alternative for longer range transmission. A 60GHz system with the same 28m aperture could deliver a diffraction limited beam with a divergence of 0.2mrad, transmitting up to 150km for to a comparably sized receiver. Power could then be transmitted deep into the largest PSRs and could even be routed over the horizon by receivers on high terrain. Study is warranted on methods of transceiver construction and control, and on end-to-end electrical efficiency of such systems.

Laser transmission at 1 μm offers diffraction limited performance three orders of magnitude better than microwave for the same aperture size. Fiber lasers can be combined with vertically oriented photovoltaic arrays for long beamlines offering diffraction limited performance and very large fields of view [Enright & Carroll, 1997]. Electrical efficiencies of around 50% require higher power inputs and more heat rejection capacity than microwaves, driving system mass higher than desirable. For applications such as prospecting, with power levels up to tens of kilowatts and where range and small receiver size is more important than electrical efficiency, laser systems have desirable characteristics [Centers, et al., 2018].

Finally, nuclear power remains a viable option. Megawatt scale systems for space use are in the concept development stage by several commercial companies with estimated specific power levels of 18kg/kW [Morrison, 2020].

4.6 Deployment and Setup

One of the most risky and expensive phases of establishing a lunar propellant production capability is launch and landing on the Moon. Once hardware begins to arrive at the Moon, it will undergo setup and checkout operations to ensure it's ready for full scale production operations. This section describes a preliminary launch and landing plan based on commercially available launch and landing capability expected to be available by the time of the first launch no earlier than 2028. We are fortunate that a number of new commercial launch capabilities are currently in development by Blue Origin, Northrup Grumman, SpaceX and ULA. For the purposes of this study—to demonstrate a feasible solution—ULA's Vulcan launcher and XEUS lander are used to develop the preliminary deployment plan. A propellant production company would clearly conduct a competition among the qualified suppliers and potentially reduce risk by employing a mix of different suppliers. The aim would be to minimize cost while maintaining an acceptable risk posture.

The Vulcan/Centaur rocket is ULA's next generation launch vehicle slated to fly for the first time in 2021. It consists of a 5m diameter first stage powered by two Blue Origin BE-4 engines using LO₂/LNG propellants. The second stage is the Centaur 5, a 5m version of the venerable Centaur

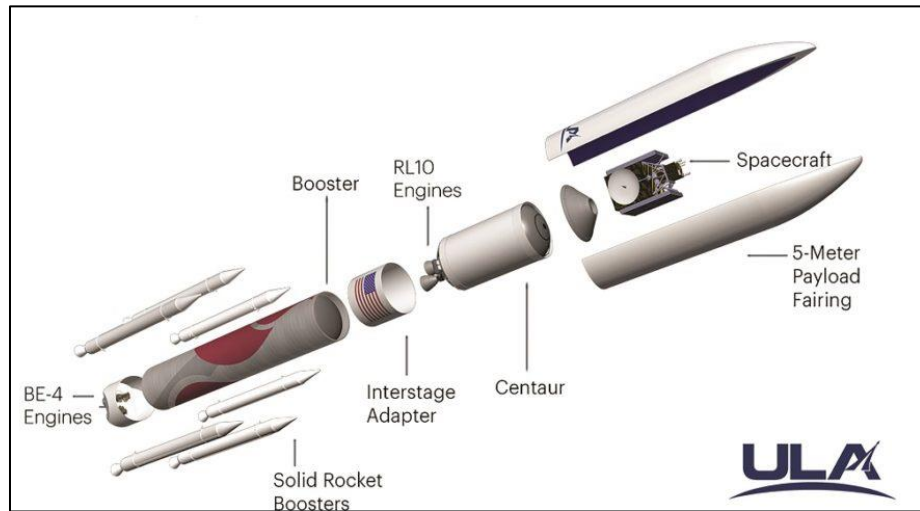


Figure 4.6.1. The Vulcan/Centaur rocket. Graphics courtesy ULA.

stage flying today on Atlas. It utilizes an upgraded version of the RL10 engine with LO₂/LH₂ propellants. It will be scarred to accept the modifications required for refueling. This upgrade will be accomplished at a future date. See Figures 4.6.1 and 4.6.2. The Vulcan can be equipped with up to six solid rocket boosters (SRBs) for enhanced performance. The upper stage can be equipped with a landing kit that allows it to descend and land on the lunar surface. The lander version of the upper stage is called XEUS, shown in Figure 4.6.3. It should be noted that the name XEUS is no longer used by ULA. They refer to the Centaur 5 lander. We retain the XEUS name for historical continuity. One significant advantage of the XEUS lander is that it lands in a horizontal orientation, allowing easy deployment of the payload on to the lunar surface.

The payload capability (performance) of the Vulcan/XEUS with 6 SRBs is 4mT to the lunar surface. Once the upper stage is equipped for refueling, a technique called distributed lift (or dual launch) can be



Figure 4.6.2. Centaur 5.

employed to significantly increase performance. This technique involves launching a tanker of fuel into a rendezvous orbit, then launching the payload to the same orbit [Schiller, 2016]. The upper stage is then refueled from the tanker and proceeds to the Moon. This technique can increase the performance to 12mT to the lunar surface, a gain of a factor of three for slightly more than the cost of two launches. See Section 4.8.4 for our assumptions on launch cost for both the single and dual launch configurations.

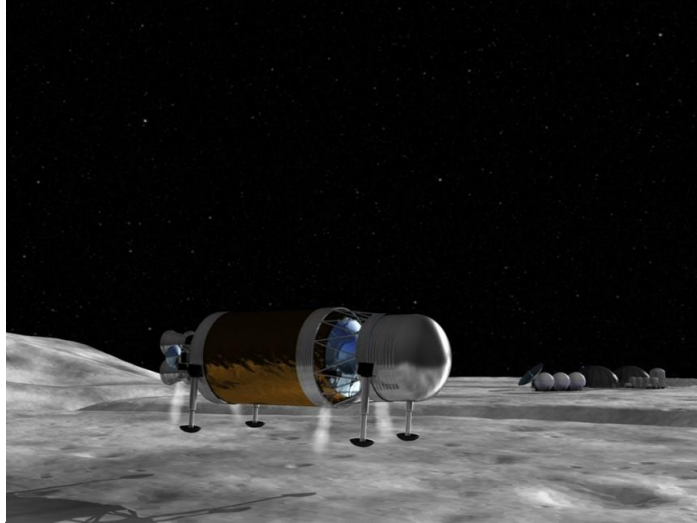


Figure 4.6.3. XEUS, the Centaur 5 stage equipped with a landing kit. Graphic courtesy ULA.

Based on these capabilities of the Vulcan/XEUS and the system hardware masses detailed in Section 4.8.1 and 4.8.2, a preliminary launch manifest and launch campaign were developed. Table 4.6.1 shows the launch sequence and the propellant production system elements included on each launch. Also included are the capability of the launch, the mass of hardware, the payload margin and the landing location. The total mass margin is 10,800 kg, over 40%, which allows for some mass growth without affecting the launch campaign or launch cost.

Table 4.6.1. Deployment launch and landing campaign details.

Launch/landing number	Launch vehicle	Capability (kg)	Payload	Payload mass (kg)	Payload margin (kg)	Landing location
1	Single	4,000	Heliostat system 1	2,500	1,500	Rim location 1
2	Dual	12,000	Liquification set 1, landing pad constructor	1,000	*11,000	PSR landing site
3	Single	4,000	Heliostat system 2	2,500	1,500	Rim location 2
4	Single	4,000	Heliostat system 3	2,500	1,500	Rim location 3
5	Dual	12,000	Liquification set 2, power plant, GPV, processing plant, comm relay	11,100	900	PSR landing site
6	Dual	12,000	Liquification set 3, capture tent, secondary optics, ice haulers, cold traps	6,600	5,400	PSR landing site
Total		48,000		26,200	10,800	

*Reserved for the landing pad constructor. Not included in total margin.

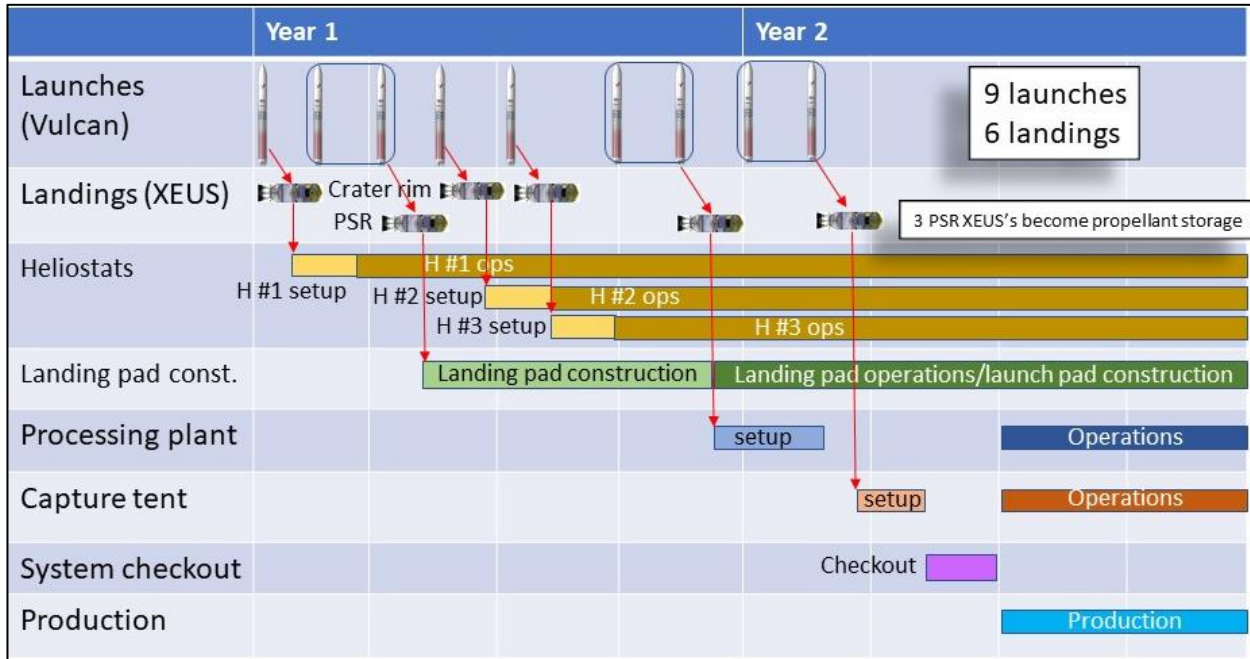


Figure 4.6.4. Deployment and setup sequence.

The launch and setup sequence is shown in Figure 4.6.4. The first mission is a single launch/landing on the crater rim of the first of three heliostat systems. The location and timing of this launch are chosen so that this system can provide sunlight to the PSR site as soon as possible. The second launch is a dual launch that lands in the PSR as close as possible to the eventual location of the landing and launch pad. The spent XEUS stage is equipped with one set of liquification hardware and is destined to become one of the storage tanks for the LO_2 and LH_2 produced by the propellant plant. The payload for this landing is a system to construct the landing pad. The design of this system is beyond the scope of this study, but various concepts have been suggested [cf. Scott, E., et al. 2019]. The construction of a landing pad before the next landing takes place is critical to minimize the dust and debris generated by a landing on exposed regolith. The landing pad construction technology is thus on the critical path for propellant production on the Moon.

The third and fourth launch/landings are for the second and third heliostat systems. Once all three heliostat systems are in place, nearly continuous power can be provided to the PSR location. The fifth launch/landing carries the bulk of the propellant processing system: the second set of liquification hardware attached to the second spent XEUS storage tank, the power system, the propellant processing system, the communications relay and the GPV. The sixth and final launch/landing carries the ice extraction system: the Capture Tent, secondary optics, and the three ice hauler/cold trap assemblies.

Each of the heliostat systems is allotted a 45-day set up phase. The heliostats are mounted to rovers that move from the landing site to the desired crater rim locations. Once in place, permanent support legs are deployed to provide a stable base for the unfurling of the heliostat reflectors. The spent XEUS stages from these landings will save enough residual fuel to eventually hop to the PSR landing pad for use as propellant transporters.

Once the landing pad construction system is landed and unloaded, it begins construction of the landing pad. This operation must be complete before landing the propellant processing plant and power station. Seven months is allocated for this operation. Once the pad is complete, the processing plant and power system can land. This landing also includes the GPV and the Communications relay. All of these elements will be deployed and set up with the aid of the GPV. It is also envisioned that the robotic element of the launch pad construction system can aid in these setup operations. These operations are expected to take 2 to 3 months. Once the ice extraction system is landed, it will be unloaded and moved to the ice field. After all system elements are in place, a full end-to-end system checkout will be performed.

To summarize, the deployment of the propellant production system can be accomplished via nine commercial launches and six commercial landings. The total duration between the first launch and the start of production is 18 months. This launch campaign is well within the capabilities of the commercial launch industry as it exists today. The necessary landing capabilities are expected to be widely available in the latter half of the decade as the CLPS and Artemis programs reach maturity.

4.7 Operations

Once the propellant production system has been deployed, set up and checked out, production operations can begin. The overall concept of operations of the propellant production plant are shown in Figure 4.7.1. After deployment from Earth, set up and checkout, ice production operations begin. Ice production can be divided into two main parts operating in parallel: ice extraction operations and propellant processing operations. In turn, the ice extraction operations can be divided into two operational phases: ice collection and transport and system repositioning.

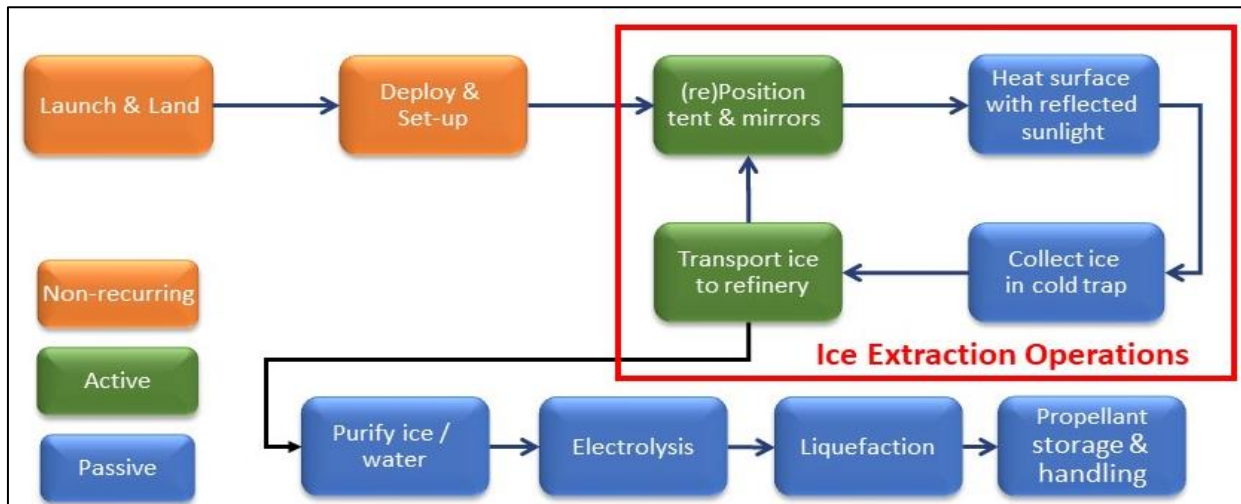


Figure 4.7.1. Overall process flow.

Ice collection and transport operations, shown in Figure 4.7.2, begin when the ice extraction system is positioned over the ice field and the heliostats and secondary optics are

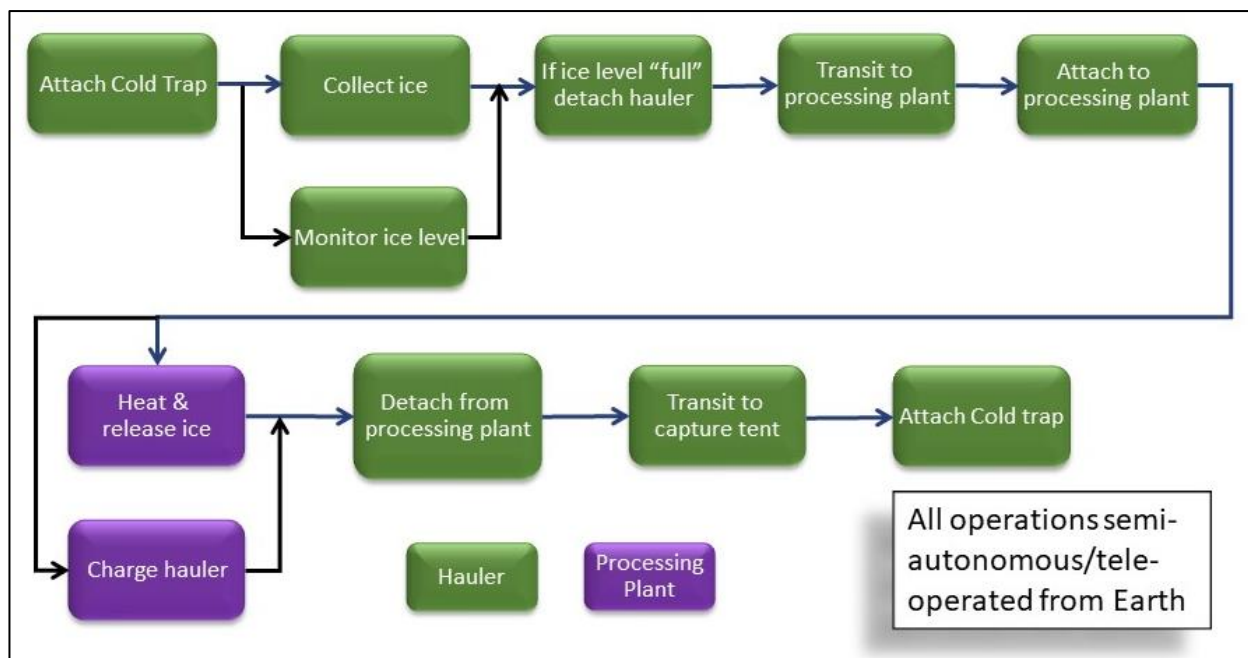


Figure 4.7.2. Ice collection and transport flow.

positioned. Two cold traps are first attached to the capture tent. Heating begins driving sublimation and ice collection in the cold traps. The fill levels in the cold traps are monitored and when a particular cold trap is full, it detaches and begins its transit to the processing facility. Once it reaches the processing plant it attaches to the unloading port where the cold trap is heated to re-sublimate the ice for input into the purification system. While unloading, the ice hauler also recharges its onboard batteries. The ice hauler then detaches from the processing plant and travels back to the capture tent.

To work out the detailed timelines and logistics of this operational phase, we developed a notional map of the propellant processing and ice mining area. This map represents a preliminary point design for sizing and feasibility determination. This will all need to be adjusted per the actual results of a resource exploration campaign. See Figure 4.7.3. During the resource exploration campaign, an ice field of the appropriate size, richness and geotechnical properties has been identified. The ice field is portioned into 10 parcels, each to be mined during one year of propellant production operations. Our point design assumes these parcels are square with sides of length, L . During the course of the year, the Capture Tent will be moved back and forth across the parcel in rows or columns. The starting location for the year is marked by a small 'o' on each parcel in Figure 4.7.3 and the ending location by an 'x.' The ending tent position for each year is adjacent to the starting position for the next year.

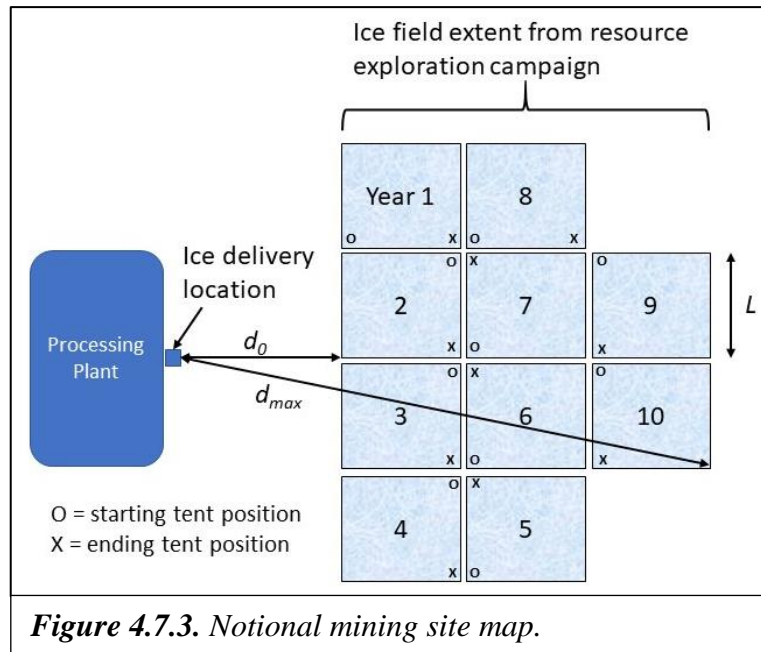


Figure 4.7.3. Notional mining site map.

The minimum distance from the ice delivery location to the edge of the ice field is denoted by d_0 . Based on the ice field geometry shown in the figure, the max distance from any point in the ice field to the ice delivery location is given by $d_{max} = \sqrt{(d_0 + 3L)^2 + (L)^2}$. If each Capture Tent placement is adjacent to the previous placement and are arranged in rows, then the length of a parcel side is given by $L = (\frac{4}{\pi})\sqrt{A}$, where A is the total annual area required to be mined. See Figure 4.7.4.

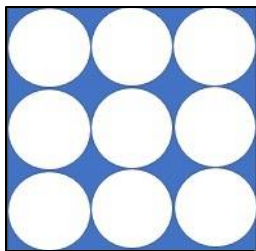


Figure 4.7.4. Tent placement pattern.

The sizing of the ice extraction system and operations is driven by the required overall propellant production

Parameter	Value
Tent diameter	30m
Tent placements	156/yr
Tent dwell time	44hr
Max cold trap dwell time	4hr
Move time	12hr
Ice mass loss	10%
d_0	100m

rate. The point solution discussed here assumes an annual propellant production rate of 1100mT. This corresponds to the commercial scenario (Scenario 1) discussed below in Section 4.9. At a propellant mixture ratio of 5.5:1, this entails the extraction of 1600mT of ice per year. To narrow in on a solution, several other assumptions are made, shown in Table 4.7.1. Based on these parameters, other parameters of our point solution can be derived. These derived parameters are shown in Table 4.7.2.

One of the most important parameters is the average rate of ice production per unit area, which is 16.1kg/m² per our current point design. Ultimately, this will become a critical requirement for both the resource exploration campaign and the ice extraction system. This is the parameter that links our proof of concept testing discussed in Section 5 and the system architecture.

The parameters in Tables 4.7.1 and 4.7.2 allow us to begin sizing the cold traps and ice haulers. Our concept includes three cold trap/ice haulers, two of which are normally attached to the Capture Tent during collection, while the other is unloading ice and recharging. The current operations concept entails a dwell time of 44h for the tent and 4h maximum for a cold trap. The round-trip time for an ice hauler to detach, transit, charge and unload, and return to the tent is 2.5h as shown in Figure 4.7.5. The average speed of the ice hauler is assumed to be 5km/h or walking speed. For comparison, the Apollo buggy was designed for a maximum speed of 13km/h.

A detailed timeline for the collection operation has been worked out including collection, transport, unloading and recharging. Over the 44 hours, each of the three ice haulers makes seven trips to the processing plant. See Figure 4.7.6. The total time attached for the haulers is 81h, giving a collection rate of 126kg/h with an average ice collected of 506kg. These data

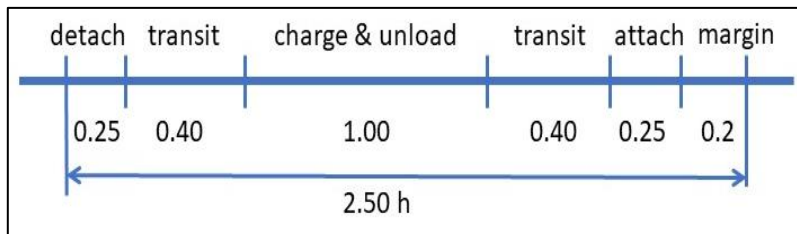


Figure 4.7.5. Ice hauler transit time.

Table 4.7.2. Point design derived requirements.

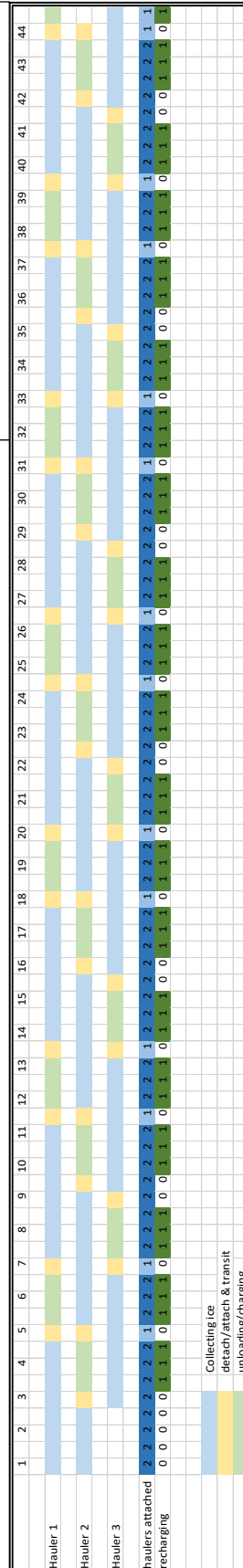
Parameter	Value
Average ice production per placement	10,256kg
Average ice production per placement per area	14.5kg/m ²
Average ice sublimation per area	16.1kg/m ²
Area mined per year	110,270m ²
L (parcel side)	423m
d _{max}	1432m

Table 4.7.3. Cold trap design parameters.

Parameter	Value
Ice capacity	600kg
Diameter	2.0m
Length	2.5m
Volume	7.85m ³
Material	Aluminum
Wall thickness	4mm

allow us to size the cold trap. Adding in a bit of margin, we have requirements for the cold trap listed in Table 4.7.3.

Figure 4.7.6. Ice hauler duty cycle. Each row represents the duty cycle for one of the three ice haulers across the 44h collection time of a tent placement. Blue is ice collection, yellow is attach/detach, and green is unload/recharge. The bottom two rows show the number of ice haulers attached at any time and the times the unloading port and charging station is occupied.



Once the ice under a particular tent location has been depleted, the tent is moved to an adjacent location. Given the placement pattern shown in Figure 4.7.4, the tent will normally be moved a distance slightly larger than the tent diameter of 30m. Doubling this and adding some margin, we assume the maximum move distance to be 70m. The time allotted for tent movement is 12h. The operations flow for tent movement is shown in Figure 4.7.7.

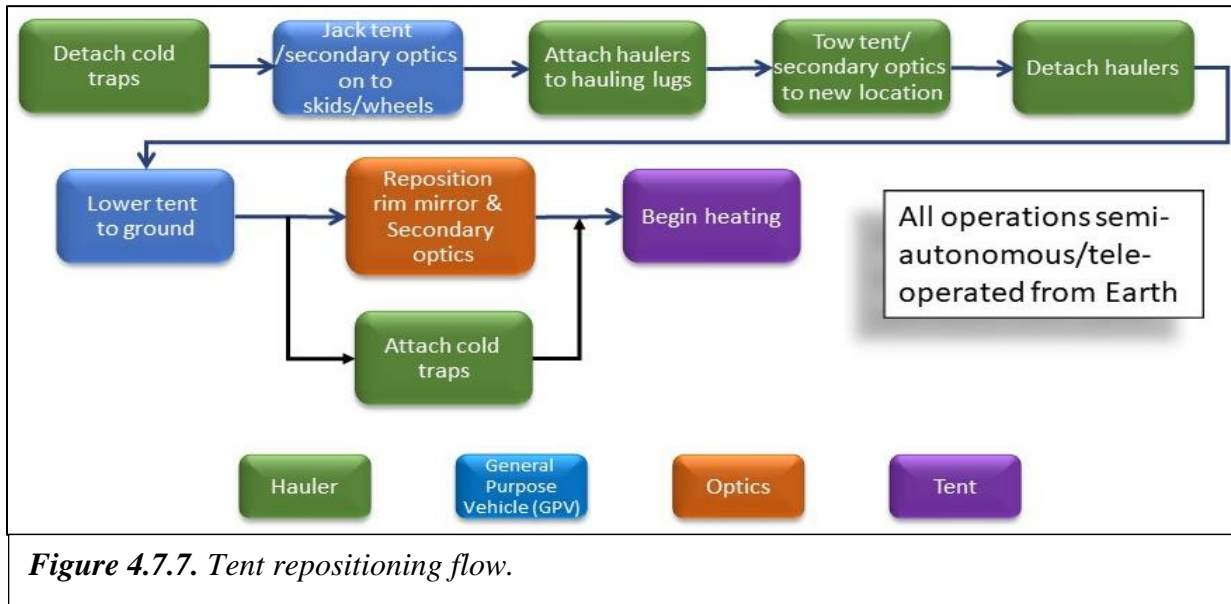


Figure 4.7.7. Tent repositioning flow.

As discussed in Section 4.4 above, four disc-shaped skids are mounted to the tent at 90 deg increments around the circumference. During collection operations, these skids are in the retracted configuration as seen in Figure 4.4.3. Each skid is extended using a screw jack mechanism operated by the GPV. Two ice haulers are then attached to towing lugs on the skids using the towing bar mounted to the back of the ice hauler. The ice haulers then slowly drag the capture tent to the new location. Any obstacles are scouted in advance by the GPV and removed or avoided during the operation. Then the skids are retracted, lowering the tent into the collection configuration. Figure 4.7.8 shows the ice hauler attached to the capture tent in towing configuration. Figure 4.7.9 is an artist’s concept of the capture tent being moved across the PSR with the secondary optics in the background.

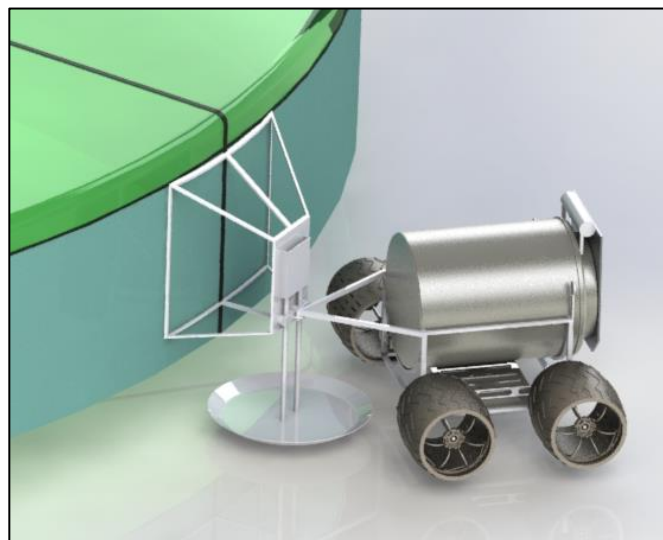


Figure 4.7.8. Capture Tent and ice hauler in the towing configuration.

Once the tent is in position, the secondary optics are towed into the new position by the ice haulers. Although the details have not yet been worked out, the secondary optics are envisioned to be

mounted to fixed skids. Finally, the rim heliostats are adjusted to point at the new location and the secondary optics are adjusted to receive the reflected light.



Figure 4.7.9. The capture tent being moved across the PSR. Art by Matt Olson.

The operations of the propellant processing plant are straightforward. Once ice delivery has commenced, the propellant processing operations are expected to be nearly continuous. They will be monitored from Earth with a limited set of possible commands or interventions. Periodic maintenance will take place and be performed by the GPV. After unloading, the vapor enters the purification system where contaminants are scrubbed out. Initially, these contaminants are disposed of, but eventually, many of them will become salable products. The purified water vapor enters the electrolysis system where it is separated into H₂ and O₂ gasses. These are liquified and stored in the XEUS derived storage tanks for sale and export into cislunar space.

Details of the purification and electrolysis system are being worked by Paragon Space Development Corporation under the NextSTEP-2 BAA. An alternate approach to the electrolysis subsystem will be developed by OxEon as part of NASA's Tipping Point program. CSM is participating in the OxEon project.

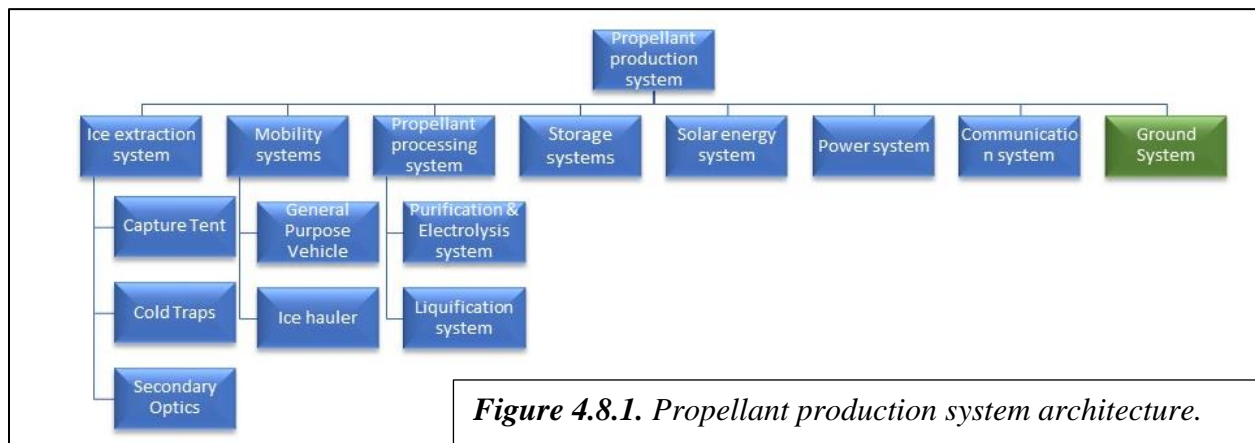
4.8 Mass and Cost Estimates

This section describes the mass and cost estimates made for the lunar propellant production system. The mass estimates were used in a number of different analyses as described above, including thermodynamic analysis, movement analysis and the deployment analysis. The mass estimates are to be regarded as a fairly aggressive point estimates for the purpose of system sizing and feasibility assessment. Actual system masses will be developed through a future detailed design process and include the appropriate margins for weight growth and other uncertainties. As stated earlier, all of the system elements have been sized to generate a production rate of 1100mT of LO₂/LH₂ propellant per year (equivalent to 1600mT of water per year). Other production rates can be conservatively obtained by simple linear scaling of the masses and costs described below.

The cost estimates were calculated based on the mass estimates and a mass to cost estimating relationship. A complexity factor was used to account for the difference in complexity among the various subsystems. Costs for system development and system fabrication were independently estimated. Where appropriate, a manufacturing learning curve was employed. Launch costs were estimated based on data previously published by ULA. Costs in dollars per kilogram (\$/kg) were converted to dollars per launch. As described in Section 4.6, the number of launches was determined from the mass estimates and the deployment and setup sequence.

4.8.1 Component Mass Estimates

Mass estimates were made for each subsystem in the propellant production system architecture shown in Figure 4.8.1. The ground system (in green) was not included in the mass estimates since it won't be launched to the Moon, but was included in the cost estimate. This section contains a short description of each element with a brief description of the mass estimation methodology. Table 4.8.5 lists all the masses as well as the location of that subsystem on the Moon: PSR or one of three crater rim locations. Figure 4.8.2 shows the masses in bar graph format.



Capture Tent

As shown above in Figure 4.4.1, the Capture Tent is a cylindrical structure with membrane-like top and walls. Its main function is to confine the vapor sublimated from the lunar surface and direct the vapor to the attached cold traps. The inner surface is reflective in the infrared

wavelengths to confine as much heat as possible. It provides four interface locations to the cold traps and has four skid structures for repositioning.

The Capture Tent is 30m in diameter and 4m tall. Thus, the total surface area is 1084m². Assuming a membrane density of 0.5kg/m², the membrane mass is 542kg. This number is rounded up to 800kg to account for uncertainties. An additional 600 kg is assumed for the support structure needed to keep the structural shape and support the mass. A mass of 100kg is assumed for each of the four skid assemblies for a total of 400kg. Finally, a mass of 200kg is assumed for other miscellaneous hardware. This brings the total mass to 2000kg. See Table 4.8.1.

Table 4.8.1. Capture Tent mass.

HW Element	Mass (kg)
Membrane	800
Support structure	600
Skid assemblies (4)	400
Miscellaneous	200
Total	2000

Cold Traps

The cold trap is a cylindrical tank whose purpose is to trap and refreeze vapor coming from the Capture Tent. There are three cold traps assumed in the architecture. Each is 2m in diameter by 2.5m long. There is a circular opening of 1.5m diameter in one end that serves as the interface to the capture tent. This opening is covered by a dust cover when the cold trap is not connected to the Capture Tent. There is also the possibility of some internal structure (e.g. veins) to aid freezing.

The cold trap is assumed to be made of aluminum of 4mm thickness. The surface area of the cylinder is 22m² and the density of aluminum is assumed to be 2800kg/m³. This gives a mass of 250kg. An additional 50kg is allotted for any internal structure. The total cold trap mass is then 300kg each, giving 900kg for all three.

Ice Haulers

The ice hauler is a vehicle permanently attached to a cold trap, one vehicle per trap, as shown in Figure 4.4.4. There are three ice haulers assumed in the architecture. The primary purpose of the ice hauler is to transport ice frozen within a cold trap to the processing plant for unloading. It has an additional function as a tow truck to move the capture tent and secondary optics to a new location. The vehicle is assumed to be wheeled with 4 large metallic wheels and is equipped with a towing hitch and headlights.

The mass of the ice hauler is assumed to be 500kg, consisting of the wheels, drive train, chassis, batteries, heaters and other miscellaneous equipment. Including the cold trap itself, the total mass of the vehicle is 800kg unloaded. For reference, the Spirit and Opportunity Mars rovers were 185kg each while the Curiosity rover is 900kg. The combined mass of all three haulers is 1500kg.

Secondary Optics

The purpose of secondary optics is to receive light from heliostats located in areas of persistent sunlight and redirect it to the lunar surface. It consists of a large elliptical mirror held above the Capture Tent by some support structure. The mirror can be pointed to track the location of the heliostats as the ice extraction system is moved.

The mirror is assumed to be a thin film material held in position by lightweight support structure. There is also a support base that nestles up against the capture tent. The elliptical mirror is 40m by 30m giving an area of 950m². Assuming a density of 0.5kg/m³, the mirror mass is 471kg, rounded up to 500kg. The mass of the support structure is assumed to be 600kg and the control hardware 100kg.

Table 4.8.2. Secondary optics mass.

HW Element	Mass (kg)
Elliptical mirror	500
Support structure	600
Power & controls	100
Total	1200

General Purpose Vehicle

The general-purpose vehicle (GPV) is a rover to perform operations and maintenance tasks requiring manipulation and rudimentary dexterity. There is one GPV assumed in the architecture. GPV tasks include initial assembly operations, removing and replacing line replaceable units (LRUs)—hardware components designed to be replaceable as part of the long-term maintenance plan—raising and lowering the capture tent for movement operations, and scouting the tent move route for hazards. The vehicle is equipped with a number of manipulator arms and other devices for maximum long-term flexibility.

The GPV’s wheels, drive train, chassis, batteries, heaters, and other basic components are assumed to be identical to the ice haulers and have a mass of 500kg. The manipulator hardware, sensors and other hardware are assumed to have a mass of 500kg. The mass of the GPV is thus 1000kg.

Purification and Electrolysis System

The purification and electrolysis system takes raw ice from the ice haulers and converts it into hydrogen and oxygen. See Figure 4.2.5. As discussed in Section 4.0, there are indications that other volatiles besides water ice are frozen in the lunar PSRs. Although these substances might have economic value in the future, for the purposes of producing LO₂/LH₂ propellants, they are contaminants. The purification subsystem removes these contaminants and feeds pure water into the electrolysis system. In turn, the electrolysis system converts the water into hydrogen and oxygen gas.

Industrial scale systems for both water purification and electrolysis are commercially available today. Unfortunately, these systems tend to be extremely heavy, not having a need to reduce mass for terrestrial use. An estimate for the lunar system was made by looking at several commercially available systems, scaling to the required production rate of 1100mT/yr, subtracting components deemed unnecessary for lunar use, and assuming the remaining components can be made lighter by a factor of two. This resulted in a mass of 4000kg for the electrolysis system and 1000mT for the purification system. This gives a total mass of 5000kg.

This crude estimate will be refined based on the results of ongoing technology development programs by Paragon and OxEon to develop space capable systems.

Liquification System

Once water is electrolyzed into hydrogen and oxygen gas, it must be liquified for storage and use as propellants. This step will be aided by the cold temperatures in the lunar PSRs, but to date, it has not been studied in detail. The overall concept is to incorporate this hardware into the three XEUS landers that will deploy the system elements into the PSR. As a placeholder until more

detailed analysis can be performed, this hardware is assumed to have a mass of 1000kg per XEUS lander. The total mass is thus 3000kg.

Propellant Storage System

The propellants will be stored in the tanks of the three XUES landers that deployed the system elements into the PSR. Each spent XEUS stage can hold 70mT of propellant: 59.2mT of LO₂ and 10.8mT of LH₂. Since these stages have been purchased for the deployment campaign, their mass does not count against the system mass and their cost is included in the launch costs.

Solar Energy System (Heliostats)

The solar energy system is a critical component of the propellant production system. It provides all the energy needed for the operation in the PSR. It consists of three identical sets of two heliostats, deployed in three locations around the rim of the PSR to provide nearly continuous sunlight for operations. Each set consists of a large heliostat and a small heliostat. The large heliostat illuminates the photovoltaics of the power system to provide energy to the purification, electrolysis and liquification systems. The small heliostat illuminates the secondary optics subsystem to provide energy for ice extraction. Each set is deployed by one XEUS landing. Each heliostat is mounted to the top of a small rover that will be used only once to move the system from the landing location to the proper location at the PSR rim. Once in position, permanent support legs will be deployed and the heliostat unfurled.

Heliostat construction is assumed to be based on thin film mirror technology and aggressive masses were assumed. These were based, in part, on the NIAC work of Stoica [Stoica et al., 2016; Stoica et al., 2017]. The area of the large heliostat is 5000m² giving a diameter of 80m, while the small heliostat has an area of 600m² with diameter of 28m. Assuming a density of 0.1kg/m², the masses are 500kg and 60kg respectively. The mirror support structure is assumed to be half of the mirror mass giving 250 kg and 30kg.

Table 4.8.3. Heliostat mass.

HW element	Small heliostat mass (kg)	Large heliostat mass (kg)
Mirror	60	500
Mirror support	30	250
Mobility & base support	400	400
Power & controls	100	100
Margin	210	450
Total	800	1700

The mobility and base support structure are assumed to be 400kg for each to allow commonality. The mass of the other systems, power, control, pointing and communications is assumed to be 100kg each. Finally, a mass margin of 450kg and 210kg is included for the large and small heliostats, respectively. See Table 4.8.3.

The total mass of the small heliostat is thus 800kg. The large heliostat is 1700kg. The combined mass of the set is 2500kg. The grand total for all three sets is 7500kg.

Power System

The primary purpose of the power system is to receive sunlight from the large heliostat and convert it into electrical power for use in purification, electrolysis and liquification. It consists of

a 30m diameter photovoltaic (PV) array, batteries and heaters, structure, a charging station for the haulers and GPV, cabling and control system.

The mass density of the PV array is assumed to be 2.8kg/m² and its area is 707m², giving a mass of 1980kg. The mass of the support structure is assumed to be 400kg. Batteries and heaters are estimated to have a mass of 1000kg, the charging station is 100kg, cabling is 100kg and the pointing and controls are 140kg. A mass margin of 380kg is included for a total to 4000kg.

Communication System

The communication system is a simple data relay to enable communications with Earth. The main relay may be collocated with one of the heliostats or it may be located in the PSR. It relays command signals from Earth to the heliostats, the secondary optics, the power station, the propellant processing plant and the vehicles. It relays health and monitoring data from the systems to Earth and enables the teleoperating of the GPV and ice haulers. The communications system is greatly simplified if a global satellite communication system exists for the Moon. The mass of the relay is assumed to be 100kg.

Table 4.8.4. Power system mass.

HW Element	Mass (kg)
PV array	1980
Support structure	400
Batteries & heaters	1000
Cabling	100
Charging station	100
Pointing & controls	140
Margin	380
Total	4000

4.8.2 Total Mass

Table 4.8.5 shows the mass of each component estimated above, the location of that component and the total mass. Figure 4.8.2 shows a comparison of subsystem masses in bar graph format.

Table 4.8.5. Subsystem masses by lunar location and total mass.

Subsystem	Mass (kg)	Lunar location
Capture tent	2000	PSR ice field
Cold traps	900	PSR ice field & processing plant
Ice haulers	1500	PSR ice field & processing plant
Secondary optics	1200	PSR ice field
General purpose vehicle	1000	PSR ice field & processing plant
Purification & electrolysis system	5000	PSR processing plant
Liquification system	3000	PSR processing plant
Solar energy system	7500	PSR rim, 3 locations
Power system	4000	PSR processing plant
Communication system	100	PSR processing plant
Total	26,200	

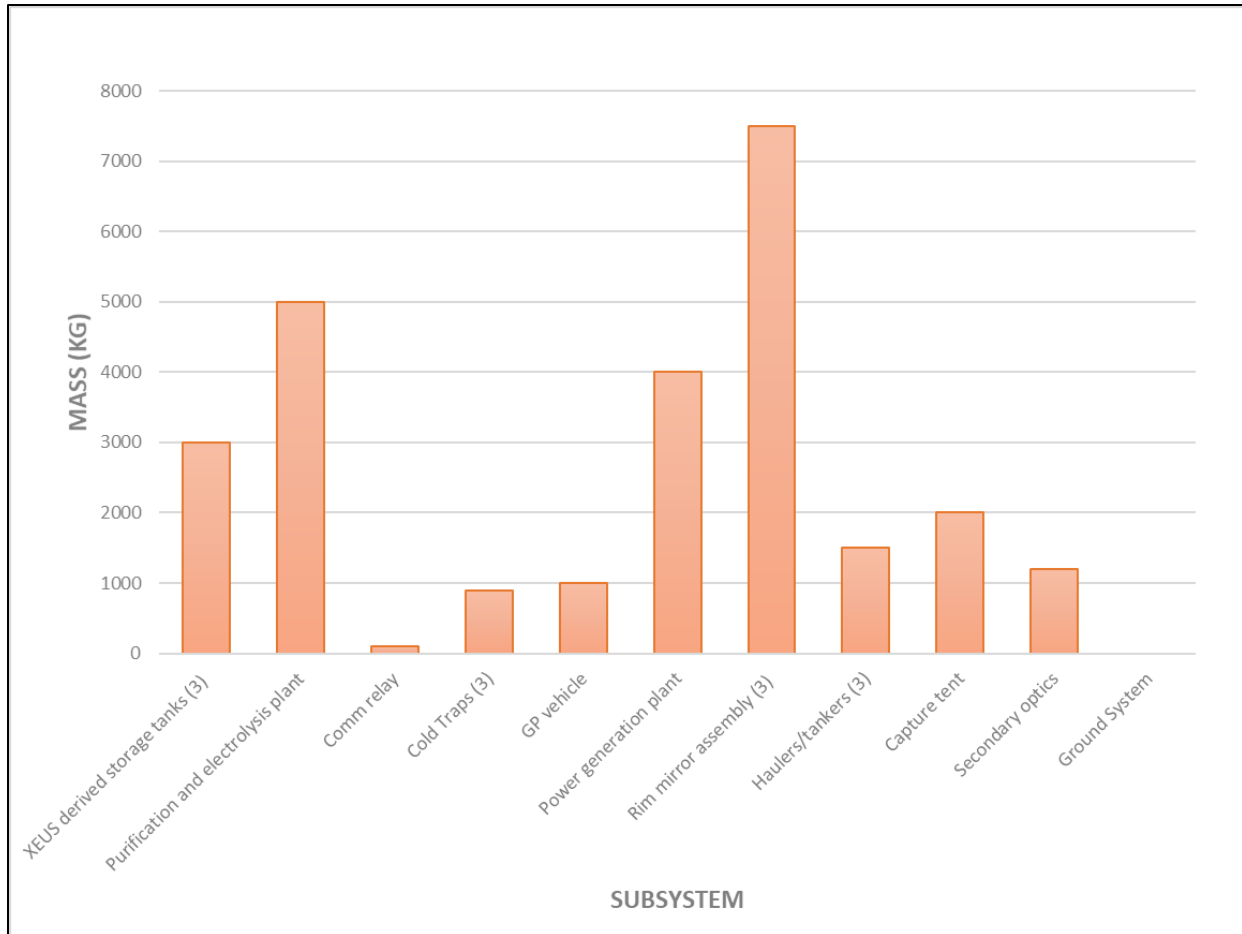


Figure 4.8.2. Subsystem mass comparison.

4.8.3 Subsystem Cost Estimates

The cost estimates for each subsystem hinge on the mass estimates determined above. In general, both the development cost and the production cost are determined by multiplying the mass by a factor in dollars per kilogram (\$/kg). These factors vary from subsystem to subsystem depending on the complexity and estimated difficulty in developing and/or producing the subsystem.

Costs are separately estimated for the development of the subsystem and the production of the system. Development cost includes all activities required to develop the system up through qualification testing. This includes technology research and development (R&D), prototype testing, design evaluation testing, detailed design, integration and qualification testing. It also includes development of the production and supply system. Production cost is the cost to manufacture the subsystem in the quantities required by the architecture.

Development costs are estimated by a single \$/kg factor for that subsystem. The value of the factor is intended to represent a commercial, for profit, development approach. In this approach, all the cost and cost risk is borne by the system developer, tending to keep costs low and timelines short. This is in distinction to a typical government run development program where the

cost and risk are born by the government and contractors are reimbursed on a cost-plus basis. A government development approach would entail much higher costs.

The nominal cost factor used was \$50,000/kg. This value corresponds to aerospace industry experience for hardware of average complexity. In contrast, the government development of a highly complex system like the Curiosity Mars Rover was a factor of 10 higher. At the other end of the spectrum, terrestrial mining equipment is two to three orders of magnitude lower, reflecting both high mass and mature technology. This average value was adjusted up or down based on our judgement of the relative complexity of the particular subsystem.

The production costs for the subsystems were estimated in a similar manner with a base \$/kg factor. However, some of the subsystems are produced in quantity, or have similarities. For example, the wheels, chassis, drive train and power system are assumed to be the same for the GPV and the ice haulers. Hence, that component needs to be developed only once, but with a total of four produced (one GPV and three ice haulers). When subsystems or components are produced in quantities larger than one, a learning curve is applied. The learning curve exponent used was 0.9, a typical value in the aerospace industry.

Table 4.8.6 shows the unit mass, development cost factor and development cost estimate for each subsystem, while Table 4.8.7 shows the production cost factors, first unit cost, number of units, and total build cost. The ground system has been added in both tables as a discrete element of cost. The total development cost is \$883M while the production cost is \$613M. Figure 4.8.3 shows a comparison of both development and production costs for the subsystems.

Table 4.8.6. *Subsystem development cost estimates.*

Subsystem	Unit Mass (kg)	Cost factor (\$/kg)	Development cost (\$k)
Capture tent	2000	50,000	100,000
Cold traps	300	20,000	6,000
Ice haulers	500	0 (incl w/GPV)	0
Secondary optics	1200	50,000	60,000
General purpose vehicle	1000	100,000	100,000
Purification & electrolysis system	5000	50,000	250,000
Liquification system	1000	50,000	50,000
Solar energy system	2500	70,000	175,000
Power system	4000	30,000	120,000
Communication system	100	20,000	2,000
Ground system	—	—	20,000
Total	17,600		883,000

Table 4.8.7. Subsystem production cost estimates.

Subsystem	Unit Mass (kg)	Cost factor (\$/kg)	Units	First unit cost (\$k)	Production cost (\$k)
Capture tent	2000	20,000	1	40,000	40,000
Cold traps	300	10,000	3	3,000	8,239
Ice haulers	500	30,000	4	15,000	53,343
Secondary optics	1200	20,000	1	24,000	24,000
General purpose vehicle w/o base	500	30,000	1	15,000	15,000
Purification & electrolysis system	5000	20,000	1	100,000	100,000
Liquification system	1000	20,000	3	20,000	54,924
Solar energy system	2500	30,000	3	75,000	205,965
Power system	4000	20,000	1	80,000	80,000
Communication system	100	20,000	1	2,000	2,000
Ground System	—	—	1	30,000	30,000
Total	17,600				613,471

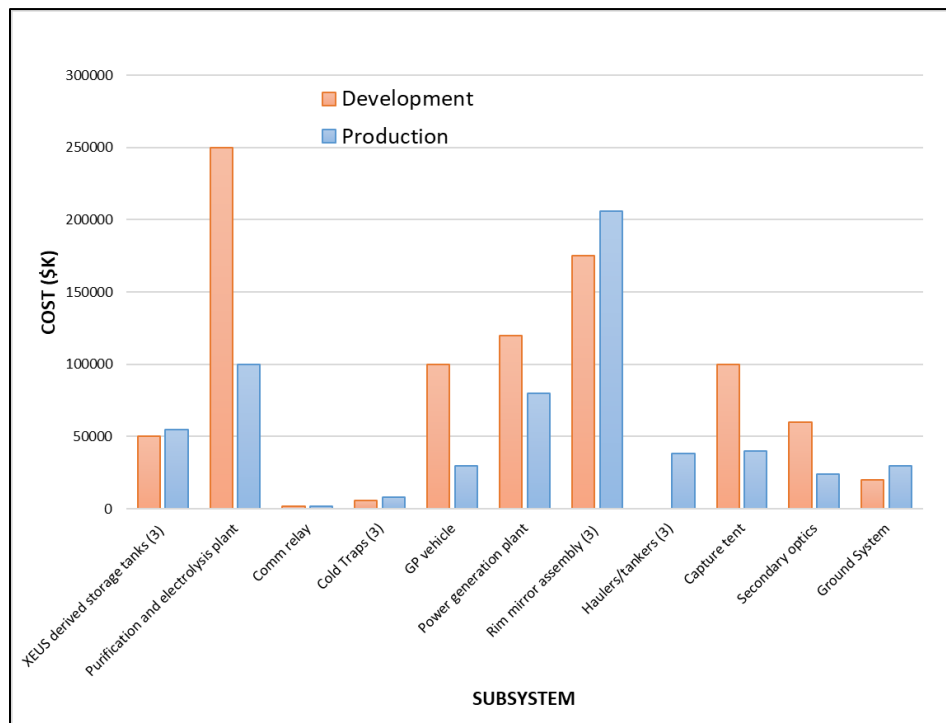


Figure 4.8.3. Development and production cost by subsystem.

4.8.4 Total Cost

Launch and Landing Cost

The previous section developed estimates for the development and production costs of the propellant production system. The last component of non-recurring cost to be considered is launch cost. The numbers used here are based on publicly available data published by ULA [Sowers, 2016]. The data are based on the launch of the currently in development Vulcan launcher with the upper stage equipped with a lunar landing kit, called XEUS. The landed capabilities of XEUS are 4000kg and 12,000kg for single and dual launch respectively. The dual launch scenario is discussed in Section 4.6. The cost factor for a single XEUS launch to the lunar surface is \$35,000/kg. This gives a launch cost of \$140M. A 10% premium was added for a dual launch to account for the cost of refueling hardware and operations in route to the Moon. Hence the price of a dual launch is \$308M. These data are summarized in Table 4.8.8.

Launch configuration	Mass delivered (kg)	Cost (\$M)
Single	4,000	140
Dual	12,000	308

As discussed in Section 4.6, six landings are required to deploy the propellant production system. Three single launches are used to deploy the three sets of heliostat systems on the PSR rim. Three dual launches are required to land the propellant production and ice extraction systems into the PSR. However, the first PSR landing is used to deploy a landing and launch pad construction system, not assumed to be part of or chargeable to the mining operation. Presumably, this cost would be borne by the transportation company, a critical element of the overall propellant ecosphere, but independent of the mining company. This landing does include one of the three liquification systems with a mass of 1000kg. Since the capability of the dual XEUS launch is 12,000kg, one twelfth of the cost of that launch is included here. Table 4.8.9 shows the cost of each launch and the total launch cost.

Launch number	Cost (\$M)
1 (single)	140
2 (single)	140
3 (single)	140
4 (dual)	26
5 (dual)	308
6 (dual)	308
Total	1062

Non-recurring Cost (Capital Expenditures or CapEx)

We can now combine everything into one grand total cost for development, production and deployment as shown in Table 4.8.10. This represents the capital expenditures for the project or CapEx.

Table 4.8.10. Propellant production system non-recurring cost.

Cost Element	Cost (\$M)
Development	883
Production	614
Launch	1,062
Total	2,559

Recurring (Operations) Cost

The final component of cost is the recurring cost. This cost represents all of the effort required to operate the mining operation to generate the required propellant production rate. Elements of this cost include the labor to operate the ground system to receive data from the lunar system, process the data, determine necessary actions and provide the necessary operational commands. These activities can be classified as routine operations, scheduled maintenance operations and repair operations. Routine operations include tele-operating ice haulers and the GPV as they move ice, recharge and relocate the ice extraction system, repointing the heliostats and secondary optics, operating the propellant processing system and monitoring system health. Scheduled maintenance will include replacing rapidly wearing parts, cleaning systems, and detailed inspections. Repair operations occur when the system breaks.

A detailed analysis of all of these operations will occur in the next phase of the study. At this point, we will use a cost factor as we did for the non-recurring costs. The operations cost factor is assumed to be \$3000/kg per year. This factor is applied to the entire mass of the system. as shown in Table 4.8.11.

Table 4.8.11. Propellant production system non-recurring cost.

System mass (kg)	Cost Factor (\$/kg)	Annual Operations Cost (\$k)
26,200	3000	78,600

4.9 Business Case Analysis

One of the overarching goals of this NIAC project is to enable the development of lunar water resources into a commercially viable enterprise. To achieve this, the lunar propellant production operation must generate economic value, measured by profit. In principle, making a profit is quite easy. It is the simple condition that revenues exceed costs. But in practice, this condition can be difficult to achieve. This section describes our analysis of the revenues and costs incurred by a hypothetical company implementing a Thermal Mining based propellant production system on the Moon. This company will be referred to as “the Production Company” or “the Company” for short.

This section will first examine the revenue side of the profit equation. Revenue comes from customers agreeing to purchase propellant at a particular location for a particular price. In the mind of the customer, the value of the propellant at that location must exceed the price paid. Section 4.9.1 will look at markets for propellant in space, potential customers and rationale for prices at different locations in space. The costs, both non-recurring and recurring, were discussed in detail in the last section. The third element is the timeline for expenditures and revenues. Because of the cost of money and the time value of money, cash now is more valuable than cash in the future. These considerations will be addressed via a set of business case scenarios discussed in Section 4.9.2. Section 4.9.3 will look at several figures of merit that capture the relative profitability of the Company as well as the potential benefits accruing to NASA or other government entities. Finally, Section 4.9.4 will provide a comparison of this analysis to other recent analyses of the cost of lunar propellant.

4.9.1 The Propellant Market

The Physics and Economics of Refueling

The cost of most space activities is dominated by transportation cost. The energy to escape Earth’s gravity well is enormous and the distances between interesting or valuable destinations in space is vast. For the sixty years since the first human mission into space, all space missions have originated on Earth with all propellants brought from Earth. This situation gives rise to what is known as the tyranny of the rocket equation. The rocket equation is taught to every science or engineering freshman and is simply written: $\Delta V = v_e \ln (m_i/m_f)$, where ΔV is the velocity added to the rocket, v_e is the exit velocity of the rocket engine, m_i is the initial mass of the rocket including propellant and m_f is the final mass after all propellant has been expended. The difference between the initial mass and the final mass is essentially the mass of the propellant.

If you solve the rocket equation for propellant mass in terms of ΔV , the equation is exponential. In other words, the farther you want to go in space (increasing ΔV), the required propellant increases at an ever-increasing rate. This can be understood intuitively by considering your own car. Suppose you wanted to drive from Washington DC to Los Angeles but all the gasoline for the trip had to be brought with you from Washington. Even if you rented a trailer for the gasoline, your car probably wouldn’t be able to haul it. You’d need a truck. But the truck gets far worse gas mileage, so you’d need a bigger trailer, but now you need a bigger truck. Translating that situation to rockets is the reason rockets leaving Earth consist mostly of fuel, and that a rocket

going to the Moon and back, must be the size of a Saturn V used in Apollo or the SLS currently in development.

However, if you can refuel enroute, and reuse the propulsion system through multiple refuelings, you can *break the tyranny of the rocket equation*. The exponential increase of propellant with ΔV becomes linear. Figure 4.9.1. shows the the enormous benefit of one, two or three refuelings in reducing required propellant for a given ΔV . Furthermore, reduced requirements for propellant to do a given mission entails

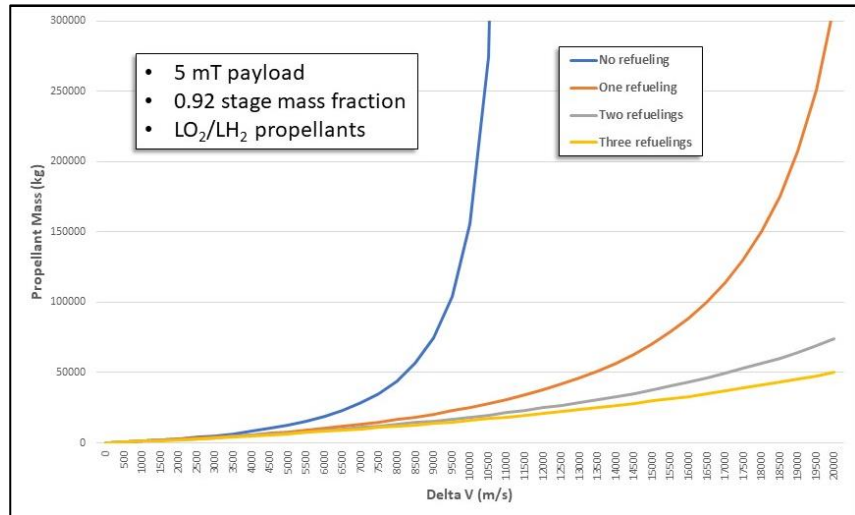


Figure 4.9.1. Benefits of refueling with space sourced LO₂/LH₂ propellants.

a reduction in the size of the rocket or the number of rockets required. Either of these situations results in a significant reduction in the cost of the mission. See Table 4.9.1.

Given that the Moon is a viable source of water (Section 4.1) and thus LO₂/LH₂ propellant, it is uniquely situated to enable space activities in cislunar space and beyond. The Moon is the closest source of resources (mostly) outside Earth’s gravity well. Escaping the Moon’s gravity well is far easier than Earth’s. As shown in Figure 4.9.2, the ΔV from the surface of the Moon to EML1 is a factor of five less than from Earth and it doesn’t have an atmosphere to fly through.

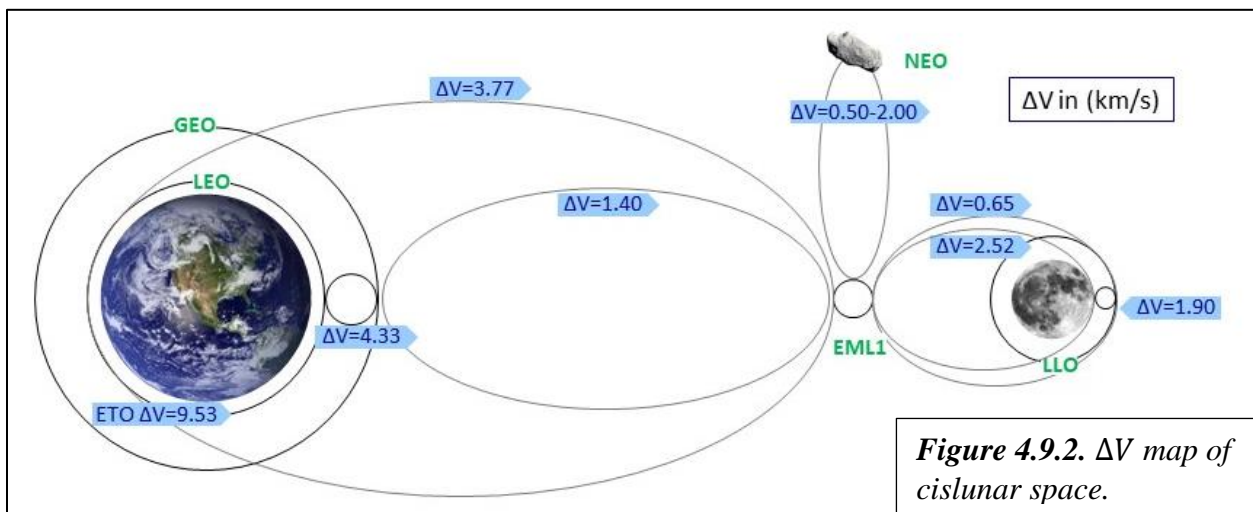


Figure 4.9.2. ΔV map of cislunar space.

Of course, a source of fuel is not valuable unless there is a refuelable space transportation architecture able to take advantage of it. Fortunately, there are several commercial companies working on refuelable upper stages and landers including Blue Origin and ULA. As Chief Scientist of ULA, PI Sowers made a public offer to buy propellant in space to support ULA’s future upper stage, being designed to be refuelable. He presented prices ULA would be willing to pay at various

locations within cislunar space. These prices, depicted in Figure 4.9.3, reflect both the physics discussed above and the corresponding economics of propellant in cislunar space. The blue bars represent the cost of propellant (or any mass) launched from Earth. The green bars were set by the criterion that the price of lunar propellant in LEO be less than the price of propellant launched from Earth at the same location. The LEO price chosen was \$3000/kg, lower than the \$4000/kg to launch from Earth. If this condition is met, then ULA would be able to lower the cost to launch a payload from Earth to GSO, a critical piece of ULA’s current market.

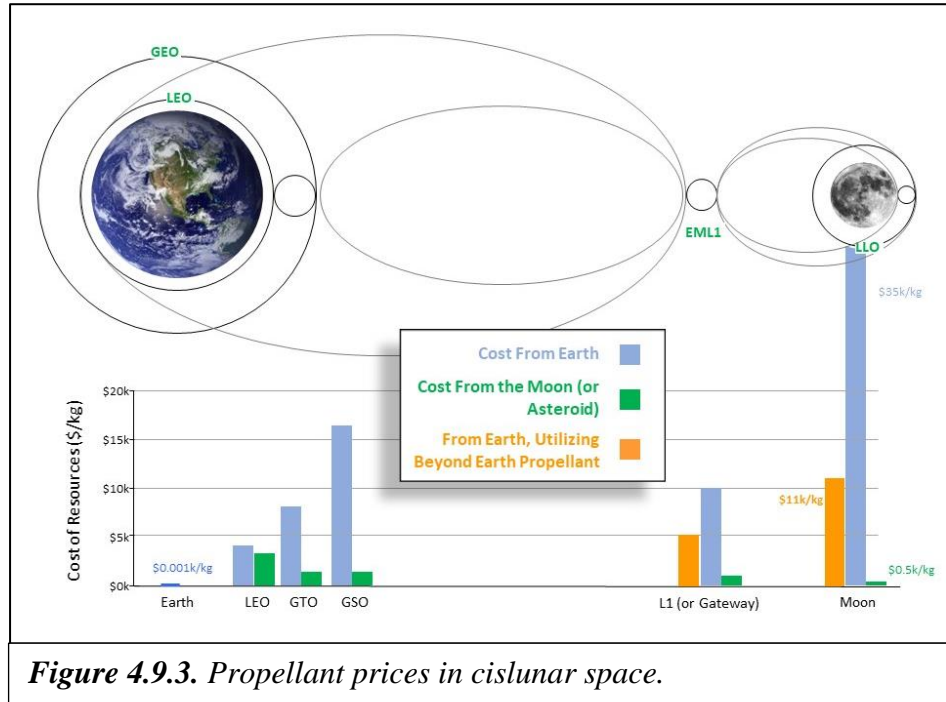


Figure 4.9.3. Propellant prices in cislunar space.

The price of propellant on the lunar surface required to ensure meeting \$3000/kg in LEO is \$500/kg. This depends on several assumptions regarding transporting the propellant from the Moon to LEO. First, the transportation utilizes ULA’s ACES upper stage and XEUS lunar lander. Second, all maneuvers are propulsive. This assumption is very conservative, given that aerobraking using Earth’s atmosphere to decelerate to LEO could reduce the cost by a factor of two. The other key location for pricing is EML1. This location is a good proxy for any location in high Earth or Lunar orbit such as the orbit of NASA’s proposed Lunar Gateway station. From the Earth, this price is \$10,000/kg. From the Moon, the price is \$1000/kg, a factor of ten reduction. In the business case analysis below, the latter price has been increased to \$1100/kg to provide better profitability for the transportation company.

Finally, the orange bars represent the price to move mass from Earth to EML1 or the lunar surface, *if you refuel enroute a single time using propellant from the Moon*. The use of lunar propellant will reduce the cost to move mass to the gateway by a factor of two and reduce the cost to move mass to the lunar surface by a factor of three. These two facts alone should convince policy makers to move forward with lunar propellant production as a top priority. Table 4.9.1 summarizes the cost benefits of using lunar propellants. To summarize, every space mission beyond LEO will benefit from the use of refueling with lunar propellant.

Table 4.9.1. Benefits of lunar-sourced propellants.

Space Activity	Lunar-Sourced Propellant Benefit
Transportation from Earth to Geosynchronous orbit.	10-20% lower cost.
Transportation from Earth to the lunar gateway.	2 times lower cost.
Transportation from Earth to lunar surface.	3 times lower cost.
Transportation from the lunar surface to the lunar gateway and back.	70 times lower cost.
Cost of a human mission to Mars.	2-3 times reduction.
In-space transportation.	Essentially the cost of lunar-sourced propellant.

Propellant Markets

Given that all space missions beyond LEO benefit from refueling with lunar propellant, determining markets becomes a matter of understanding what those missions are and who are the customers. This is an easy matter for today’s missions and markets and ULA’s initial pricing was firmly grounded in this reality. Looking ahead, there are two categories of future market growth: future programs planned assuming current non-refueling economics and future missions enabled by the profound cost reduction entailed by refueling. Below, we take each category in turn.

The current and forecasted launch markets are compiled by the FAA Office of Commercial Space (AST). Missions that could benefit from refueling go to GSO or beyond [FAA, 2018]. The GSO satellite location has been the anchor for the launch market for many decades. That market has been remarkably steady with 15-20 launches per year worldwide. The FAA forecast for the next decade is for that market to remain steady at the 15-20 launches per year level. The other class of current missions that would benefit from refueling are NASA interplanetary science missions. Historically, these have occurred roughly twice per year. Hence, the total current market for refueling is in the range of 17-22 missions per year. The original ULA business model assumed three of these missions, refueled in LEO as the initial, foundational commercial demand for propellant.

Beyond current markets, many government space agencies, non-governmental entities and commercial companies are planning for exploration, business and other activities beyond LEO. All of these activities require transportation and refueling with space-sourced propellant will dramatically lower the cost of that transportation. Recently, the focus of most of this energy has been the Moon and cislunar space. The current US space policy entails a “return of humans to the Moon for long-term exploration and utilization” [SPD-1, 2017]. The European Space Agency (ESA) is also focused on the Moon as is China. As the elements of the architectures that support these goals begin to be defined, refueling with lunar propellant can play a large role in lowering cost or expanding capability or both.

For example, NASA’s current plans envision a Lunar Gateway in high lunar orbit. The Gateway is a space station, occupied periodically by humans, that serves as a way station for

missions to the lunar surface. Early plans envision four commercial missions per year to the Gateway for logistics. The same mass could be delivered in two missions by refueling with lunar propellant. Even more dramatically, the cost of missions to and from the lunar surface could be reduced by factors of up to fifty using lunar propellant. To fully take advantage of this potential, it is imperative that the transportation architecture be developed with refueling in mind.

Finally, there are many space missions and activities that are probably not feasible or affordable without the use of refueling with space-sourced propellants. The list of these potential space missions is limited only by imagination, but two stand out. It has long been a goal of humankind to visit, then colonize another planet. Mars is the closest and most amenable target and it is a stated policy goal of the US to eventually land humans on Mars. There have been many proposed architectures for human missions to Mars, but most of them entail aggregating large masses of hardware and propellant in cislunar space. One recent estimate [McVay, et al., 2016] shows that 163mT of hardware consisting of a habitats and landers as well as 103mT of propellant are required in cislunar space for a Mars mission spanning 26 months. Both hardware delivery and propellant are markets for lunar propellant.

Finally, space solar power (SSP) offers the promise of inexhaustible energy for Earth forever. The barrier to establishing SSP has been the large size and mass of SSP satellites making the cost unaffordable if launched from Earth. However, using lunar resources to construct the satellites and lunar propellant to deliver the satellites to GSO reduces the cost to the point where SSP can be competitive with terrestrial energy sources.

Adjacent Markets

Although the first viable market for lunar volatiles is likely to be LO₂/LH₂ propellant, water has many uses in space. The architecture described in Section 4.2 produces purified water in the steps before electrolysis. Water can be diverted at this stage to satisfy other markets. Water can be used as propellant directly for low thrust applications like steam propulsion systems for Earth orbiting satellites. It can be used in higher thrust applications as propellant for plasma thrusters. Once we have human presence at the Gateway or on the lunar surface, water will be needed for life support and even agriculture. Water can be used as radiation shielding for the Gateway or Mars missions. Split into hydrogen and oxygen, water can be used for energy storage. *Water will be the foundation of the space economy.*

In addition to water, the propellant production architecture will also produce an excess of oxygen. This is because the propellant is produced in the mass ratio 5.5:1 oxygen to hydrogen and water comes in the mass ratio of 8:1. This means that for each metric ton of propellant produced, 450kg of excess oxygen is produced. This oxygen can be sold as oxidizer to customers using a fuel other than hydrogen or used for breathing air or some other chemical process.

Finally, there are a number of other volatiles present at the lunar poles that must be removed from the extracted ice by the purification system as shown in Table 4.0.1. Many of these substances have potential exploration or economic value.

4.9.2 Business Case Scenarios

This section will describe three business case scenarios for the Propellant Production Company. Scenario 1 represents commercial demand only and all investment coming from the

private sector. Scenario 2 represents a Public Private Partnership (PPP) modeled after NASA's successful Commercial Orbital Transportation Services (COTS), Commercial Resupply Services (CRS) programs. The demand model is commercial plus missions to the Gateway plus a minimal surface demand for refueling two landers per year. Scenario 3 is the same as Scenario 2 but with the addition of demand for an ongoing Mars program, both hardware delivery and propellant.

The following ground rules are common to all three scenarios:

- This is the very first mining operation to be established on the Moon.
- The cost of the resource exploration (or prospecting) campaign is borne by NASA and/or other international governments. Resource exploration is an important activity to map the locations and abundances of ice as well as characterize the chemical and geotechnical properties of the materials. This assumption is justified by the high risk of this activity, the tremendous scientific value of the data obtained and the potential economic and strategic value of the resource. A framework for the resource exploration campaign was developed at a workshop held at CSM in the summer of 2018 [Sowers, et al., 2018]. A roadmap for this campaign is shown in Figure 4.0.2.
- Some upfront technology development is funded by NASA or other governments. This is already happening via a number of programs within NASA's Space Technology Mission Directorate (STMD). This NIAC study is an example.
- Full scale development and production of the ice mining facility occurs over a four-year time span.
- Deployment, setup and checkout of the propellant production plant takes 18 months, as shown in Section 4.6.
- The operational life of the plant is 10 years.
- There is a separate transportation company that takes delivery of the propellant at the production plant and moves it to the point of customer delivery. Transportation costs are reflected in Figure 4.9.3 prices.

The demand models and pricing models for the three scenarios are shown in Table 4.9.2. Baseline pricing is as shown in Figure 4.9.3. The sensitivity of business results to pricing will be shown in the following section. The difference in demand at the point of sale and the lunar surface represents the cost and propellant expended moving the propellant from the lunar surface to the point of sale (POS). The commercial, Gateway and lander demand is assumed to be constant for the 10-year production life of the operation. The Mars demand begins in the third year of operations and continues through end of life.

Table 4.9.2. Propellant demand and price.

Scenario	Market segment (POS)	Demand at POS (mT)	Price at POS (\$/kg)	Demand at lunar surface (mT)	Price on lunar surface (\$/kg)
1	Commercial (LEO)	210	3000	1100	500
2	Commercial (LEO)	140	3000	733	500
	Gateway (~GTO)	140	1700	420	500
	Landers (lunar surface)	5	500	5	500
3	Commercial (LEO)	140	3000	733	500
	Gateway (~GTO)	140	1700	420	500
	Landers (lunar surface)	5	500	5	500
	Mars Propellant (EML2)	47	1100	94	500
	Mars Hardware (~GTO)	210	1700	630	500

The total propellant demand on the lunar surface determines the required propellant production rate for the system. The total propellant demands for the three scenarios are 1100mT, 1158mT and 1882mT, respectively.

The public private partnership (PPP) model for Scenarios 2 and 3 is based on the COTS/CRS model with elements drawn from the Commercial Crew development program (CCDev). The program consists of four phases, each retiring risk, maintaining competition and affording off ramps. The first two phases are modeled after CCDev; the third phase after COTS and the fourth phase after CRS. The phases of program are as follows:

- Propellant Mining Development 1 (PMDev 1). The purpose of this phase is to retire the risk on the critical technologies enabling ice mining and propellant production on the Moon. There would be notionally 4 to 6 winners receiving \$5-10M each over a two-year period of performance (POP). A cost match would be required.
- Propellant Mining Development 2 (PMDev 2). The purpose of this phase is to further retire the risk on the critical technologies enabling ice mining and propellant production on the Moon. Lunar surface demonstrations would be included using the Commercial Lunar Payload Services (CLPS) program. There would be notionally 3 to 4 winners receiving \$20-30M each over a three-year POP. A cost match would be required.
- Full Scale Development and Deployment (FSDD). This phase develops, builds and deploys the full-scale production plant. There would be one to two winners each receiving \$400-800M (Scenario 2) or \$800-1200M (Scenario 3) over a five-year POP. The contract would be milestone based with NASA’s investment fixed.

- Production. This phase is the production and delivery of propellant. NASA would commit to a pre-negotiated annual buy of propellant. The contractors would be incentivized by business forces (recovering their investment) to seek other customers.

A roadmap for this program is shown in Figure 4.9.4. It is integrated with the resource exploration campaign [Sowers & Morris, 2018] and leads to full propellant production within 10 years.

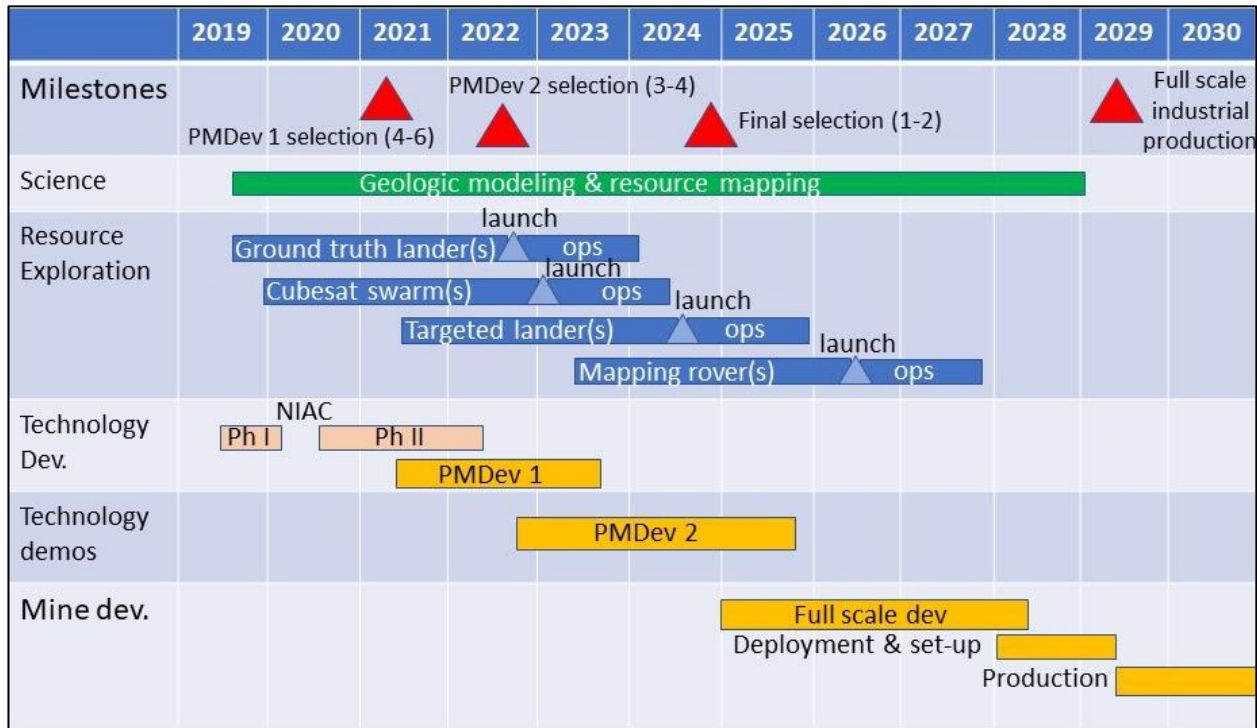


Figure 4.9.4. Propellant production program plan (Scenarios 2 and 3).

The cost model for each scenario is based on the costs developed in Section 4.8, scaled by the relative production rates for the three scenarios. The scale factor for Scenario 1 is 1.0; Scenario 2 is 1.052; and Scenario 3 is 1.625. These factors are applied to the development, production and operations costs. The launch costs for both Scenario 1 and 2 are the same since the launch campaign developed for Scenario 1 had sufficient mass margin to accommodate Scenario 2. Scenario 3 added one dual launch at \$308M.

4.9.3 Business Case Results

The critical data for the three scenarios are summarized in Table 4.9.3. The key figure of merit is Internal Rate of Return (IRR). This measures the annual rate of return of the investments into the Company provided by the revenues. It's a function of the time dependent streams of cash, either into the company in the form of revenues or out of the Company in terms of costs. The acceptability of a particular IRR is determined by other business factors influencing the Company. These include the debt to equity ratio, risk rating, tax rate, interest rates and inflation. The minimum acceptable IRR is often referred to as the hurdle rate. If the IRR exceeds the hurdle rate, it will generate a positive Net Present Value (NPV) and is an indicator that the business is viable. If the IRR is less than the hurdle rate, the business is not viable.

Table 4.9.3. Key business case parameters.

Parameter	Scenario 1 (Commercial Only)	Scenario 3 (Commercial + NASA Lunar)	Scenario 4 (Commercial + NASA Lunar + Mars)
Production rate (mT/yr)	1100	1158	1882
Development cost (\$M)	883.0	929.6	1435.1
Production cost (\$M)	613.5	645.8	997.0
Transportation cost (\$M)	1062.0	1062	1370
Operations cost (\$M/yr)	78.6	82.7	127.7
NASA investment (\$M)	0	800	1200
Price (\$/kg)	500	500	500
Revenue (\$M/yr)	550	579	971
IRR (%)	8.84	15.8	15.4

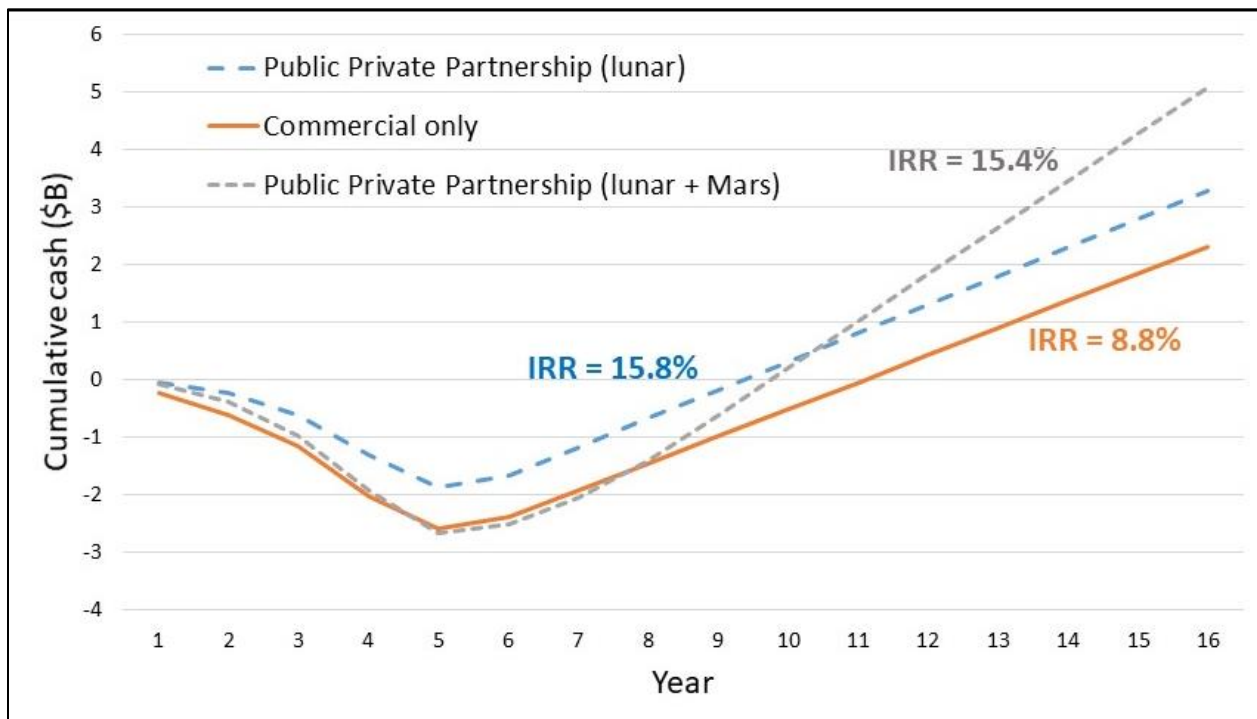


Figure 4.9.5. Cumulative cash for the Propellant Production Company.

Figure 4.9.5 shows the cumulative cash versus time for the three scenarios. Cumulative cash can be thought of as the money in the company’s bank account. In each scenario, the curve dips below zero as funds are expended to develop, produce and deploy the propellant production. Once the system is operational and production begins, revenues are generated and the curve begins to head upward. The break-even point (cumulative cash of 0) is not reached until year 9 or 10 for the PPP scenarios, and not until year 11 for the commercial only scenario. But by the end of the mine life, all scenarios are in the black, netting between \$2B and \$5B.

Acceptable IRR values for something as new and risky as lunar mining are difficult to predict with what we know today. Sommariva et al. (2019, 2020) discuss a range of 8% to 20% while Charania and DePasquale (2007) use a value of 21.7%. The value of 8.8% for Scenario 1 is clearly marginal without other business enhancing measures (e.g., government guarantees or tax incentives), but both PPP scenarios are more promising. Options to increase business viability include increasing propellant price or the level of NASA investment. Figures 4.9.6, 4.9.7 and 4.9.8 show sensitivities of the IRR to increased propellant price for each of the three scenarios. Also included is the sensitivity with development cost for Scenario 1. A cost factor was applied to the all the components of non-recurring cost discussed in Section 4.8. A hurdle rate of 21.7% can be readily met by a price increase or additional NASA investment or both. As shown in Figure 4.9.3, lunar propellant prices have a lot of margin relative to launching from Earth in every market except LEO. But the price at LEO can be reduced by a factor of two by simply using aerobraking instead of a propulsive maneuver to move from a HEO orbit into LEO.

So far, we have discussed the business scenarios from the perspective of the Company. However, a good PPP should provide benefits to both the public sector and the private sector. Since the government is a not for profit entity, it is not appropriate to talk in terms of revenues. Instead, we calculate NASA benefits in terms of savings; in other words, savings resulting from the availability of propellant and the costs described take the place of revenues.

NASA savings in Scenario 2 accrue from the reduced cost of propellant purchased on the lunar surface and from the reduced cost of cargo missions to the Gateway. The cost of the propellant purchased on the lunar surface is \$2.5M/yr (5mT/yr @ \$500/kg). If brought from Earth, this propellant would cost \$175M (5mT/yr @ 35,000/kg). The savings is thus \$172.5M/yr. As discussed above, the number of cargo missions could be reduced from four to two using lunar

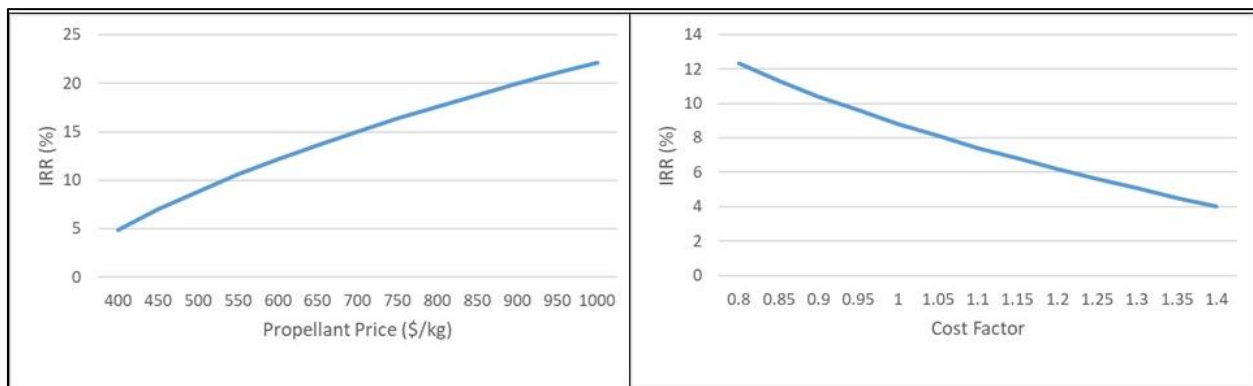


Figure 4.9.6. Scenario 1. IRR sensitivity with propellant price and non-recurring cost.

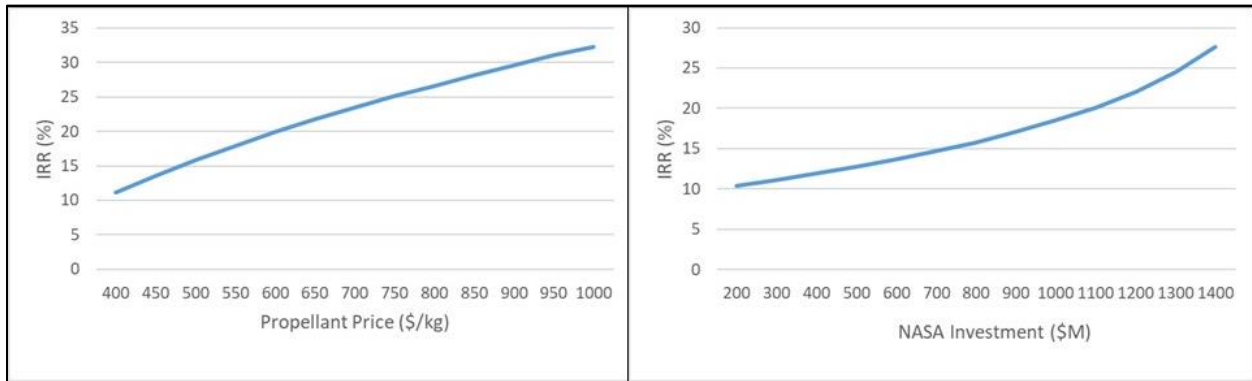


Figure 4.9.7. Scenario 2. IRR sensitivity with propellant price and NASA investment.

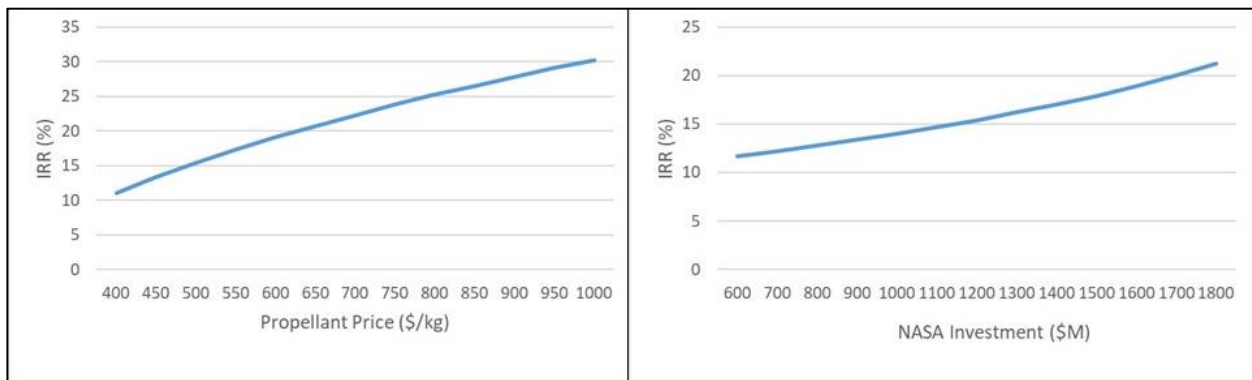


Figure 4.9.8. Scenario 3. IRR sensitivity with propellant price and NASA investment.

propellant. Assuming each mission costs \$150M, the savings is \$300M/yr. The total savings is \$472.5M/yr.

The savings for Scenario 3 are even more spectacular. In addition to the \$472.5M/yr savings in Scenario 2, enormous savings are realized for a Mars mission. A Mars mission requires delivering both hardware and propellant to an aggregation point in cislunar space. Derived from McVay et al. (2016), the annual mass of hardware for a Mars campaign is 75mT and propellant is 47mT. The cost to deliver hardware mass to cislunar space using lunar propellant is \$375M (75mT @ \$5,000/kg). The cost to deliver lunar propellant to cislunar space is \$52M (47mT @ \$1,100/kg). The cost to deliver all this mass to cislunar space from Earth using the SLS can be determined using data from Jones et al, (2019) who give a number of \$46,000/kg. Delivered from Earth using SLS, the cost is \$5,612M/yr. The annual savings for a Mars campaign is thus \$5,185M/yr.

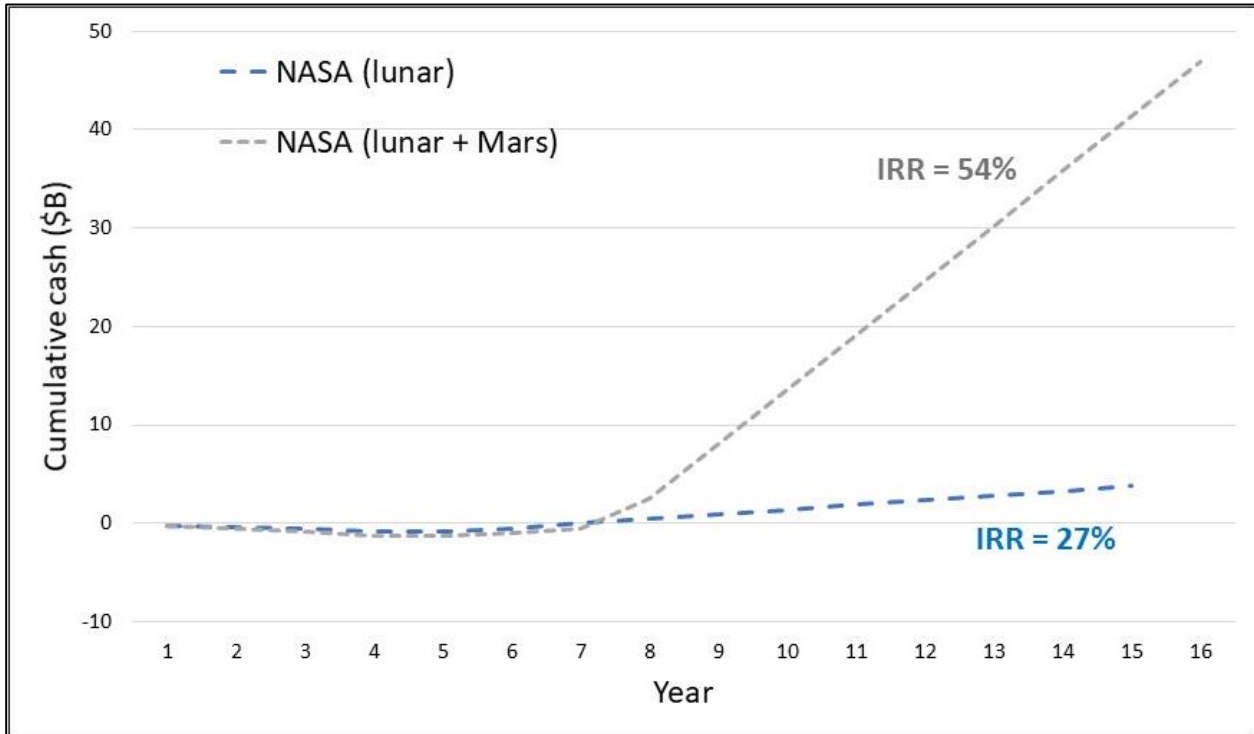


Figure 4.9.9. Cumulative cash for NASA.

Figure 4.9.9 shows the cumulative cash flows for NASA as a function of time with savings expressed as positive cash. The IRR for Scenario 2 is a respectable 27% while the IRR for scenario 3 is double at 54%. The net savings for Scenario 2 is over \$4B while the savings for Scenario 3 is a whopping \$47B. Clearly, the use of lunar propellant is enormously beneficial and probably enabling for any Mars program.

4.9.4 Comparison to Previous Analysis

The previous section has shown that a propellant price of \$500/kg on the lunar surface or \$1100/kg in cislunar space can support an economically viable business. A propellant price at this level also generates enormous cost savings for NASA for both Moon and Mars exploration. However, a number of previous studies have resulted in much higher prices. Shisko (2019) has put together a good comparison of the most recent relevant papers. For example, Charania & DePasquale (2007) derive a cost of \$26,845/kg at the lunar surface. Shisko (2019) escalated that price to 2019 dollars producing \$35,300/kg. This is about a factor of 70 greater than the price used here. A more recent paper by Jones et al. (2019) gives a value of \$101,000 in cislunar space for the scenario most similar to ours, a factor of 90 higher. This section gives a brief summary of the major differences between our approach and other recent literature, focusing on Charania & DePasquale (2007) and Jones et al. (2019).

It is worth restating here that the Thermal Mining architecture developed under this NIAC study is intended to be the minimal economically viable architecture. Every effort has been made to keep the architecture simple and the costs as low as possible. Making use of recent scientific

findings (e.g., Li et al., 2018) indicating surface ice in abundances up to 30wt%, our ice extraction system is 65% less mass than excavation. Furthermore, we have made full use of the commercial strides in space transportation in the past few years. This has allowed us not to burden the Company with the cost of developing a completely new transportation system. Finally, we have assumed a PPP model that leverages both public and private sources of capital.

The 2007 study by Charania and DePasquale assumed a completely private venture. Their company was also responsible for transportation and thus had to develop two new in-space vehicles, a lunar tanker vehicle (LTV) and an orbital transfer vehicle (OTV). The propellant production plant relied on excavation and had a mass of 20.9mT producing 49.4mT of propellant per year yielding a plant efficiency of 2.3 (kg of annual propellant production per kg of plant mass). This is in contrast to the efficiency of 42.0 for the Thermal Mining system. Their plant was deployed to the Moon using NASA’s heavy cargo launcher, a precursor to the current SLS. Finally, as discussed above, they assumed a hurdle rate of 21.7%. Table 4.9.4 provides a summary of the key differences.

The hurdle rate discrepancy is easiest to reconcile using the data in Figure 4.9.6. A price increase to \$1000/kg increases the IRR to 22%. That still leaves a factor of 35 difference. The plant efficiency difference is a factor of 18 leaving another factor of 2, easily accounted for by the other factors. Clearly, the high efficiency of Thermal Mining is the critical element in achieving low prices.

Table 4.9.4. Thermal Mining comparison with Charania and DePasquale (2007).

Factor	Charania & DePasquale	Thermal Mining	Comments/Rationale
Propellant price on lunar surface	\$35,300/kg	\$500/kg	Factor of 70 difference.
Transportation system development	Included	Not included	Transportation system elements in development by commercial companies (Blue Origin, SpaceX, ULA) & NASA.
Delivery to the Moon	NASA heavy cargo vehicle	Commercial	Commercial launch readily available, commercial landing in development.
Plant efficiency	2.3	42.0	Thermal Mining avoids excavation, targets surface ice.
Business model	Commercial	PPP	NASA investment improves IRR, reduces risk.
Hurdle rate	21.7%	9-15%	Thermal Mining commercial scenario achieves 22% IRR with price of \$1000/kg.

The recent study by Jones et al. (2019), henceforth abbreviated as “Jones” was conducted to specifically answer the question of whether lunar propellant would be more cost effective than bringing propellant from Earth for a Mars mission. The analysis was conducted from the perspective of a completely government run Mars program with no lunar activity other than propellant production for the Mars mission. Jones examined a number of scenarios, but his scenario 3 is most similar to the Thermal Mining architecture: “Propellant delivered from the

Moon using a reusable lunar lander between the Moon and cis-lunar aggregation. All-up deployment of ISRU infrastructure.”

A number of significant differences exist between the assumptions of Jones and the Thermal Mining architecture. First is the assumption of the business model. Jones’ model was a full up government program with commensurate cost assumptions. No insight was provided into the details of the cost model. The comparison point for propellant cost was cislunar space. Thus, an assumption must be made on the means of transportation from the lunar surface to cislunar space. Jones assumed a reusable lunar lander with mass fraction of 0.26 (inert mass to total mass). This number came from NASA studies for the Altair lander, to be used for human landings in the previous lunar program. Our study assumed a mass fraction of 0.11 for the XEUS. The XEUS mass fraction is credibly derived from the ACES mass fraction of 0.08. An early version of ACES is slated to fly next year. This difference amounts to a factor of five in the resulting cost.

Next, Jones assumed SLS and presumably the same lander, would deliver the propellant plant to the Moon. No costs for this are provided though SLS costs for delivery to cislunar space are quoted to be \$46,000/kg. This is a factor of 4.6 higher than the commercial price shown in Figure 4.9.3. The propellant mine itself has an efficiency of 8.4 compared to 62.0 for Thermal Mining. It is important to note that Jones accounted for the mass of the power system separately, which is why this efficiency is different than cited above for the Charania study. In a private correspondence with Jones (Jones, 2019), just this factor was enough to reduce the price in their model to \$23,000/kg, a factor of 4.4.

Finally, Jones assumed a nuclear power source for the propellant plant and power levels based on molten regolith electrolysis. Nuclear power is a viable source for powering a propellant plant in a lunar PSR and remains an option for Thermal Mining. However, the specific power used by Jones is high based on the current state of the art. Jones used a value of 75kg/kW versus a value of 18kg/kW shown by Ultra Safe Nuclear Corporation (USNC) in a recent seminar at CSM (Morrison, 2020). Reflected sunlight using thin film mirrors is even more efficient at 5.8kg/kW. The power demands used by Jones are derived from work on molten regolith electrolysis, a technique being developed to extract oxygen from lunar regolith. It is a very poor proxy for the energy requirements of ice mining. For one, melting regolith requires temperatures in the range of 2200K versus sublimating ice at 220k.

The cost effect of the two parameters we can quantify is enough to resolve most of the discrepancy, leaving a factor of four. This residual can be easily explained by the other factors like power, and non-recurring cost including delivery from Earth.

Table 4.9.5. Thermal Mining comparison with Jones et al., (2019).

Factor	Jones et al.	Thermal Mining	Comments/Rationale
Propellant price in cislunar space	\$101,000/kg	\$1100/kg	Factor of 92 difference.
Business model	Government only	PPP	Commercial investment amortized over the 10-year life of the operation.
Delivery vehicle mass fraction	0.26	0.11	Mass fraction corresponding to the Altair human lander. XEUS based on cargo only Centaur derivative.
Delivery to the Moon	SLS	Commercial	Commercial launch readily available, commercial landing in development.
Plant efficiency	8.4	62.0	Thermal Mining avoids excavation, targets surface ice. Jones based on molten regolith electrolysis.
Power source	Nuclear (75kg/kW)	Reflected sunlight (5.8kg/kW)	Reflected sunlight very mass efficient. Nuclear number high by factor of 4.
Power efficiency	Based on molten regolith electrolysis (48kW/T/yr)	1.8kW/T/yr	Molten regolith electrolysis is a poor proxy for ice extraction, producing only oxygen and requiring temperatures of 2200K (vs 220K for Thermal Mining).

This quick comparison to previous studies highlights the advantages of the Thermal Mining approach and the philosophy of a minimum viable architecture. The efficiency of Thermal Mining far exceeds any method based on excavation. This high efficiency is gained by targeting surface ice, using reflected sunlight and avoiding excavation. The use of commercial methods, a highly efficient commercial transportation system, and a PPP business model also result in much lower costs. Of course, much work remains to retire the risks inherent in Thermal Mining on the Moon. But the promise is astounding: tens of billions of dollars in savings for the Moon to Mars program and opening up the Moon and cislunar space to economic development, delivering trillions of dollars into Earth’s economy.

5.0 Proof of Concept Testing

The overarching objective for the proof of concept testing was to demonstrate the sublimation of water ice from icy regolith simulant samples via surface and subsurface heating. A secondary objective was to gain an understanding of the physics of the heating and sublimation process to enable the development of effective extractive techniques. Both the primary and secondary objectives were met.

5.1 Test Objectives and Approach

Using thermal energy to mine volatiles at an industrial scale is a novel approach to collecting ice on the moon. Our objectives started with defining the overall yield (g/cm^2) using the power of the sun (simulated with a laboratory lamp), and the ice ore production rate (g/s). As testing proceeded, objectives were added to include a broader understanding of how thermal energy penetrates icy regolith, sublimation of ice at cryogenic temperatures, and determining how ice migrates in the subsurface. The objectives were chosen to gain an understanding of the thermal mining phenomena and to increase ice yields.

1. Determine the overall yield of ice (g/cm^2).
2. Determine the ice sublimation rate (g/s).
3. Develop a simple model to describe heat transfer into icy regolith.
4. Develop a simple model to describe sublimating ice in regolith.
5. Determine how ice migrates in cryogenic icy regolith.

To achieve these objectives, the Block 1 apparatus was built to simulate a functional thermal mining system. A lamp was used to simulate the power output of the sun. The PSR environment was simulated in the lab environment at cryogenic temperatures ($<100\text{ K}$) by using liquid nitrogen and the vacuum chamber consistently reached vacuum pressures of ($\sim 10^{-4}$ Torr). The icy regolith simulant was produced in the lab and is described in Section 5.2.

The lamp used (Plusrite 3223 75W12V MR16) is a 75-Watt halogen bulb. Using an optical output sensor, the lamp output was measured and adjusted to simulate insolation at 1AU, $1371\text{W}/\text{m}^2$. The lamp output was adjusted to maximize the bulb output over the entire top surface of the simulant, while not touching the cryogenic boundary. A halogen lamp was chosen due to its better spectral match to the sun.

5.2 Icy Regolith Simulants

The physical structure of cryogenic volatiles and regolith in the Permanently Shadowed Regions (PSRs) of the Moon are not well defined. In this study, the regolith compactness, density, and thermal properties are assumed to be analogous to the lunar highlands, while the volatile species in this study are limited to water. Cryogenic ice in this study was produced in various configurations described below. We produced multiple icy regolith simulant configurations and captured a broad data set under various icy regolith conditions.

The regolith simulant used was LHS-1, a highlands simulant produced by the University of Central Florida's Exolith Lab. The chemical makeup and specific grain size distribution closely matches samples taken during Apollo 16 as shown in Figure 5.2.1. Before production of each icy regolith simulant batch, LHS-1 was placed in an oven at 275F for 300 minutes to remove any trace amounts of

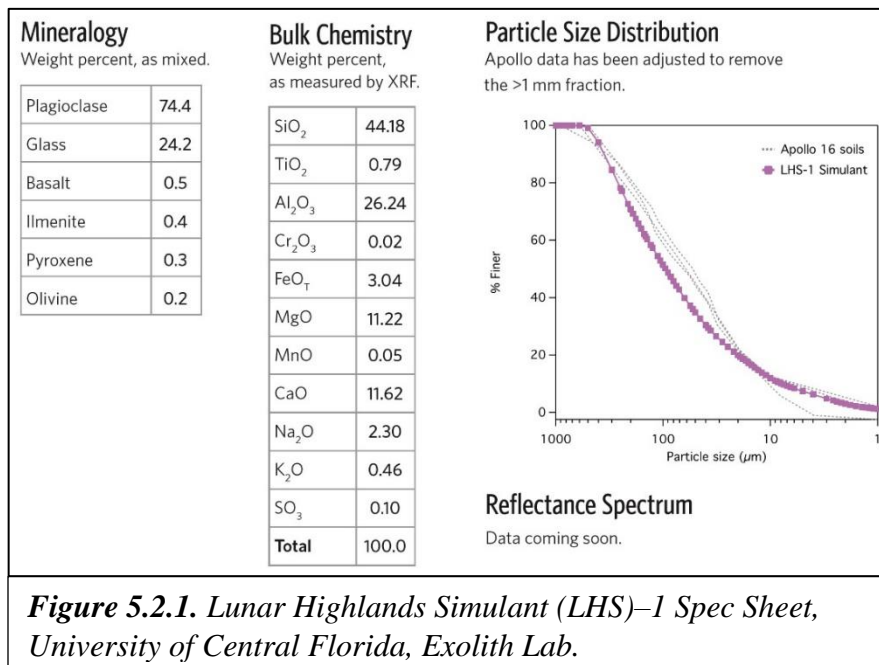


Figure 5.2.1. Lunar Highlands Simulant (LHS)-1 Spec Sheet, University of Central Florida, Exolith Lab.

moisture. The dried LHS-1 was then placed in a sealed container in a freezer or stored at room temperature, depending on the icy regolith configuration to be produced.

Granular Icy Regolith Simulant

Granular icy regolith simulant is a new icy regolith simulant developed for this work that is based on the theory that icy regolith in PSRs is granular, loose and has a low cohesive value, analogous to dry sand. Blocks of ice in a freezer are shaved to small grain sizes and then sifted to yield ice grains of various sizes. The grain size configurations are described in Table 5.2.1. A dry batch of LHS-1 is cooled to 254K. Measured amounts of chilled dry regolith are combined with measured amounts of granular ice and thoroughly mixed inside of a freezer at 254K. This method produces an icy regolith simulant that is physically analogous to sand where some grains are ice and some regolith as seen in Figure 5.2.2.

Table 5.2.1. Granular Ice Grain Distributions.

Ice Configuration	Grain Size	Notes
Fine	< 0.84mm	-
Medium	0.84mm < x < 1.2mm	-
Coarse	> 1.2mm	-
Multi-Grain	Fine (80.1%) Med (14.7%) Coarse (5.2%)	Grain distribution chosen to be similar to LHS-1

A metal sample container is filled with the icy regolith mixture and then placed in a bath of liquid nitrogen. The simulant-filled container is then further cooled to 80K as shown in Figure 5.2.3. At cryogenic temperatures, the simulant maintains the mechanical behavior of sand. There is no observed increase in soil cohesion after 20 hours of cryogenic cooling. The density of granular icy regolith simulants is consistent with the water weight percentage, but the simulants were not mechanically compacted in this study. Simulant density is shown as a function of water weight percentage in Table 5.2.2.



Figure 5.2.2. Granular Icy Regolith Simulant, 12% Water Weight.

Table 5.2.2. Granular simulant water weight % vs density.

Water Weight %	Density (g/cm ³)
0	1.50
1	1.47
5.6	1.32
12	1.10

‘Mud Pie’ Icy Regolith Simulant

Mud pie is a term given to the traditional icy regolith simulant pioneered by several laboratories [Kleinhenz et al., 2013; Gertsch et al., 2008]. The final mud pie product is more analogous to permafrost on Earth. Dry regolith is combined with room temperature water and is thoroughly mixed, creating a ‘mud pie.’ This mixture is then mechanically compressed to a density of 1.5g/cm³.



Figure 5.2.3. Block 1 sample container submerged in LN with LN feed through.

The sample is then placed in a freezer for cooling to 243K or directly cooled in the sample container with liquid nitrogen to 80K. Some measurements show the resulting product is as hard as concrete, [Liu, et, al., 2019; Gertsch et al., 2008]. In addition, the frozen water forms a matrix mixed within the regolith, providing an increase in thermal conductivity. This has been observed in our experiments, described in Section 5.3.3. Water weight percentages (>1%) still produced a product that was hard and had a higher thermal conductivity when compared to other icy regolith configurations.



Figure 5.2.4. ‘Mud pie’ icy regolith simulant, 12% water weight.

Frost Layer Icy Regolith Simulant

In the Frost Layer simulants, it was assumed that areas in a PSR may exist with a higher water weight percentage than normal at the surface. A dry sample of LHS-1 was first cooled to cryogenic temperatures and then using a syringe, small amounts of water were added to the surface as seen in Figure 5.2.5. The liquid water cooled to ice before adding additional water. No liquid water was observed to seep in the regolith. Frost layers were added until 10g (± 0.001) of water had been



Figure 5.2.5. Frost Layer Production, Simulant and Container at 77K.

deposited over an area ~6cm diameter. This approach produced a solid sheet of ice, not a layer of ice grains. The subsurface dry regolith was measured before and after each experiment to determine if ice had migrated below the surface. The results are described in Section 5.3.3.

5.3 Block 1 Testing

The physical state of icy regolith present in lunar PSRs is currently unknown. For Thermal Mining testing, it was desirable to understand how the ice structure plays a role on overall ice yield and to learn the response of the ice in the regolith. Both mud pie and granular icy regolith simulants were prepared with equal water weight percentages. Samples were cooled to cryogenic temperatures, placed in the vacuum chamber and the lamp was powered to simulate sunlight. Ice and regolith mass measurements were taken at the start of every test and post-test mass measurements were made. While pressure data were recorded, the vacuum pump was left on to ensure a low pressure was maintained. Therefore, pressure data could not be used to determine sublimation rates. Instead, tests were conducted at different time intervals and an overall average sublimation rate was recorded. In addition to mass measurements, subsurface temperature measurements were taken to gain a better understanding of the heat transfer into the substrate. Finally, the structure of the icy regolith simulant is affected with the application of heat. Great lengths were taken to carefully deconstruct the simulant samples post-test to observe and record the final state.

5.3.1 Block 1 Test Apparatus

The Block 1 test apparatus included a cryogenic sample container (8.9cm diameter, 7.0cm depth), actively cooled with liquid nitrogen, a lamp to simulate the sun, and various type K thermocouples to record temperature. These were all placed in a vacuum chamber to best simulate

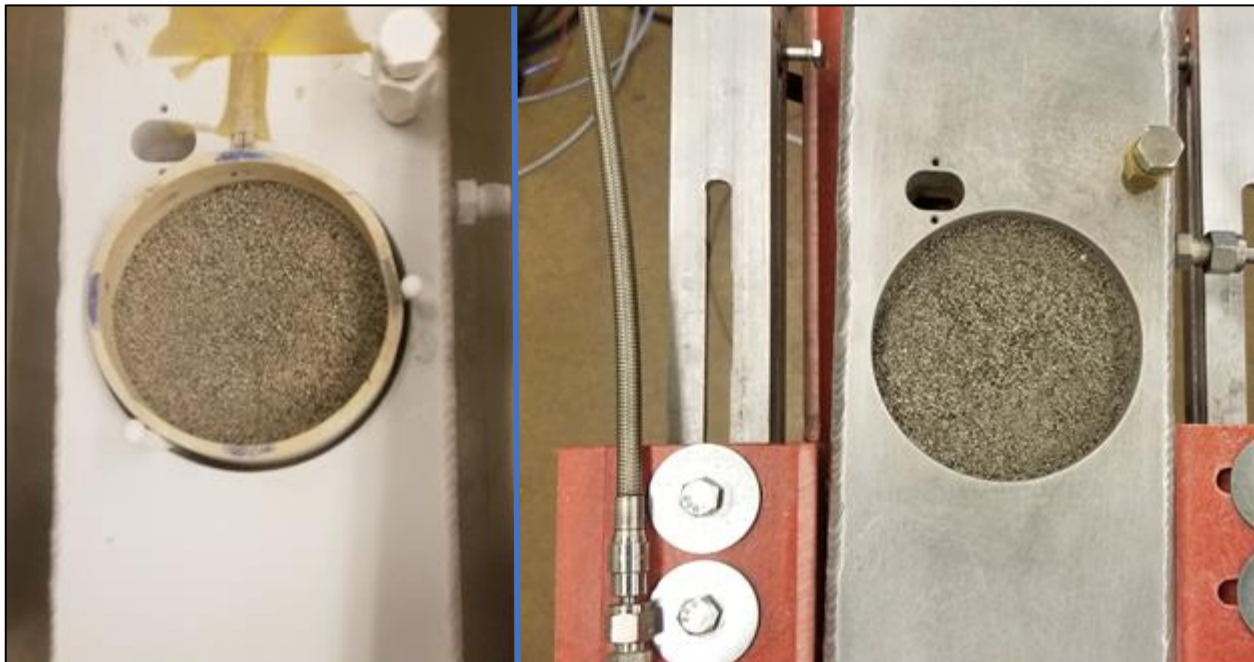


Figure 5.3.1. *Left: Adiabatic Boundary Condition. Right: Isothermal Boundary Condition.*

the environmental conditions on the lunar surface. When icy regolith was poured directly into the sample container the container wall provided an isothermal boundary condition (BC) at liquid nitrogen (LN) temperature. Testing with isothermal boundary conditions constrained the test results described in Section 5.3.3. To reduce heat transfer into the container walls, we inserted a polyvinyl chloride (PVC) sleeve between the cold wall and the sample. The sleeve was separated from the cryogenic walls by a thin gap, with low thermal conductivity separators, which allows a vacuum once under test pressure, reducing the diameter by ~1.5cm. This configuration approximates an adiabatic boundary condition, although the bottom of the sample was still exposed to a cold boundary. Neither boundary condition represents what the actual conditions are in a PSR. This is the main motivation for the Block 2 test configuration discussed below. However, these two configurations provide valuable insight into the behavior of icy regolith simulants under surface heat. Once the cryogenic sample was in place, the lamp was moved into position roughly 1cm above the sample. The lamp and sample container were both operated remotely.

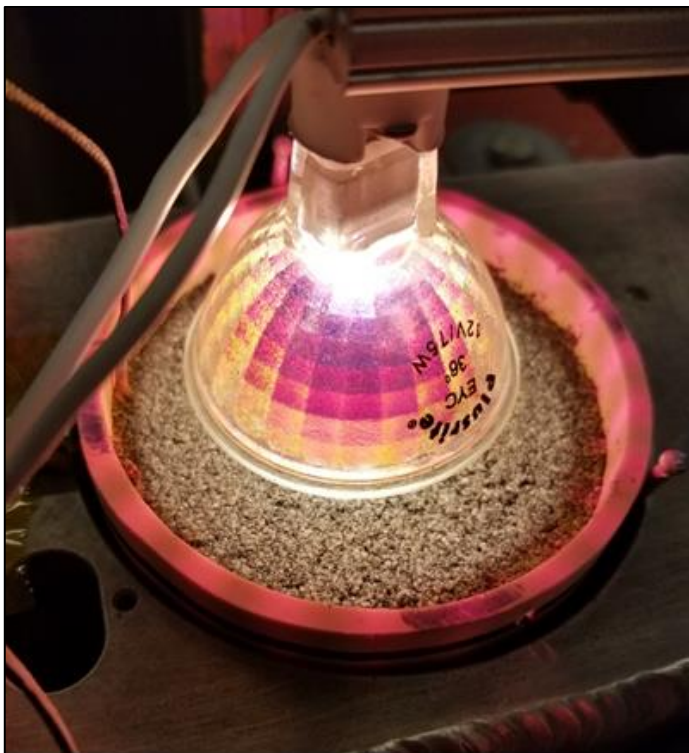


Figure 5.3.2. View from Vacuum Chamber port during an adiabatic boundary test.

in a PSR. This is the main motivation for the Block 2 test configuration discussed below. However, these two configurations provide valuable insight into the behavior of icy regolith simulants under surface heat. Once the cryogenic sample was in place, the lamp was moved into position roughly 1cm above the sample. The lamp and sample container were both operated remotely.

5.3.2 Block 1 Test Methodology

Each test started with the production of the icy regolith simulant. The regolith simulant mass was first dried and then cooled to 243K for a granular sample, while mud pies started production at room temperature. Granular ice or liquid water mass was recorded using a mass scale (Model: USS-DBS3-2) with an accuracy of $\pm 0.001\text{g}$, with a limitation of 200g maximum weight. Post-test measurements, specifically loss of ice, attempted to maximize the use of the USS-DBS3-2 scale, however, some larger measurements ($>200\text{g}$) had to utilize a less accurate scale (PS-25KG) with an accuracy of $\pm 2.0\text{g}$. The desired water weight percentage determined the mass quantities of regolith and added water (or ice).

Once the sample was properly mixed, the sample container was cooled to cryogenic temperatures in a liquid nitrogen bath. The evaporating liquid nitrogen filled the bath container and prevented humidity from the atmosphere to collect on the sample container. Once the sample container reached 77K, the granular ice simulant, initially at 243K, was poured into the sample container and left to cool to cryogenic temperatures. Temperatures were monitored using type K thermocouples at a depth of 2cm and 4cm. Once the temperature at 2cm was 100K, the sample container was moved to the vacuum chamber for final test placement and the lamp was moved into

place. The sample container was exposed to the normal atmosphere during this time (typically no longer than 3 minutes). On days with high humidity, a thin layer of ice developed on all cryogenic surfaces. However, compared with tests on days of low humidity, this did not appear to have a notable effect on overall test results.

The vacuum chamber was then closed and pumped down to a pressure of at least 1×10^{-4} Torr. The pump down time took approximately 60 minutes, during which liquid nitrogen was circulated through the sample container to maintain the cryogenic temperatures. However, the top surface of the icy regolith is radiatively exposed to the room temperature inside of the vacuum chamber causing the temperature at 2cm to climb to 120K. Once the test pressure has been reached, the lamp is turned on and emits the output power of the sun, $0.1371\text{W}/\text{cm}^2$. The lamp was kept on for the entire duration of the test.



Figure 5.3.3. Mud Pie Surface Condition after a 5-hour test.

Typical test lengths were 2.5, 5.0, 10.0 and 20.0 hours. During a test, liquid nitrogen was constantly cooling the sample container. Temperature data was recorded for the duration of the test. Once the test time was complete, the lamp was turned off and the vacuum chamber was brought back up to room pressure with atmospheric air. This was accomplished in approximately 20 seconds. Opening the chamber and moving the sample container to a box or freezer allowed the sample container and sample surface to be exposed to the normal atmosphere for typically no more than 3-5 minutes. Once in the box or freezer, the remaining LN in the sample container would fill the container with N_2 gas and prevent any further condensation from the atmosphere. Overall mass measurements were then taken, and any ice structural phenomena were recorded in a timely manner.

5.3.3 Block I Test Results

Mud Pie Results

The mud pie icy regolith tests with isothermal boundary conditions showed no measurable amount of ice sublimation even after a 20-hour test. All isothermal mud pie tests were performed at 5.6% water weight. The only physical

observation was a desiccated layer of regolith approximately a single grain size deep ($<1\text{mm}$) with a diameter roughly 2.5cm, directly below the lamp.

Table 5.3.1. Mud Pie Results.		
Boundary Layer: Isothermal		
Test Length (hours)	Overall Ice Yield	Overall Sublimation Rate
2.5	null	null
5.0	null	null
20.0	null	null
Boundary Layer: Adiabatic		
Water Weight %	Overall Ice Yield	Overall Sublimation Rate
12.0%	1.18g	0.24g/hr

Only two adiabatic tests were conducted (Figure 5.3.4), each at 5 hours but with different water weight percentages. The 5.6% test had significant ice contamination during a post-test mishap and the test results were discarded. In the 12% test, a small desiccated layer was observed (~4mm).

Comparing Granular Ice Grain Sizes

Each granular configuration was subjected to the same 5-hour test duration, while only adjusting the water weight percentage. Overall yield, sublimation rates and temperature profile data were used to compare the tests. However, the 1% and 5.6% coarse grains tests and 5.6% multi-grain test were determined to have faulty test data due to a low LN flow issue. Thus, only the 12% water weight percentages were used for comparison. See Table 5.3.2. The temperature profiles of each grain size were also compared to determine if heat flow differed greatly between ice grain size, shown in Figure 5.3.5.

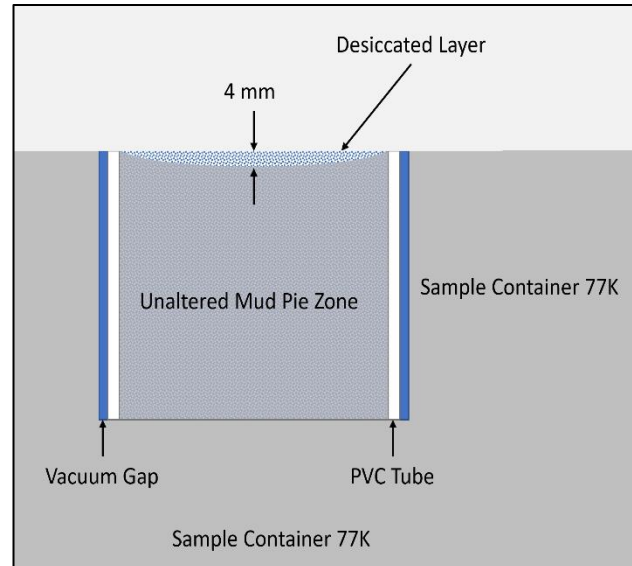


Figure 5.3.4. Cross-Section diagram of mud pie icy regolith physical analysis results.

Table 5.3.2. Comparison of Granular Ice Grain sizes (12% Water weight).

Ice Grain Sizes	Overall yield (g)	Sublimation Rate (g/hr)
Coarse	3.11	0.62
Fine	3.10	0.62
Multi-grain	3.9	0.71

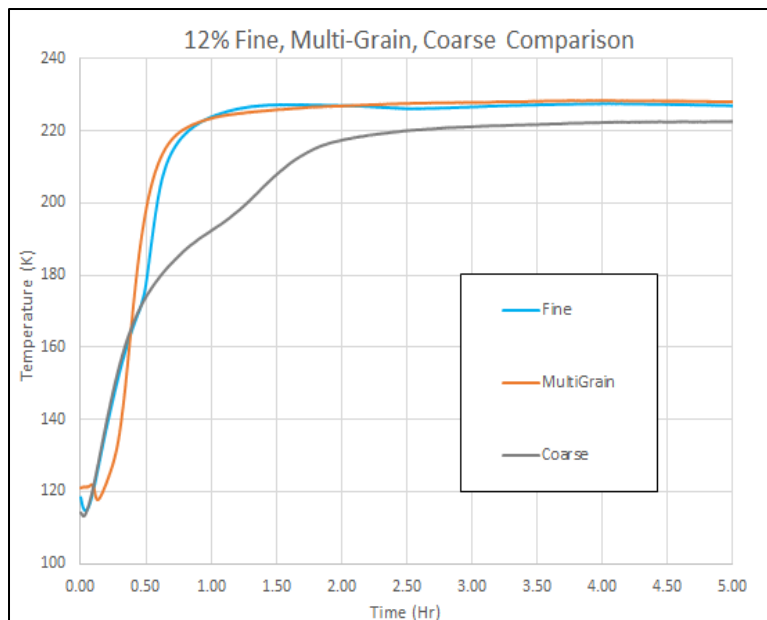


Figure 5.3.5. Temperature profile response of ice grain configurations at depth of 2cm with a 12wt% water.

Granular Icy Regolith Results

For reasons explained in Section 5.5, granular simulant tests were all conducted with fine ice grain sizes. Tests were conducted at various test durations and three different water weight percentages. Tests were repeated at 12% water weight and 5 hours to determine repeatability, which was observed. All granular tests were conducted once unless an error was suspected. The test results are contained in Table 5.3.3. The general post-test structure of the samples is shown in Figures 5.3.6 and 5.3.7 for the isothermal and adiabatic boundary conditions, respectively.

Table 5.3.3. Granular Icy Regolith Tests Results (Fine).		
Boundary Condition: Isothermal		
Water Weight: 12%		
Test Duration (hr)	Overall Yield (g)	Sublimation Rates (g/hr)
5.0	3.10	0.62
Water Weight: 5.6%		
5.0	0.29	0.06
21.5	1.32	0.06
Water Weight: 1.0%		
5.0	0.30	0.06
Boundary Condition: Adiabatic		
Water Weight: 12%		
2.5	2.05	0.82
5.0	3.25	0.65
20.0	6.74	0.34
Water Weight: 5.6%		
5.0	1.29	0.26
20.0	2.70	0.14
Water Weight: 1.0%		
5.0	1.23	0.25

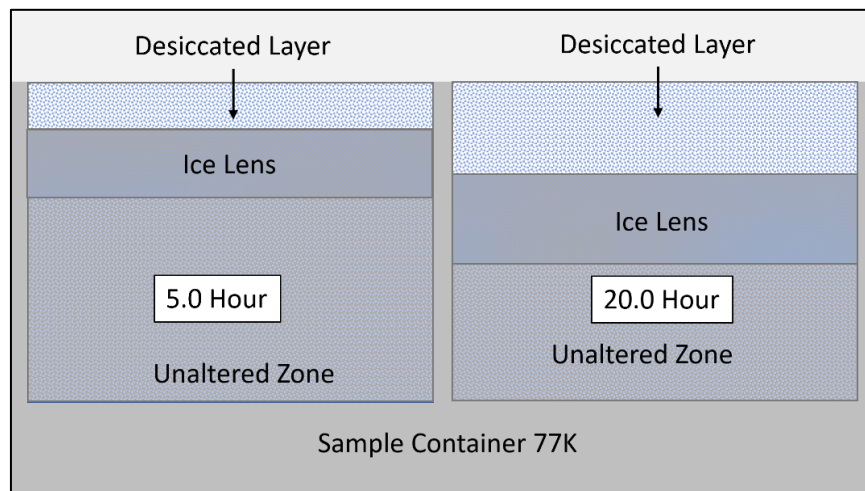
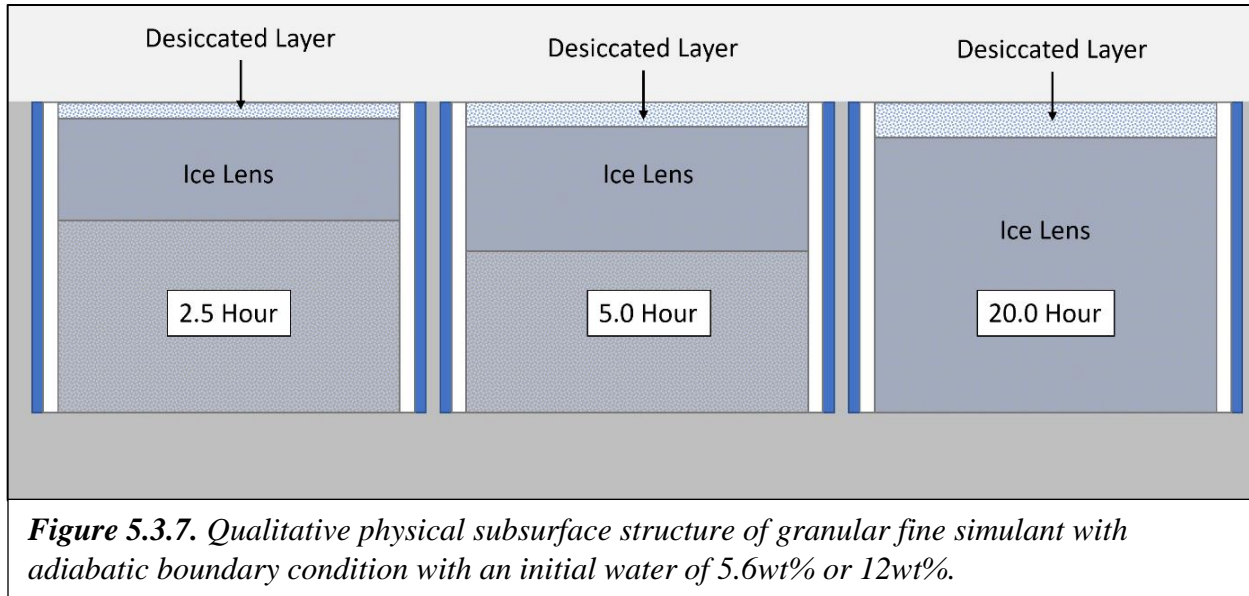


Figure 5.3.6. Qualitative physical subsurface structure of granular fine simulant with isothermal boundary condition with an initial water of 5.6wt% or 12wt%.

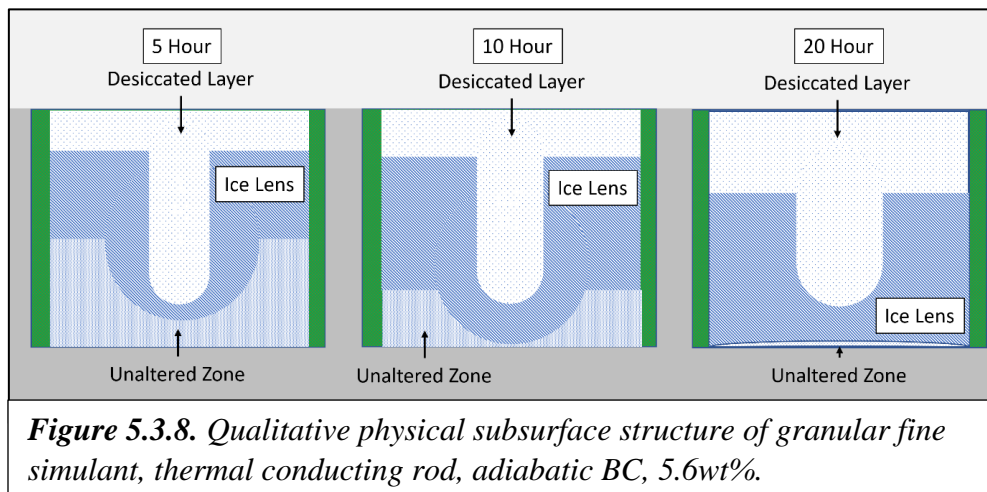


Thermal Conducting Rod Test Results

Based on observations from our initial tests, it was decided to attempt to increase sublimation rates and ice yields by the addition of a conducting rod. The rod was made from a quarter inch copper tube with perforations added. The intent was to provide a path for heat into the subsurface as well as a path for vapor to reach the surface of the sample. See Figure 5.5.7. Test results for the conducting rod are shown in Table 5.3.4. The post-test sample structure is depicted in Figure 5.3.8.

Table 5.3.4. Thermal Conducting Rod Test Results.

Boundary Condition: Adiabatic		
Water Weight: 5.6%		
Test Length (hr)	Overall Yield	Average Sublimation Rate
5.0	2.19g	0.43g/hr
10.0	2.93g	0.29g/hr
20.0	4.26g	0.21g/hr



Frost Layer Test Results

Test results for the frost layer configuration are given in Table 5.3.5. In each case, all the surface ice was sublimated within the 5hr test duration.

<i>Table 5.3.5. Frost Layer Test Results.</i>			
Test Number	Overall Yield	Ice Migration	Sublimation Rate
Test 1	10g	null	5g/hr
Test 2	10g	null	5g/hr

Ice Redistribution in the Simulant

Only a small number of tests were able to provide ice mass measurements post-test. The results are tabulated below, and they help describe how ice migrated during tests. Desiccated mass is the mass of regolith that had ice measurements less than 0.5% post-test. Total Ice is the mass of ice that would have originally existed in the desiccated layer. Sublimated Ice is the total amount of ice measured to be missing post-test. Redistributed Ice is the difference between total ice and sublimated ice that must have been redistributed back into the regolith simulant.

<i>Table 5.3.6. Ice Distribution Data.</i>				
Boundary Layer: Adiabatic				
Water Weight: 12%				
Icy Regolith Configuration: Granular (Fine)				
Test Length (hr)	Desiccated Mass	Total Ice	Sublimated Ice	Redistributed Ice
2.5	25.1g	3.42g	2.05g	1.37g
5.0	37.4g	5.10g	3.25g	1.85g
20.0	70.4g	9.60g	6.74g	2.86g
Icy Regolith Configuration: Mud Pie				
5.0	8.65g	1.18g	1.18g	0.0g

Temperature Profile Test Results

Temperature profile data were taken at a depth of 2cm and 4cm. Not all tests had functional thermocouples and most tests has similar temperature profiles. The primary benefit of the temperature measurement was to gain understanding of heat transfer into the regolith. Figures 5.3.9 and 5.3.10 show representative temperature profiles for tests with the isothermal boundary condition. Figures 5.3.11 and 5.3.12 show temperature profiles for tests with the adiabatic boundary condition.

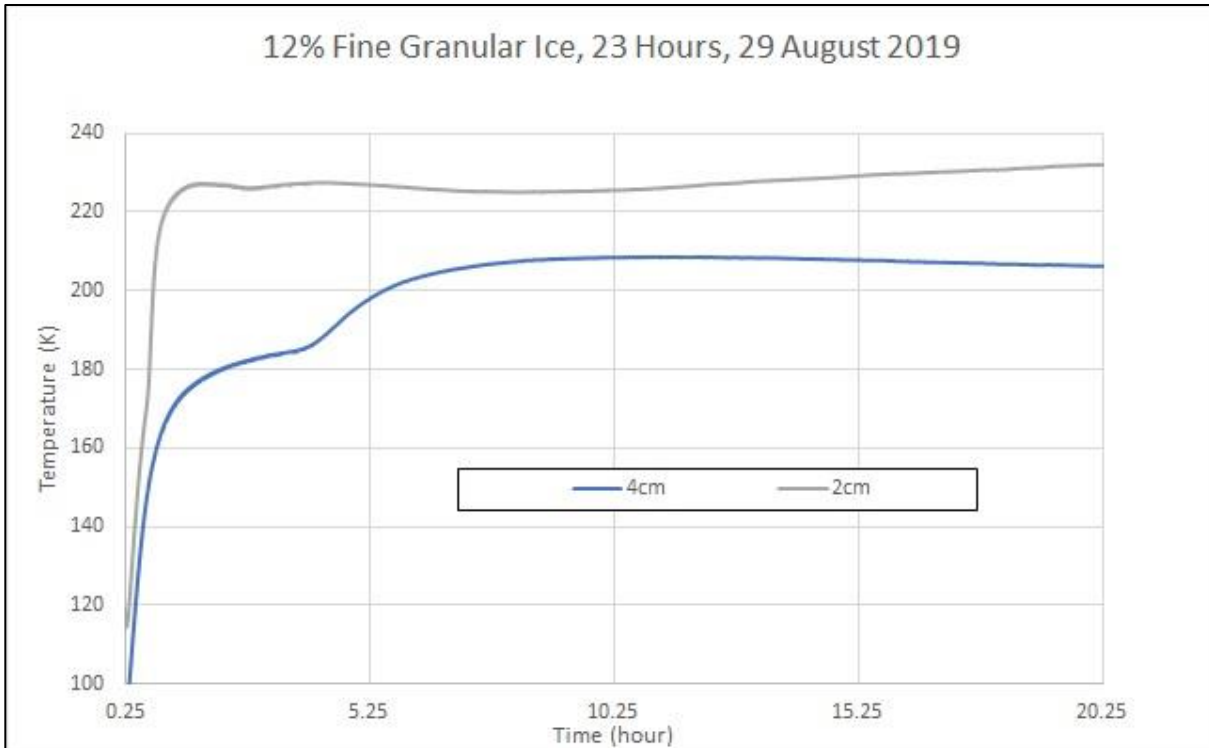


Figure 5.3.9. Temperature profile: 12% Granular Ice, 23-hour test, Isothermal BC.

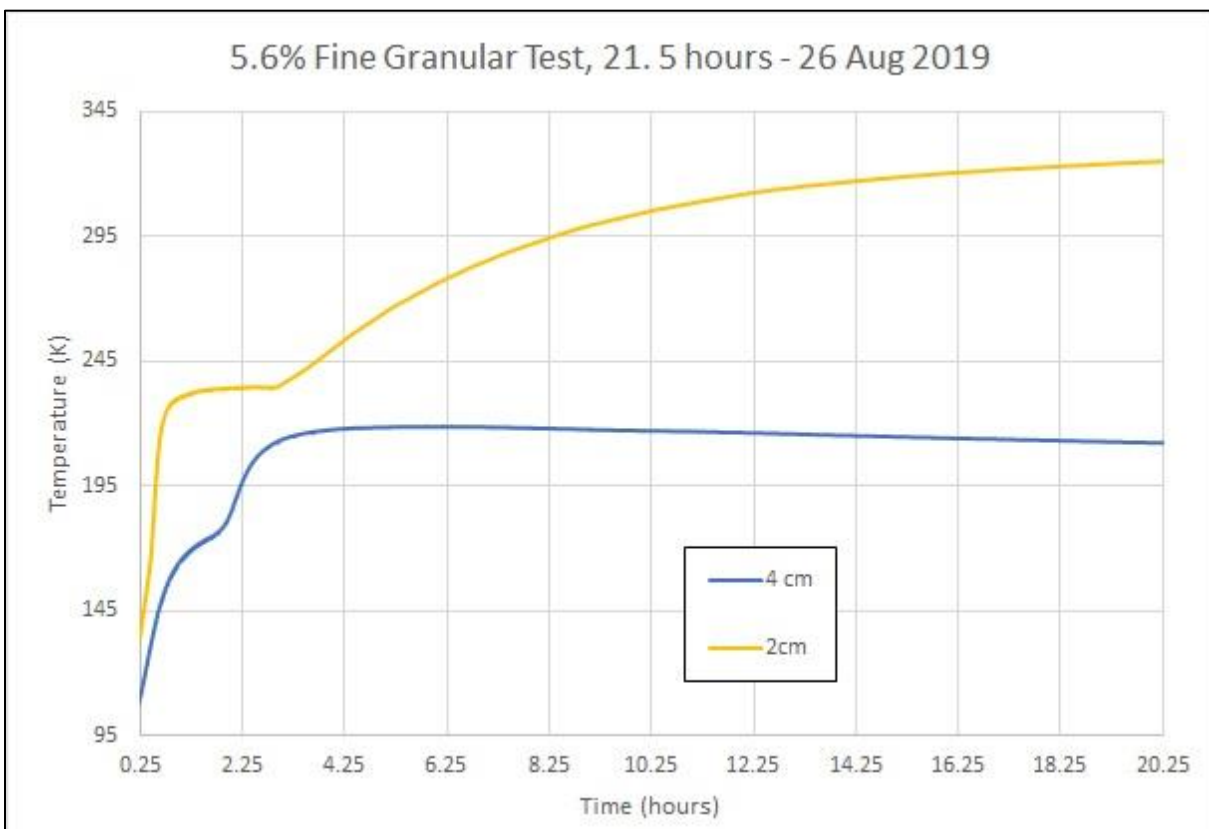


Figure 5.3.10. Temperature profile: 5.6% Granular Ice, 20-hour test, Isothermal BC.

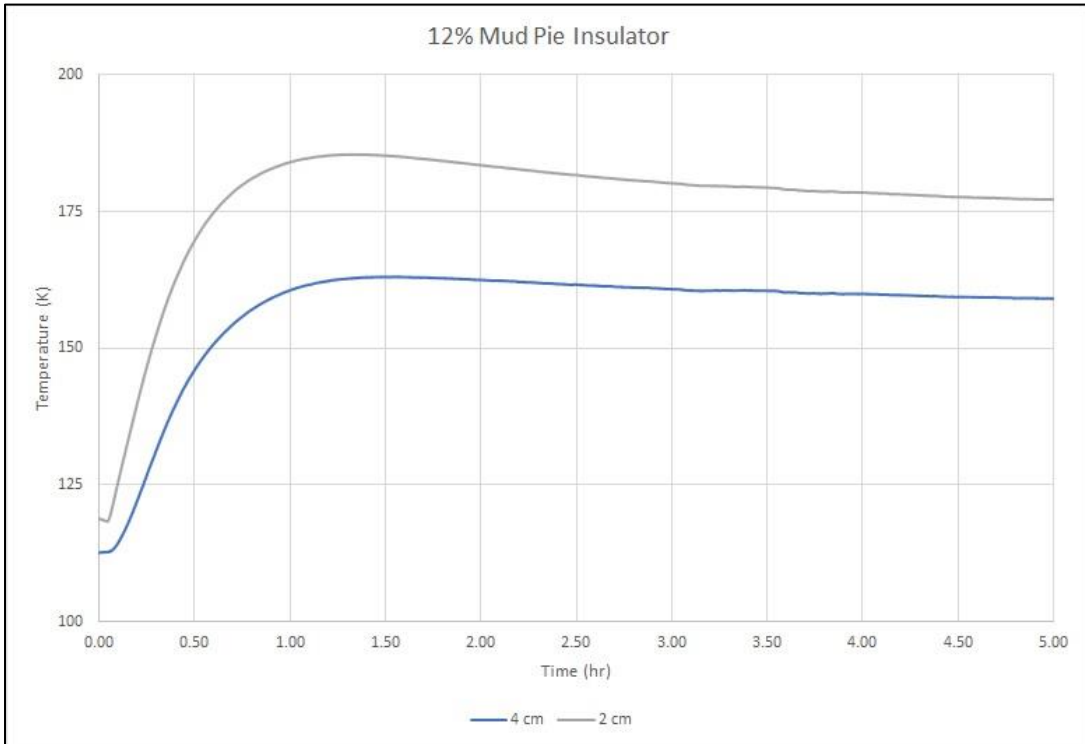


Figure 5.3.11. Temperature Profile: 12% Mud Pie, Adiabatic BC.

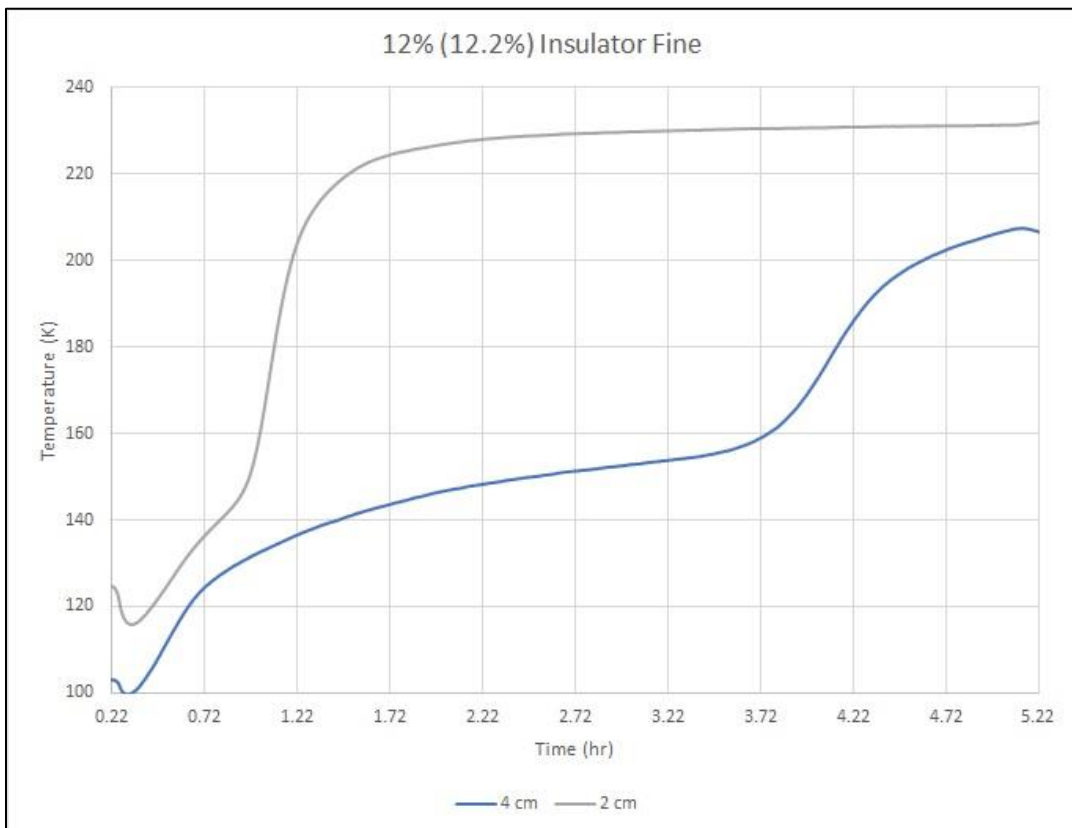


Figure 5.3.12. Temperature profile: 5.6% Granular, Adiabatic BC.

Icy Regolith Cool Down Times

The rate of cooling of icy regolith samples during cool down gives us an indirect and relative measure of thermal conductivity, as shown in Figure 5.3.13. These results are consistent with our other test results. For example, the relatively high thermal conductivity of the mud pie simulant provides a thermal short to the cold wall boundary, preventing the sample from reaching the temperature needed for ice sublimation.

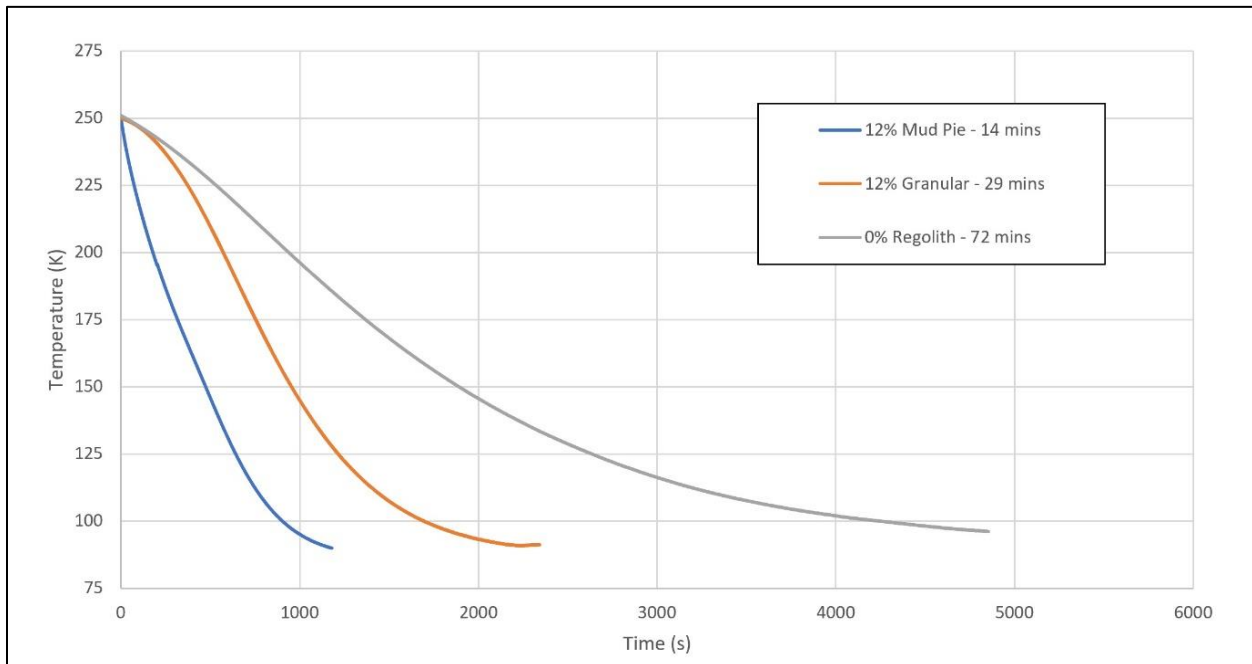


Figure 5.3.13. Temperature profile during cryogenic cooling of different water wt% icy regolith configurations.

5.4 Block 2 Testing

An improvement is required on the Block 1 apparatus to better simulate the boundary conditions that will exist in the PSR environment and to provide a test apparatus more analogous to the Thermal Mining system. Our intent was to include a series of tests with the Block 2 apparatus in the Phase I program, however, due to fabrication delays, the Block 2 apparatus was not available for testing in this phase.

5.4.1 Block 2 Test Apparatus

The Block 2 apparatus doubles the radius of the sample container, pushing the isothermal boundary further away from the source of the heat. In addition, a cover plate above the sample adds an additional thermal boundary layer that would simulate the background of space. However, the background temperature of space is ~3K, while the lowest temperature achievable with LN cooling is 77K. However, this is an improvement over the Block 1 apparatus, which is exposed to the vacuum chamber at room temperature. The Block 2 apparatus also uses a removable sample container which allows the before and after mass measurements that are required to get an accurate overall ice yield. An optional cone fits over the lamp to act as a simulated tent.

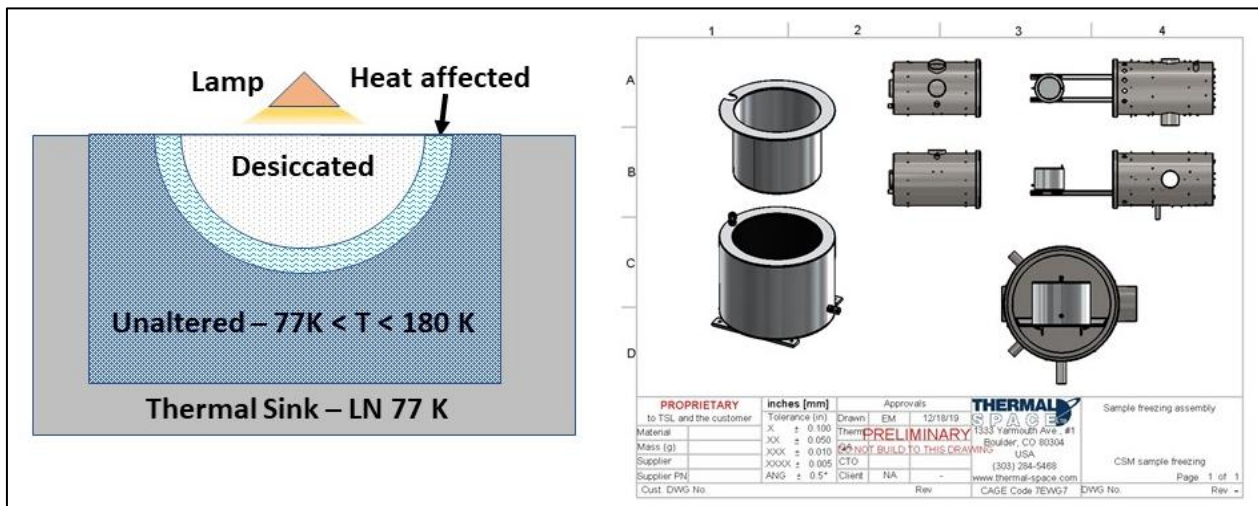


Figure 5.4.1. The Block 2 testing apparatus. Left: Schematic showing expected ice distribution after testing. Right: Design drawing of apparatus in the CSM medium vacuum chamber.

5.4.2 Block 2 Test Methodology

Block 2 testing will take place in the CSM medium chamber following a very similar methodology to Block 1.

5.4.3 Block 2 Test Results

Due to delays in the fabrication of the Block 2 test apparatus, we were not able to accomplish any Block 2 testing during the Phase I study.

5.5 Test Conclusions

Mud Pie Results

As can be seen in Table 5.3.1, the isothermal boundary condition test results showed no measurable amount of ice leaving the system with the mud pie icy regolith. This was true for all tests with 5.6% and 12% water weight percentages, including a 20-hour test. We suspect the ice structure in the mud pie allowed the heat to quickly transfer from the lamp, through the regolith to the LN-cooled sample container. With an adiabatic boundary condition, the LN-cooled boundary layer was now only at the bottom surface, while the sides of the sample were adiabatic. However, only a small amount of regolith near the surface was desiccated, while the remaining sample was unaltered. A comparison of cool down times among our different sample types, as shown in Figure 5.3.13, shows that the mud pie cooled the fastest in 900 secs, while the granular sample cooled in 1700s and the dry regolith reached 100K at 4200s. This is confirmation that even though the water weight was the same in both samples, the ice structure in mud pie configuration allows for a higher thermal conductivity. The adiabatic test also shows indications of high thermal conductivity with its temperature profile during the test shown in Figure 5.3.11. At a depth of 2cm and 4cm, the temperature clearly starts to rise; however, roughly 1.25 hours in, the temperature stops increasing and slowly begins to cool. Our hypothesis was that as the ice near the surface sublimated away as shown in Figure 5.3.4, the heat entering the sample was unable to keep up with the heat leaving the sample through the cold wall boundary. This effect was also suspected in granular tests, but with lower bulk thermal conductivities.

Tests with mud pie simulants showed no ice migration with either boundary condition. This implies that the pore space of the sample was nearly 100% filled with frozen water. This prevented water vapor from migrating down into the sample.

The Block 2 apparatus is expected to improve the boundary conditions allowing a greater temperature gradient to develop even in mud pie simulants. However, we strongly believe the mud pie configuration would not exist in a lunar PSR. Regolith in PSRs is subjected to the same gardening events that occur all over the Moon. This would imply that, as ice and regolith mixtures are shattered, they return the surface in a more granular configuration. Further discussion in the section below, “Granular Test Results”, explains various icy regolith configurations that may exist in a PSR.

Granular Ice Grain Size Comparison

Granular icy regolith is more representative of what we expect to see in a PSR. In the granular configuration, the cryogenic ice exists as grains of similar size to the regolith grains since both were subjected to the same gardening forces. However, the size distribution of these ice grains is uncertain. To compare the effect of different grain sizes, three samples of different grain size were prepared with a water weight percentage of 12.0% and tested for 5 hours. The ice grain sizes are described in Table 5.3.2: fine, coarse and multi-grain. The multi-grain was designed to have a grain size distribution similar to the LHS-1 simulant. This was accomplished in a freezer using various sieves. Table 5.3.2 also shows the overall ice yield and sublimation rates. While the multi-grain does show a slightly higher ice yield, the standard deviation of the three grain size types was only 0.21g overall yield relative to an average yield of 3.37g. More tests are warranted to explore

the gran size distribution effect, but given that the measured effect was small, we elected to focus on just fine grain samples for the purposes of this study.

A comparison of the temperature profiles is shown in Figure 5.3.5. The fine and multi-grain showed nearly identical temperature profiles. This may be explained by the fact that in the multigrain sample, 80.7% of the ice grains were fine. The coarse grain test showed a delayed temperature increase but finally settled near the same constant steady state temperature. This temperature delay is believed to be due to a somewhat lower thermal conductivity of the coarse grain sample. The total ice mass is contained in a smaller number of grains. Thus, heat must travel through lower thermal conductivity regolith before it can travel through the ice grain.

Another consideration was the time to produce fine, coarse and multi-grain simulants. Granular ice was produced with an ice machine in a freezer. As large cubes of ice were disaggregated, only 10% of the resulting ice grains were coarse, 20% fine and the remaining ice grains medium. To produce larger quantities of fines, the medium and coarse grains were simply run through the ice machine again to create smaller ice grains. However, storing coarse and medium grains took up valuable room inside the freezer and it was ultimately decided the differences between fine and multi-grain weren't large enough to exclusively test with multi-grain. All further granular tests described below were conducted with fine ice grain configurations due to similarity to multi-grain and ease of production.

Granular Test Results

The bulk of the Thermal Mining tests were accomplished using granular icy regolith. General trends show that tests with a higher water weight percentage yield more ice, while longer tests show more overall ice yield but a reduction in overall sublimation rate. Yield is defined as the mass of ice verified to have left the sample. This implies that the instantaneous sublimation rate was greatest at the beginning of the test, then decreased over time. As seen in Figure 5.5.1, the sublimation rate approaches zero toward the end of the longer tests. We believe the closeness of the cold LN boundary is prematurely turning off the sublimation process. The isothermal boundary conditions, including the isothermal boundary at the bottom of the adiabatic tests, are

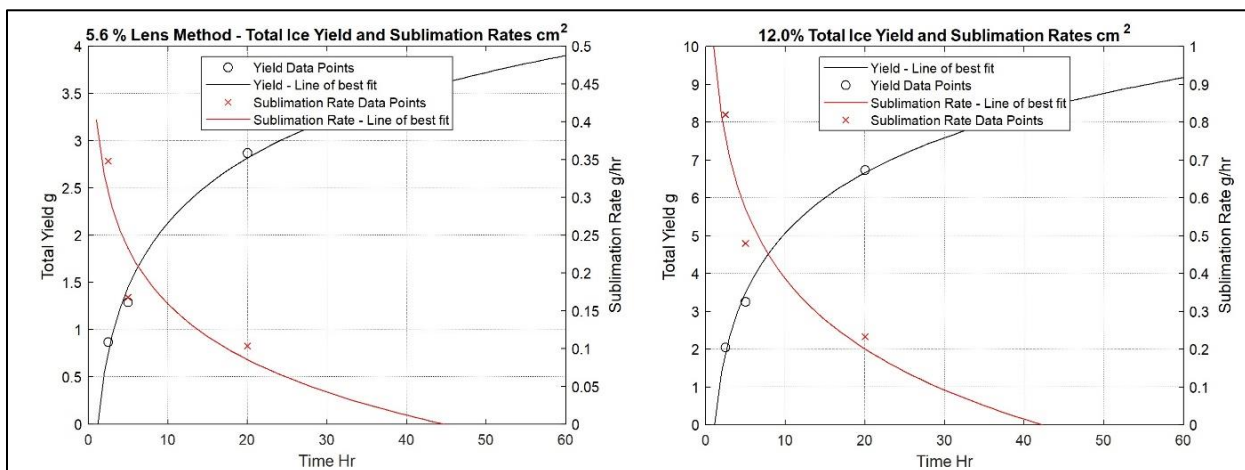


Figure 5.5.1. Granular Sublimation rates for 5.6% and 12% per cm^2 , with adiabatic boundary conditions. Data points are experimental results and solid lines are best fits to the data.

overwhelmed the heat input from the lamp. Other mechanisms that drive the reduction in sublimation rates are discussed in the section below, “Describing Heat and Mass Transfer in Cryogenic Icy Regolith”.

In contrast to the mud pie tests, granular ice tests showed structural changes within the icy regolith. In samples with 5.6% and 12% weight percentages, a desiccated layer formed near the surface, followed by a section of regolith we termed the ice lens. See Figures 5.5.2 and 5.5.3. The ice lens has two zones: a dark hard thin cap near the top, and a larger

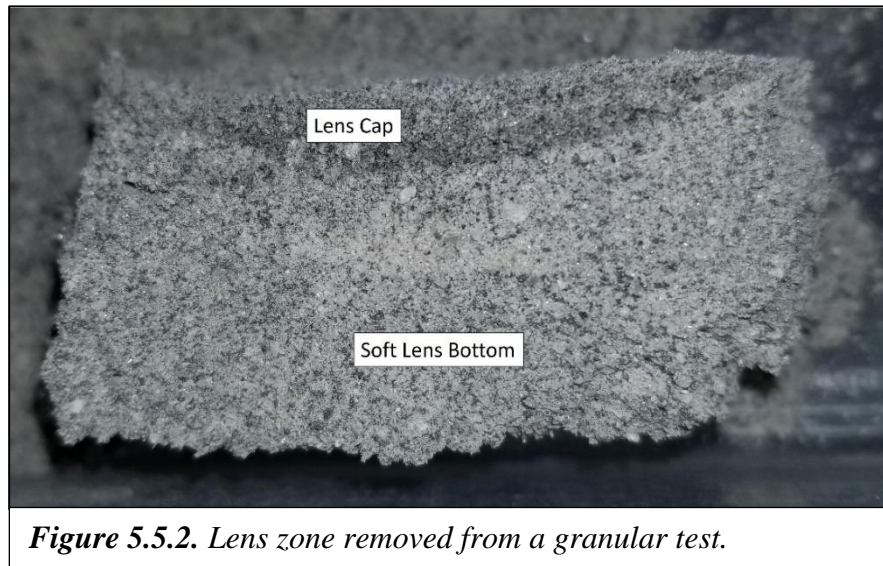


Figure 5.5.2. Lens zone removed from a granular test.

bottom lens with the hardness of a dry sandcastle. The bottom lens would hold its shape but would crumble under light forces. A layer beneath that remained granular ice is called the unaltered zone. The lens zones would generally grow over time, but growth rate slowed as time went on.

The desiccated layer in both isothermal and adiabatic tests was typically between 1–1.5cm thick after 20 hours. Exact measurements were difficult as the samples would often crumble during the measurement process. This desiccated layer sometimes could be poured out allowing us to weigh it and determine how much ice had left this zone.

In all granular ice tests, a portion of the ice sublimated out of the sample was removed by the vacuum pump while some ice migrated back into the sample. See Table 5.3.6. Portions of the lens were measured before and after drying. Typically, lens areas near the edges of the sample had a higher than original ice content. If the sample was initially 5.6%, the edges of the lens may have been as high as 8% water weight, while the center of the lens was generally around the original amount.

Just above the lens and below the desiccated layer was a thin, dark layer, typically with lower than the original water weight percentage. We believe this area was a zone of active sublimation with vapor transport to the surface or further into the sample. One hypothesis is that as ice sublimates, water vapor pressure increases in the regolith pores. Then, the localized area cools due to sublimation and high-pressure water vapor pressure refreezes on the regolith. In addition, pressure momentarily spikes as water vapor flows through tight pore spaces, allowing water vapor again to refreeze. This would explain why this dark, thin lens cap is quite hard. Hardness measurements were not taken; however, this lens cap could be snapped like a cracker. Note that the dark layer and lens are far weaker than the mud pie simulants.

The softer lens bottom reached temperatures that would allow sublimation, however we believe there wasn't enough pressure to allow the water vapor to flow. Only a light redepositing of ice occurs, creating this relatively weak transformed zone. The structure is analogous to a dry

sandcastle. A lens would always develop in 5.6% and 12% samples, but not in 1% samples. Ice is likely redistributing in samples at 1%, but there simply isn't enough ice to develop a strong structure.

Subsurface temperature profiles showed a change in slope between 160–180K. Some tests were stopped when this measurement reached 180K to confirm that indeed an ice lens had developed. It's believed the ice lens, which undergoes a clear structural change, also



Figure 5.5.3. Typical lens found in 5.6% and 12.0% granular tests.

has a higher thermal conductivity than the granular mixture, which allows the temperature to increase quicker than unaltered granular icy regolith. This effect is seen in Figures 5.3.9, 5.3.10 and 5.3.12. This temperature profile change was seen in every 5.6% and 12.0% water weight granular test. As temperatures continue to rise, water vapor pressure rises and starts to push water vapor up out through the desiccated layer and down into colder regions. However, water vapor travelling into the sample will redeposit as the temperature decreases with depth. Water vapor pressure and deposition rates strongly correlate to temperature [Andreas, 2006], as seen in Figure 5.5.5.

Frost Layer Results

The Thermal Mining system is developed to specifically collect surface and near subsurface ice in the PSRs. Since the overall ice stratification is unknown, tests were developed to understand the sublimation rates of a frost layer of ice at the surface. As can be seen in Table 5.3.5, the entire frost layer was sublimated away. Visual observations show that at 1.5 hours, only trace amounts of ice were visible and by 2 hours no ice was visible. Pre- and post-test mass measurements showed no measurable amount of ice had migrated down, implying that the bulk of the ice on the surface would be recoverable.

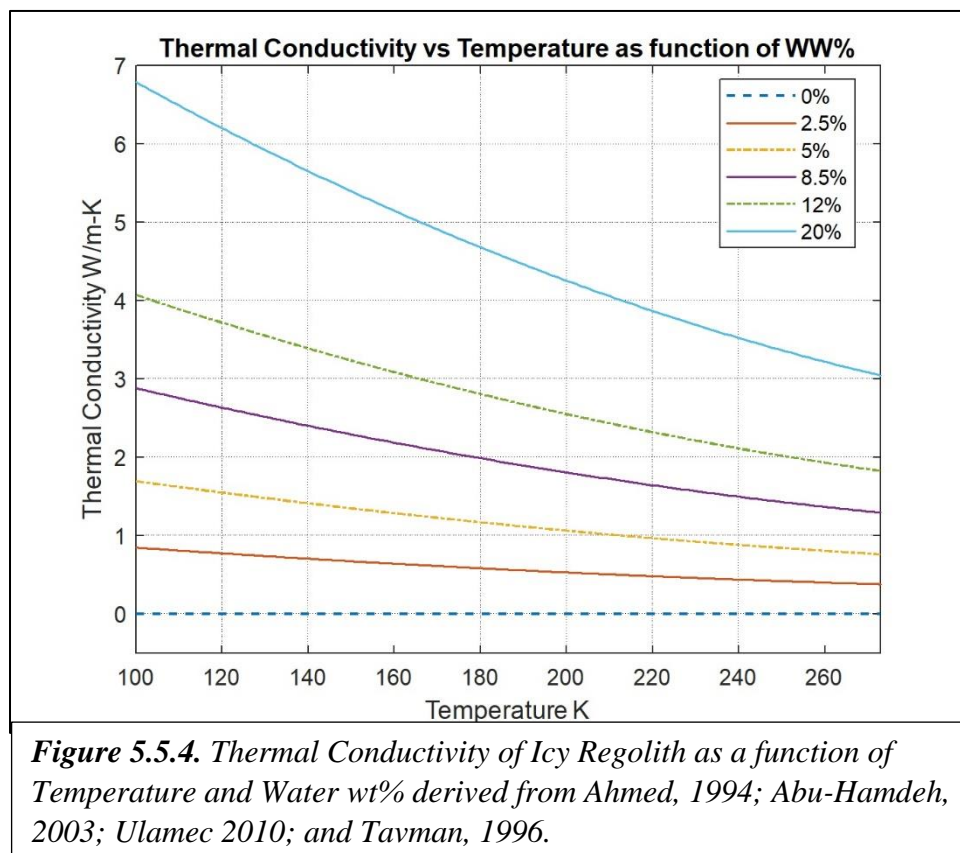
Describing Heat and Mass Transfer in Cryogenic Icy Regolith

Upon completion of mud pie, granular and frost layer tests, we sought a better understanding of the heat transfer and vapor transport mechanisms in these icy regolith samples. This section describes our initial efforts.

Heat is supplied to icy regolith via radiation from the source lamp to the surface. Heat at the surface is transferred conductively between ice grains and regolith grains and convection of escaping water vapor. For this discussion, water vapor pressure contributing to thermal convection is negligible when compared to conductivity. The thermal conductivity of dry lunar regolith is around 0.001 W/m² measured during Apollo missions and using Apollo samples [Ulamec, 2010]. We did not have the ability directly measure the thermal conductivity the LHS-1 regolith simulant used in the experiments, but LHS-1 is similar to the Apollo 16 mission samples in both chemical composition and grain size distribution. Notable differences are the unknown porosity effect due to Earth gravity and the absence of agglutinates. However, we suspect the thermal conductivity of LHS-1 is within the same order of magnitude as lunar regolith, making dry LHS-1 a very poor conductor of heat. This was observed in the temperature profiles seen in Figure 5.3.13. This effect ultimately impedes heat traveling through a desiccated dry layer. In addition, the presence of ice in any form (granular, lens or mud pie), dramatically increases the bulk thermal conductivity of icy regolith [Batir, 2017]. We used the geophysical equation to determine the bulk thermal conductivity of a mixture of grains [Tavmen, 1996]:

$$k_{eff} = \frac{k_{ice}k_{reg}}{\varepsilon k_{reg} + (1-\varepsilon)k_{ice}}, \text{ where } \varepsilon \text{ is the regolith porosity and } k \text{ is the thermal conductivity.}$$

Figure 5.5.4 compares thermal conductivity to water weight percentage. Even a small amount of ice can cause a dramatic increase in thermal conductivity.



As shown in our tests, thermal conductivity works against ice production via heating from the surface in two ways. First is the restriction of heat added from the top through dry regolith as the desiccated layer grows in thickness. Second is a subsurface layer that has higher thermal conductivity and contacts the LN-cooled sample wall container, allowing heat to ‘short’ to the walls. This prematurely slows the temperature increase in the sample and stops the ice from reaching a high enough temperature for fast sublimation, as seen in Figure 5.3.11. In comparison to the actual PSR, the boundary condition will be neither isothermal or adiabatic and heat applied to the surface will raise the temperature at greater depths than seen in our Block 1 testing.

The second important regolith parameter is the permeability of both icy regolith and dry regolith. The best analogous data to LHS-1 at this time are the actual permeability readings of highlands samples from the Apollo missions. The Apollo samples had a permeability of 7×10^{-12} Darcy, a very low permeability [LaMarche, 2011]. This restricts the ability for water vapor to flow out to the surface. By reviewing the equation for flow through a porous medium, the other restricting factors are the pressure to push the gas out and the thickness of regolith to push through. In the case of Thermal Mining, pressure is directly related to water vapor pressure, which is a strong function of temperature as seen in Figure 5.5.5.

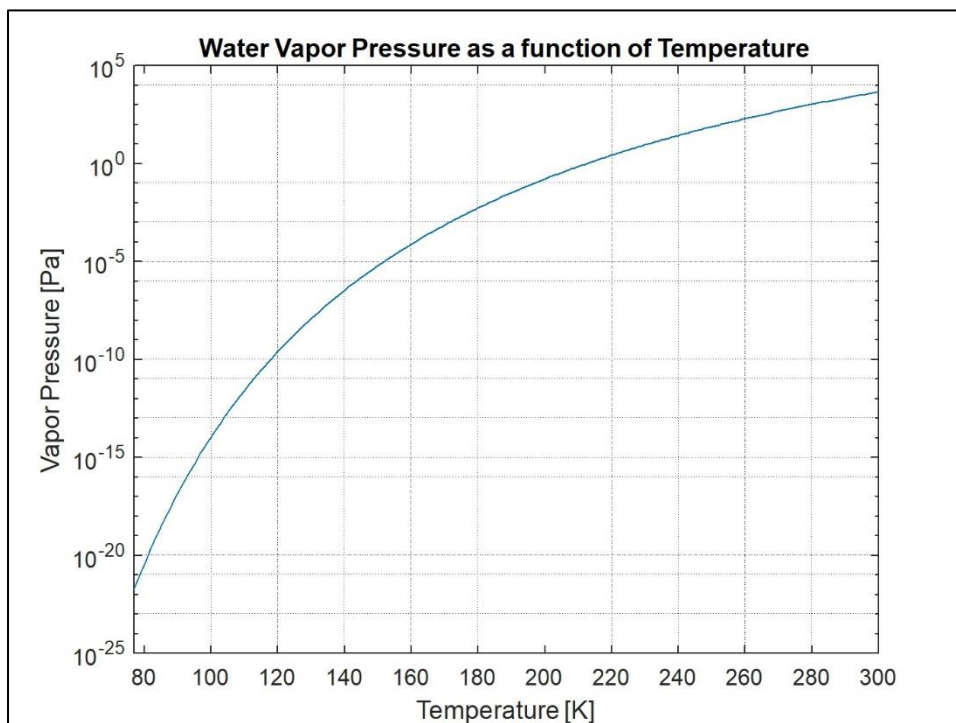


Figure 5.5.5. *Water Vapor Pressure as function of Temperature, derived from Andreas, 2006.*

We know from direct sublimation rates that ice begins to sublimate at a fast rate around 180K, which correlates with Thermal Mining experiments [Andreas, 2006]. The lens zone develops between 160–180K. However, temperature readings in 20-hour tests at a depth of 4cm have reached above 220K, as seen in Figures 5.3.9 and 5.3.10; yet the ice doesn’t leave the sample. The desiccated layer from 5 hours to 20 hours has only grown a few millimeters in the span of 15

additional hours. This leads to the conclusion that the water vapor pressure may not be sufficient to effectively allow flow of sublimated ice even though the ice is ‘hot’ enough to sublimate. Using the permeability and porosity of actual lunar regolith, the expected vapor transfer rate out of the sample as function of temperature and depth can be represented as:

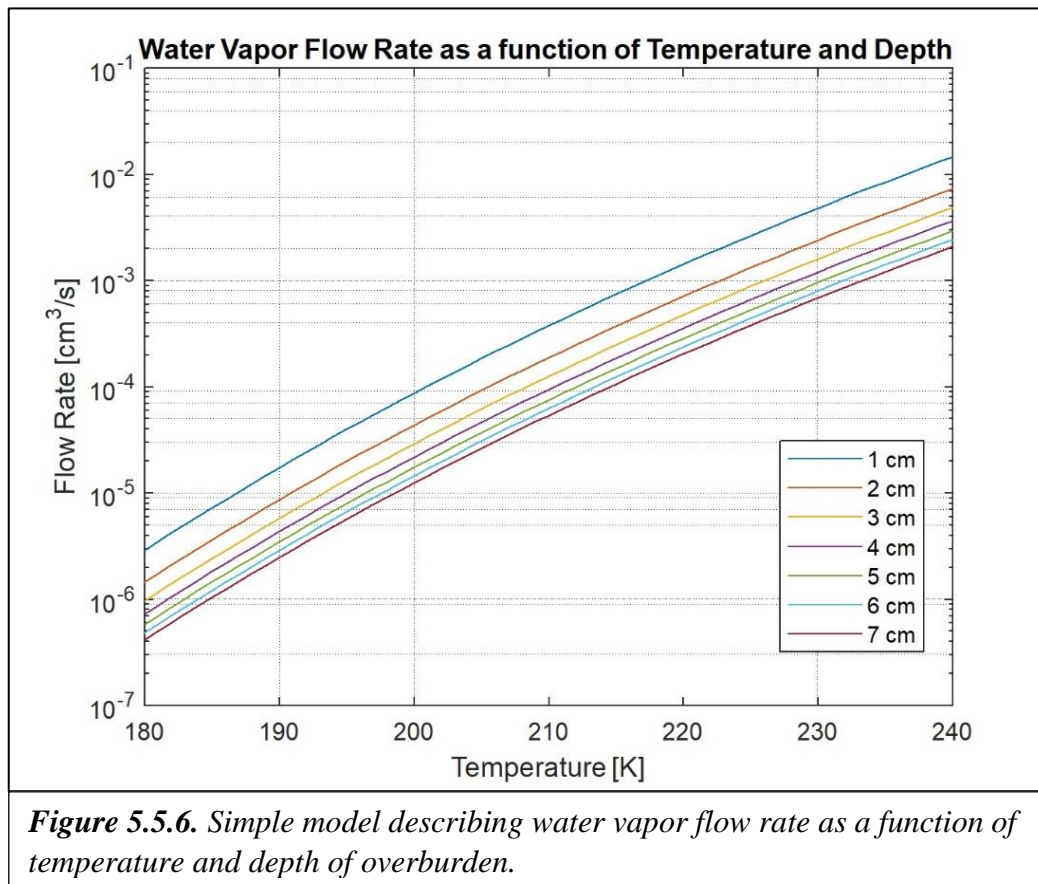
$$Q = \frac{kA}{\mu d} (P_{vap} - P_{vac}),$$

where k is the permeability, A is the cross-sectional area, μ is the fluid viscosity and d is the depth. The vapor pressure is given by Andreas, 2006:

$$P(T) = \exp(9.550426 - 5723.265/T + 3.53068 * \log(T) - 0.00728332 * T).$$

Vapor flow rate as a function of temperature and depth is shown in Figure 5.5.6.

This leads to a general conclusion: the deeper ice is below the surface, the more the temperature must be increased to keep pressures high enough to push water vapor out of the ever-growing overburden at an effective rate.



Thermal Conducting Rod Results

Understanding that heat needs to penetrate further into the surface to increase water vapor pressure and that overburden restricts the flow of gas, a modification was tested that would conduct heat deeper and allow water vapor to flow out. This was accomplished via the use of a hollow conducting rod. The thermal conducting rod used in our tests is a simple perforated copper tube.

A ¼ inch outer diameter copper tube was cut to length to be 1cm above the bottom surface of the sample container and extend 1cm above the surface. A screen was used to keep icy regolith out of the tube. Copper has a thermal conductivity of 385W/m². Therefore, when compared to icy regolith, heat in the copper builds up and flows throughout the entire length of the copper tube far more easily. Temperature readings of the copper tube showed a near constant temperature of 400K was reached within an hour of the beginning of the test. This heating was only accomplished by the lamp radiating above the surface.

This allowed heat to penetrate deeper into our icy regolith simulants. Since the tube was perforated and hollow, as ice reached temperatures to sublime, the water vapor had a shorter distance to travel through a porous medium before reaching the surface.

As can be seen by comparing Table 5.3.4 to Table 5.3.3, the overall yield and sublimation rate is higher with the conducting rod than with surface heating alone. Post-test analysis showed that during long tests, the maximum thickness of the desiccated zone away from the thermal conducting rod was approximately 1cm. However, from the center of tube to

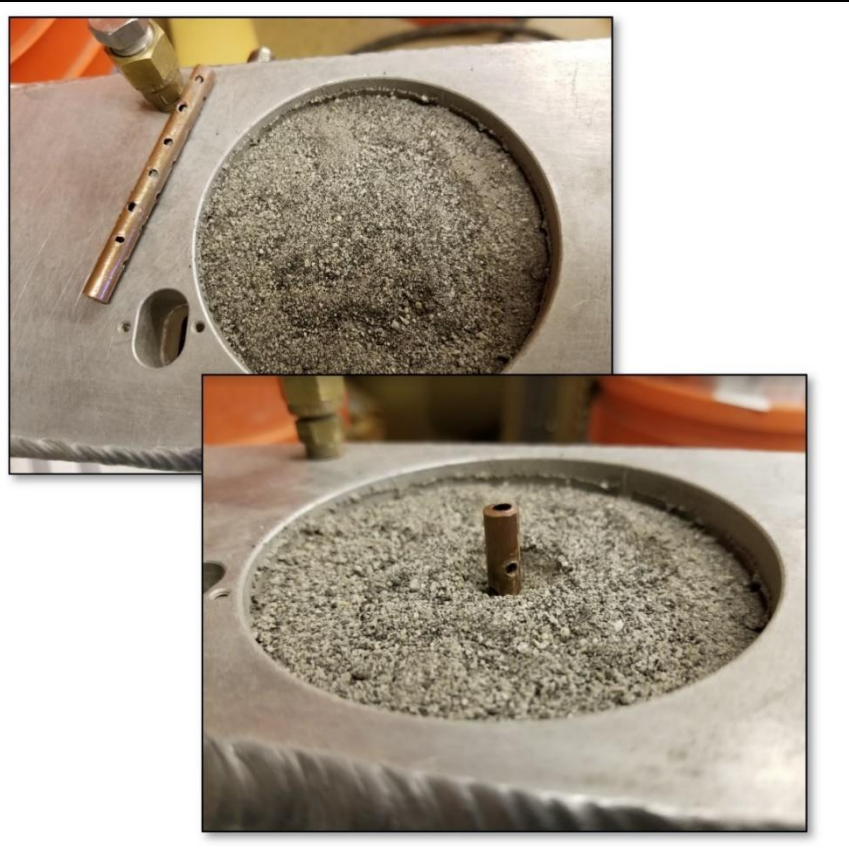


Figure 5.5.7. Thermal conducting rod inserted into granular icy regolith.

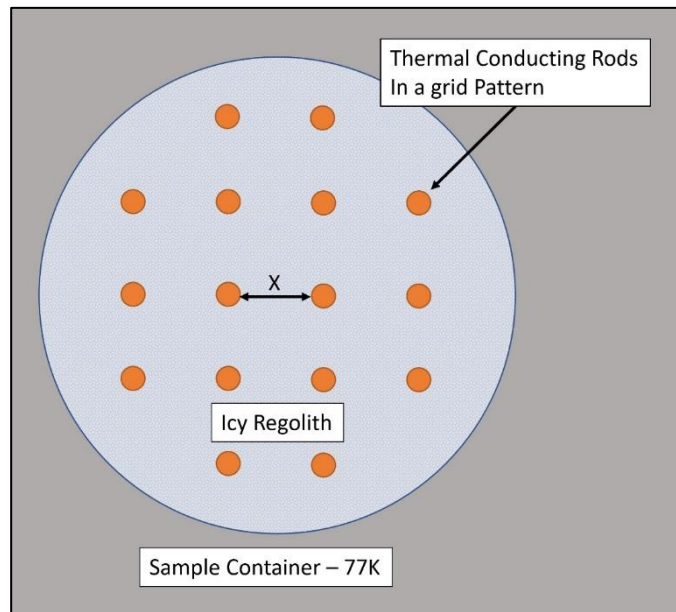


Figure 5.5.8. Top view thermal conducting rod grid layout.

the LN-cooled wall is only 3.5cm. Again, the boundary conditions work against simulating a realistic PSR environment.

Further testing of multiple thermal conducting rods is highly desired. Arranging thermal conducting rods in a grid pattern with an appropriate spacing could result in 90% or greater recoverability of ice to the depth of the rods. Understanding the optimal spacing between rods

under more realistic boundary conditions would allow us to design an optimal conducting rod system to augment surface heating if needed.

Summary

Our Block 1 test program met its main objective of demonstrating the feasibility of sublimating economically viable quantities of ice via surface heating. We showed that surface ice is quickly sublimated with surface heating. This is an important finding given the indications of surface ice within lunar PSRs. Furthermore, using the granular mix simulant, just surface heating generated measurable sublimation of near subsurface ice, but the process was limited by two effects, one of which is an artifact of our test apparatus. This is the proximity of the cold wall boundary to our heat source and the relatively small size of our sample. This effect will be largely eliminated by future testing using the Block 2 test apparatus.

The other effect would be expected in the full-scale lunar application. This is the generation of a desiccated layer of regolith at the surface. As we begin heating, ice at the surface and in the very top layers is quickly sublimated. The regolith grains left behind form an ever-growing layer of desiccated regolith. This layer inhibits further ice production in two ways. It functions as an insulating barrier, reducing heat conduction from the surface into the subsurface. It also acts as a vapor barrier, blocking the flow of water vapor from the subsurface to the surface. This effect is greatly dependent on the permeability of the dry lunar regolith in lunar gravity. Our testing has demonstrated that the use of hollow conducting rods can defeat both of these mechanisms and greatly increase the yield of subsurface ice—if needed to meet production rate requirements.

Another simple remedy that is feasible within the overall Thermal Mining architecture is to use the GPV to scrape away the dry layer of overburden as ice production tails off. The door into the Capture Tent described in Section 4.4 would enable this additional operation.

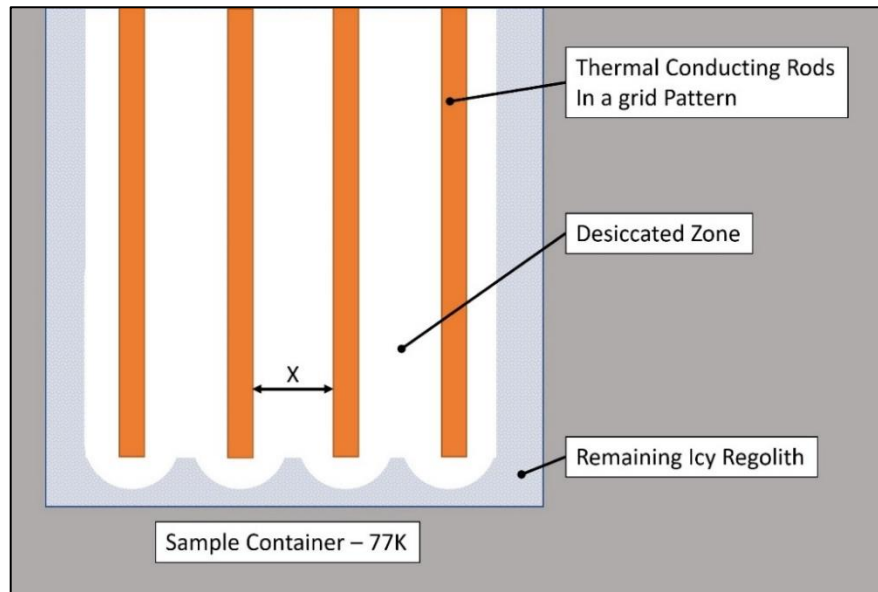


Figure 5.5.9. Side view thermal conducting rod grid layout.

6.0 Summary and Conclusions

6.1 Bulletized Summary

- The solar system is full of Thermal Mining targets, strategically located in the areas of most interest to human development of the solar system.
 - The Moon.
 - Mars.
 - Main asteroid belt.
 - Icy moons of Jupiter and Saturn.
- The Moon is the closest and most accessible Thermal Mining target.
 - A resource exploration campaign is required to confirm the presence of ice and quantify the resources as proven reserves.
- An architecture has been developed to produce propellant on the Moon from water ice extracted via Thermal Mining.
 - Details of the ice extraction system have been defined.
 - The concept of operations has been defined including launch and landing on the Moon.
 - Detailed mass and cost estimates have been developed.
 - A business case for a hypothetical propellant production company has been developed.
 - A public private partnership model delivers profits to the company and enormous savings to NASA.
- The efficiency of Thermal Mining and the minimal viable architecture approach delivers much lower cost than previous studies.
- Proof of concept testing has demonstrated surface heating is effective in sublimating surface ice and some subsurface ice.
 - Conducting rods significantly increase subsurface penetration and sublimation yields.
- Larger samples with improved boundary conditions required to make estimates of ice yields on the Moon.

6.2 Conclusions

Solar System Survey

The solar system is rich in bodies containing icy volatiles. These include some of the most desirable locations for human exploration and development.

Mars is rich in water ice, on the surface in the polar regions and in near surface deposits at lower latitudes. Carbon dioxide, CO₂, also exists frozen on the surface in the polar regions. Thermal mining of these deposits may provide early Mars explorers with a low-cost method of extracting water for human consumption, agriculture and rocket propellant. Water also makes superb radiation shielding for the long transit from Earth to Mars and back.

The dwarf planet Ceres appears to contain significant quantities of ice near the surface. Outgassing of water vapor from the surface of Ceres can be observed from Earth. This ice, extracted via Thermal Mining, makes Ceres an early candidate for a way station in the main asteroid belt as humans expand beyond Mars. Many main belt asteroids appear to be remnant comets composed of large fractions of water ice and other frozen volatiles. Examples include 24 Themis and 65 Cybele. The colonization of Ceres and ice mining of asteroids is a main theme of the science fiction series, *The Expanse*. Thermal Mining can make the fictional world of *The Expanse* a reality.

Beyond the asteroid belt, icy worlds become even more abundant. However, the illumination of the sun becomes much weaker. Solar Thermal Mining may still be feasible but could require enormous mirrors with large concentration ratios. This option may still be lower cost than other, likely nuclear, energy solutions.

Thermal Mining will likely prove to be the lowest cost method to extract valuable volatiles in the inner solar system for many decades to come. These commodities will enable human exploration and underpin a rapidly growing human economy in space.

Thermal Mining on the Moon

The closest source of icy volatiles beyond Earth is the Moon. Strategically located near the top of Earth's gravity well, the Moon is ideally situated to provide valuable resources for the very first push of humans into the inner solar system. Climbing out of the Moon's gravity well compared to Earth's is analogous to climbing a tall building versus Mount Everest. This energy advantage makes lunar sourced propellant an order of magnitude lower cost in high Earth orbit than propellant brought from Earth, even after taking account of the five hundred times higher cost to produce propellant on the Moon than Earth.

Current remote sensing data and the single LCROSS impact indicate volatiles exist at the lunar poles in quantities ranging from 1wt% to as high as 30wt%. These indications need to be confirmed via a comprehensive resource exploration campaign. If verified as a proven reserve, these quantities are sufficient to supply propellants and other commodities for centuries, fueling human exploration and development of the Moon, cislunar space and the transit to Mars. The use of lunar sourced propellant can save NASA over \$11B just to aggregate the required mass in cislunar space for a single Mars mission.

The Thermal Mining architecture for propellant production on the Moon can be considered the minimum viable architecture; it is the architecture that minimizes the total mass and cost to

create the first economically viable quantities of water and propellant. It targets surface and near subsurface ice, thus avoiding excavation, heavy equipment and dust creation. Use of reflected sunlight to provide heat and power avoids the energy conversion losses associated with power beaming. It is only after the surface ice is depleted that more expensive methods will be employed. But at that point, much more infrastructure will be in place (power, processing, transportation, etc.), mitigating the higher costs of excavation.

This situation is analogous to gold mining in the American west. The first miners were able to pick up gold nuggets from stream beds. This technique required very little capital (a mule and a pick, perhaps a gold pan) and very little labor (one miner). The result was a gold rush. But as the surface gold was depleted, methods were developed to power wash sediments or blast into hill sides to find the veins that sourced the stream-borne gold. Today, old mine tailings and slag beds are being reprocessed using advanced technology to get trace amounts of gold left behind by the technology of a century ago.

Thermal Mining is that first step for extracting water from the Moon. It provides a means to start resource development that is well within the capabilities of both private and public entities existing today. Once lunar propellant is available, transportation costs to cislunar space and the Moon will collapse, bringing more activity, stimulating more demand for propellant, stimulating competition and innovation, and lowering costs still further. This is the virtuous cycle of the free market and it will lead to the creation of a vibrant economy in cislunar space that delivers trillions of dollars in new wealth into the human sphere.

Proof of Concept Testing

The most significant technical risk to the development of a Thermal Mining system is the effectiveness of surface heating in sublimating ice on the surface and within the near subsurface. This risk has been substantially mitigated by nearly fifty tests conducted in the CSM medium vacuum chamber under cryogenic conditions.

We have created a unique set of icy regolith simulants more representative of the actual conditions on the Moon than any to date. The ice at the poles of the Moon was likely deposited in one or more impact or volcanic events in the ancient past. It was subsequently subjected to billions of years of impacts shattering the rock into regolith and mixing the ice and regolith. During these processes, the water was only ever in vapor or frozen states, never liquid. Our simulants were thus dry mixes of ice grains and regolith grains.

We subjected this icy regolith mixture to surface heat, varying the ice percentage and the boundary conditions. We also created samples of pure ice over regolith and explored the effectiveness of hollow, perforated conducting rods embedded into the surface.

Surface ice is sublimated rapidly, in a matter of hours, and does not migrate into the regolith under heating. This is an important and favorable result. *Surface ice will be quickly extracted by the Thermal Mining method.*

The situation regarding subsurface ice is more complex. Ice is quickly extracted from the first few centimeters of icy regolith, but then the process slows due to several mechanisms. First, the desiccated surface layer of regolith acts as an insulator, shielding lower layers from further heating. Second, the desiccated layer acts as a vapor barrier, prohibiting sublimated vapor from escaping to the surface. This vapor then refreezes, forming a heat affected layer. However, vapor

does not appear to migrate to lower levels in the sample. Third, the small size of our sample places a cold wall at liquid nitrogen temperature very close to the heat source.

The first two effects can be mitigated by the incorporation of a perforated, hollow conducting rod. This device increased ice extraction rates by two to three times in the Block 1 test configuration. Another approach could be to scrape of the desiccated overburden. The third effect can only be eliminated by testing larger samples with the cold wall far from the heat source, better approximating the situation that would exist on the Moon. The total amount of ice extracted from such larger samples will necessarily be larger than seen in our initial tests.

Significant quantities of ice can be extracted from the top layers of icy regolith mixtures by surface heating alone, likely to depths of tens of centimeters over the dwell times assumed in our Thermal Mining point design. Depending on the ice concentration and the amount of surface ice, this may be sufficient to meet the production rates assumed in our architecture. Under conditions of lower ice concentration and less surface ice, conducting rods can be employed. At any particular lunar site, these conditions must be determined by a robust exploration campaign.

In either case, we have demonstrated that Thermal Mining can extract economically viable quantities of ice from the Moon.

6.3 Recommendations for Future Work

As the development of the Thermal Mining system progresses, good systems engineering practices will guide the activities. Early in development, as we are with Thermal Mining, risk management plays a critical role. Hence, our recommendations for future directions of this work are driven by a detailed risk assessment of the overall architecture and the lunar mining mission context. Table 6.1 lists the current risks, ranked according to overall severity, our assessment of probability and consequences and a brief description of the next steps to mitigate the risk. As shown in Figure 6.1, the probability of occurrence and consequences are scored on a scale of 1 to 5. The overall risk severity is the product of the two scores.

Table 6.1. Top Thermal Mining Risks.

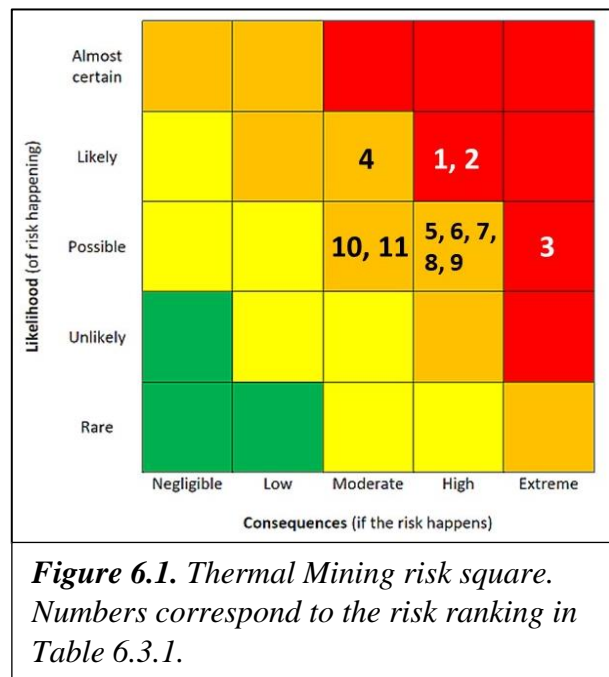
Rank	Risk description	Prob.	Cons.	Sev.	Mitigation
1	Business case can't close	4	4	16	Further business case analysis
2	System can't last 10 years	4	4	16	Maintainability analysis
3	Insufficient ice on the Moon	3	5	15	Addressed by resource exploration campaign
4	Thermal Mining cannot produce adequate ice	3	4	12	Block 2 testing
5	Simulants are inadequate	4	3	12	Need ground truth on Moon
6	Vapor cannot be captured	3	4	12	Block 3 testing
7	Ice extraction system mobility	3	4	12	Preliminary design, analysis
8	Lunar environments	3	4	12	Preliminary design, analysis
9	Launch, landing, set up	3	4	12	Preliminary design, analysis
10	Contaminants in ice	3	3	9	Being worked in ongoing NASA STMD study
11	Vehicle power/storage	3	3	9	Preliminary design, analysis

Risk 1 can be addressed by further refinements of the business case analysis. Key areas of refinement are the cost estimates and the markets. Development of the details of a PPP would also be important. Risks 2, 7, 8, 9, and 11 can be addressed by developing a preliminary design of the ice extraction system, accompanied by more detailed systems analysis. Risks 4 and 6 are addressed by Block 2 and Block 3 testing respectively. Block 3 testing, discussed below, is an extension of Block 2 testing to even larger samples and includes vapor capture and refreezing. Risks 3 and 5 can only be addressed by resource exploration missions to the lunar PSRs, a very high priority in proving the viability of lunar propellant production. A workshop conducted at the CSM in the summer of 2018 developed a roadmap for this “prospecting” campaign that could lead to industrial scale production of propellant from lunar water within 10 years [Sowers & Morris, 2018]. See Figure 4.0.2. Finally, risk 10 is being actively worked by Paragon Space Development Corporation (Paragon) as part of NASA’s NextSTEP-2 program.

Next steps in the refinement of the Thermal Mining architecture should be to develop a detailed design (to Preliminary Design Review level of maturity) of the ice extraction system and its three components: the capture tent, the secondary optics and the cold trap/ice hauler, culminating in a PDR-like review.

The design activities should be supported by ongoing systems analysis. These analyses should include operations analysis, mass properties, launch & landing, and thermodynamics and mass transport. The operations analysis should focus on requirements associated with Reliability, Availability and Maintainability (RAM) to ensure we can achieve the required 10-year life time and to develop logistics (spare parts) and maintenance plans. Mass properties analysis would produce an updated set of mass estimates for the entire system to support launch and landing analysis and an updated cost assessment. Launch and landing analysis should be expanded from the initial deployment sequence based on ULA launchers and the XEUS lander to include other potential launch providers and to examine lander capabilities under development for CLPS and Artemis. Finally, thermodynamic and mass transport analysis would model vapor sublimation (anchored to our test data), mass transport into the cold traps and subsequent freezing.

As more detail on the overall system becomes defined, either by our own work or complementary efforts (e.g. NextSTEP), the cost model and program timelines should be updated. These will feed into an updated business case analysis. Business and financial experts should be engaged. These efforts should include each of the major entities required to commercialize the Thermal Mining technology: the system developer/manufacturer, the system operator, the



customer and the financier. The product of this analysis would be a commercialization path and timeline that can be used to generate interest and investment.

Another necessary near-term step is to expand the proof of concept testing. Most of our testing in Phase I was conducted using our Block 1 test apparatus (Section 5.3). Being limited in size and having the liquid nitrogen boundary within a few centimeters of the heat source, sublimation rates and amounts were less than what we would expect under full scale conditions on the Moon. In other words, much of our heat was expended boiling nitrogen, not sublimating ice. The Block 2 test apparatus was designed to improve that situation by moving the cold boundary farther away from the lamp. The Block 2 apparatus is currently in fabrication.

Block 2 testing will vary ice content, regolith grain size distribution, compaction, and explore various configurations of conducting rods and straws. This testing should also explore creating icy regolith simulant via vapor deposition and examine the possibility of introducing volatile contaminants seen in the LCROSS data (Table 4.0.1).

Both Block 1 and Block 2 testing address program risk 4: can we sublimate enough ice? Block 3 testing includes the vapor capture part of the system, represented by program risk 6: can we capture sufficient vapor? Block 3 testing would develop a new apparatus, allowing us to capture the vapor released from the simulant in a cold trap analogous to the full-scale system. This testing would use CSM's large vacuum chamber shown in Figure 6.2. Figure 6.3.3 shows a schematic of the Block 3 apparatus. The sample and heating configuration is similar to Block 2, but scaled up to take advantage of the larger vacuum chamber. In addition, there is a cover over the sample with a passage to a cold trap to simulate the capture tent and cold trap components of the ice extraction system.

To complement our test program, physics-based models of the thermodynamic processes occurring within samples should be constructed. The complexity of these processes was one of the surprises of the Phase I investigation. Beyond creating a desiccated layer of regolith by sublimating the ice, heat affected zones are formed where the ice has been sublimated but then refrozen



Figure 6.2. The large (2.7 m³) cryogenic vacuum chamber at CSM.

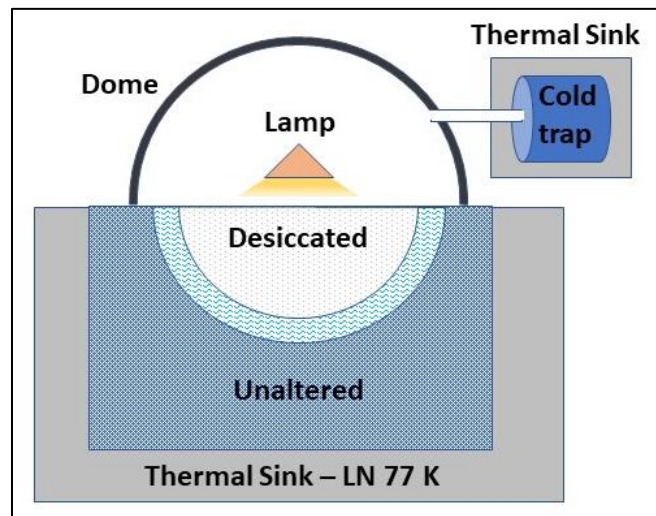


Figure 6.3. Block 3 test apparatus. schematic.

in place. However, these zones show little ice enrichment; i.e., most of the refrozen ice is not being driven down from higher in the sample, but is the ice previously present, just in a different state. Understanding these phenomena through modeling will greatly enhance the ability to optimize the Thermal Mining system. Finally, the lunar ice formation and evolution simulation effort begun under Phase I (Section 4.1) should be continued. As shown in Figure 4.1.2, this modeling provides insight into the origin, nature and abundance of lunar polar ice, critical to assessing the viability of Thermal Mining on the Moon.

7.0 References

- Abu-Hamdeh, N. H. (2003). Thermal properties of soils as affected by density and water content. *Biosystems Engineering*, 86(1), 97–102. [https://doi.org/10.1016/S1537-5110\(03\)00112-0](https://doi.org/10.1016/S1537-5110(03)00112-0)
- Ahmad, N. (1994). Thermal Conductivity of Ice, Water and Steam. *Physical Status Solidi*, 37(78039), 37–44.
- Andreas, E. L. (2007). New estimates for the sublimation rate for ice on the Moon. *Icarus*. <https://doi.org/10.1016/j.icarus.2006.08.024>
- Arnold, J.R., Ice in the Lunar polar regions, *Journal of Geophysical Research* (1979) **84**, 5659-5668, <https://doi.org/10.1029/JB084iB10p05659>
- Arnold, J. R. (1975). Monte Carlo Simulation of Turnover Processes in the Lunar Regolith, 6th Lunar Science Conference.
- Batir, J. F., Hornbach, M. J., & Blackwell, D. D. (2017). Ten years of measurements and modeling of soil temperature changes and their effects on permafrost in Northwestern Alaska. *Global and Planetary Change*. <https://doi.org/10.1016/j.gloplacha.2016.11.009>
- Benna, M., Hurley, D., Stubbs, T., Mahaffy, P., Elphic, R., (2019). Lunar soil hydration constrained by exospheric water liberated by meteoroid impacts. *Nature Geoscience* 12.
- Cannon, K. M., and D. T. Britt, (2020). A Geologic Model for Lunar Ice Deposits at Mining Scales. *Icarus*, under revision.
- Centers, Ross, David Dickson and Joshua Schertz, (2018). "Power Beaming for Rovers in Permanently Shadowed Regions." Space Resources Roundtable XX / Planetary & Terrestrial Mining Sciences Symposium, Golden, CO, June 11-13.
- Charania, A.C., DePasquale, D., (2007) "Economic Analysis of a Lunar ISRU Propellant Services Market," IAC Paper 07-A5.1.03.
- Colaprete, A., Schultz, P., Heldmann, J., Wooden, D., Shirley, M., Ennico, K., Hermalyn, B., Marshall, W., Riccio, A., Elphic, R.C., Goldstein, D., Summy, D., Bart, G.D., Asphaug, E., Korycansky, D., Landis, D., Sollitt, L., Detection of Water in the LCROSS Ejects Plume, *Science* (2010) **330**, 463-468.
- Colaprete A., Elphic, R., Heldmann, J., Ennico, K., An Overview of the Lunar Crater Observation and Sensing Satellite (LCROSS), *Space Sci. Rev.* (2012) **167**, 3-22.
- Cowen, R. (2009, October 8). Ice Confirmed On An Asteroid / Science News. Retrieved from https://web.archive.org/web/20091012075224/www.sciencenews.org/view/generic/id/48174/title/Ice_confirmed_on_an_asteroid
- Crider, D.H., Vondrak, R.R. 2000. The solar wind as a possible source of lunar polar hydrogen deposits. *J. Geophys. Res.* 105, 26,773-26,782.

- CRIRSCO, Committee for Mineral Reserves International Reporting Standards, Standard Definitions, 2012.
http://www.crisco.com/news_items/CRIRSCO_standard_definitions_oct2012.pdf
- Dickson, David, Sowers, G. (2019). "Modeling Long Term Deposition of Ice in Lunar Permanently Shadowed Regions (PSRs) for the Purposes of Resource Prospecting," Proceedings of the 70th Annual International Astronautical Congress, Washington, DC.
- Dreyer, C., Sowers, G. & Williams, H., (2018). *Ice Mining in Lunar Permanently Shadowed Regions*. Presentation at 19th Space Resources Roundtable.
https://isruinfo.com/public/docs/srr19_ptmss/7-13%20Ice%20Mining%20in%20Lunar%20Permanently%20Shadowed%20Regions-Dreyer.zip
- Dundas, C. M., Bramson, A. M., Ojha, L., Wray, J. J., Mellon, M. T., Byrne, S., ... Holt, J. W. (2018). Exposed subsurface ice sheets in the Martian mid-latitudes. *Science*, 359(6372), 199-201. doi:10.1126/science.aao1619
- Elphic, R.C., Eke, V.R., Teodoro L.F.A., Lawrence, D.J., Bussey D.B.J, Models of the distribution and abundance of hydrogen at the Lunar south pole. *GRL* (2007) **34**, doi:10.1029/2007GL029954
- Enright, John, and Kieran A. Carroll. "Laser Power Beaming for lunar pole exploration." SPS'97 (1997).
- FAA, (2018). The Annual Compendium of Commercial Space Transportation.
https://www.faa.gov/about/office_org/headquarters_offices/ast/media/2018_ast_compendium.pdf
- Farrell, W.M., Hurley, D.M., Poston, M.J., Hayne, P.O., Szalay, J.R., McLain, J.L. (2019). The Young Age of the LAMP-observed Frost in Lunar Polar Cold Traps. *Geophys. Res. Lett.* 46, 8680-8688.
- Feldman, W.C., Maurice, S., Binder, A.B, Barraclough, B.L., Elphic, R.C., Lawrence, D.J., (1998). Fluxes of fast and epithermal neutrons from Lunar prospector: Evidence for water ice at the Lunar poles. *Science* **281**, 1496-1500.
- Feistel, R., Wagner, W., Sublimation pressure and sublimation enthalpy of H₂O ice In between 0 and 273.16 K, *Geochimica et Cosmochimica*, 71 (2007) 36-45.
- Flahaut, J., Carpenter, J., Williams, J. P., Anand, M., Crawford, I. A., van Westrenen, W., ... & Zhao, S. (2020). Regions of interest (ROI) for future exploration missions to the lunar South Pole. *Planetary and Space Science*, 180, 104750.
- Filacchione, G., De Sanctis, M., Capaccioni, F. et al. Exposed water ice on the nucleus of comet 67P/Churyumov–Gerasimenko. *Nature* 529, 368–372 (2016).
<https://doi.org/10.1038/nature16190>
- Fisher, E.S., Lucey, P.G., Lemelin, M., Greenhagen, B.T., Zuber, M.T., Evidence for surface water ice in the Lunar polar regions using reflectance measurements from the Lunar

- Orbiter Laser Altimeter and temperature measurements from the Diviner Lunar Radiometer Experiment, *Icarus* (2017) **292**, 74-85.
- Foster Wheeler Environmental Corporation & Battelle Corporation, Overview of Thermal Desorption Technology, 1998. https://clu-in.org/download/contaminantfocus/dnapl/Treatment_Technologies/NFESC-CR-98-008-ENV.pdf
- Frequently asked questions. (n.d.). Retrieved from https://www.esa.int/Science_Exploration/Space_Science/Rosetta/Frequently_asked_questions
- Gertsch, Leslie S.; Rostami, Jamal; and Gustafson, Robert, "Review of Lunar Regolith Properties for Design of Low Power Lunar Excavators" (2008). International Conference on Case Histories in Geotechnical Engineering. 2. <http://scholarsmine.mst.edu/icchge/6icchge/session10/2>
- Gladstone, G. R., et al., "LRO-LAMP Observations of the LCROSS Impact Plume," *Science* 330, 472 (2010); doi: 10.1126/science.1186474
- Gläser, P., et al. "Illumination conditions at the lunar poles: Implications for future exploration." *Planetary and Space Science* 162 (2018): 170-178.
- Grima, C., Kofman, W., Mouginot, J., Phillips, R. J., Hérique, A., Biccari, D., ... Cutigni, M. (2009). North polar deposits of Mars: Extreme purity of the water ice. *Geophysical Research Letters*, 36(3), n/a-n/a. doi:10.1029/2008gl036326
- Hayne, P.O., Hendrix, A., Sefton-Nash, E., Siegler, M.A., Paige, D.A., Evidence for exposed water ice in the Moon's south polar regions from Lunar Reconnaissance Orbiter ultraviolet albedo and temperature measurements. *Icarus* (2015) **255**, 58-69
- Hurley, D. M. et al., Two-Dimensional Distribution of Volatiles in the Lunar Regolith from Space Weathering Simulations, *Geophys. Res. Lett.*, 39 (2012).
- Jewitt, D., & Guilbert-Lepoutre, A. (2011). LIMITS TO ICE ON ASTEROIDS (24) THEMIS AND (65) CYBELE. *The Astronomical Journal*, 143(1), 21. doi:10.1088/0004-6256/143/1/21
- Jones, C., et al., "Cost Breakeven Analysis of Cis-lunar ISRU for Propellant," AIAA-2019-1372, SciTech Forum 2019.
- Jones, C., (2019). Private correspondence via email. February 4, 2019.
- Kleinhenz, J., Linne, D., (2013). Preparation of a Frozen Regolith Simulant Bed for ISRU Component Testing in a Vacuum Chamber. NASA/TM—2013-217833.
- Kornuta, D., Abbud-Madrid, A., Atkinson, J., Barr, J., Barnhard, G., Bienhoff, D., Blair, B., Clark, V., Cyrus, J., DeWitt, B., Dreyer, C., Finger, B., Goff, J., Ho, K., Kelsey, L., Kervala, J., Kutter, B., Metzger, P., Montgomery, L., Morrison, P., Neal, C., Otto, E., Roesler, G., Schier, J., Seifert, B., Sowers, G., Spudis, P., Sundahl, M., Zacny, K., Zhu,

- G. 2019. Commercial lunar propellant architecture: A collaborative study of lunar propellant production. REACH 13, 100026.
- Küppers, M., O'Rourke, L., Bockelée-Morvan, D. et al. Localized sources of water vapour on the dwarf planet (1) Ceres. *Nature* 505, 525–527 (2014).
<https://doi.org/10.1038/nature12918>
- LaMarche, C. Q., Curtis, J. S., & Metzger, P. T. (2011). Permeability of JSC-1A: A lunar soil simulant. *Icarus*, 212(1), 383–389. <https://doi.org/10.1016/j.icarus.2010.12.015>
- Lang, Kenneth (2011). *The Cambridge Guide to the Solar System*. Cambridge University Press. pp. 372, 442.
- Lawrence, D. J., Feldman, W. C., Goldsten, J. O., Maurice, S., Peplowski, P. N., Anderson, B. J., ... Weider, S. Z. (2012). Evidence for Water Ice Near Mercury's North Pole from MESSENGER Neutron Spectrometer Measurements. *Science*, 339(6117), 292-296. doi:10.1126/science.1229953
- Lawrence, D.J., Feldman, W.C., Elphic, R.C., Hagerty, J.J., Maurice, S., McKinney, G.W., Prettyman, T.H. Improved modelling of Lunar Prospector neutron spectrometer data: Implications for hydrogen deposits at the Lunar poles. *JGR* (2006) **111**, E8, doi:10.1029/2005JE002637
- Li, S, Lucey, P.G., Milliken, R.E., Hayne, P.O., Fisher, E., Williams, J.P., Hurley, D.M., Elphic, R.C., Direct evidence of surface exposed water ice in the lunar polar regions. *PNAS* (2018). <https://doi.org/10.1073/pnas.1802345115>
- Licandro, J., H. Campins, M. Kelley, K. Hargrove, N. Pinilla-Alonso, D. Cruikshank, A. S. Rivkin and J. Emery(65) Cybele: detection of small silicate grains, water-ice, and organics. *A&A*, 525 (2011) A34 DOI: <https://doi.org/10.1051/0004-6361/201015339>
- List Of Jupiter Trojans. (2020, February 17). Retrieved from <https://minorplanetcenter.net/iau/lists/JupiterTrojans.html>
- Lucey, P.G., Neumann, G.A., Riner, M.A., Mazarico, E., Smith, D.E., Zuber, M.T., Paige, D.A., Bussey, D.B., Cahill, J.T., McGovern, A., Isaacson, P., Corley, L.M., Torrence, M.H., Melosh, H.J., Head, J.W., Song, E., The global albedo of the Moon at 1064 nm from LOLA *JGR* (2014) **119**, Issue 7
- Marburger, J., (2006). Keynote address to the 44th Goddard Symposium.
https://www.nasa.gov/pdf/376587main_02%20-%2003-15-06%20jhm%20Goddard%20Symp.pdf
- Mazarico, E., Genova, A., Goossens, S., Lemoine, F. G., Neumann, G. A., Zuber, M. T., ... Solomon, S. C. (2014). The gravity field, orientation, and ephemeris of Mercury from MESSENGER observations after three years in orbit. *Journal of Geophysical Research: Planets*, 119(12), 2417-2436. doi:10.1002/2014je004675

- McCord, T. B., Hansen, G. B., Clark, R. N., Martin, P. D., Hibbitts, C. A., Fanale, F. P., ... Danielson, G. E. (1998). Non-water-ice constituents in the surface material of the icy Galilean satellites from the Galileo near-infrared mapping spectrometer investigation. *Journal of Geophysical Research: Planets*, 103(E4), 8603-8626. doi:10.1029/98je00788
- McVay, E., Jones, C., Merrill, R., (2016). Cis-Lunar Reusable In-Space Transportation Architecture for the Evolvable Mars Campaign. AIAA Space Forum. Long Beach, CA.
- Mitrofanov, I., Litvak, M., Sanin, A., Malakhov, A., Golovin, D., Boynton, W., Droege, G., Chin, G., Evans, L., Harshman, K., Fedosov, F., Garvin, J., Kozyrev, A., McClanahan, T., Milikh, G., Mokrousov, M., Starr, R., Sagdeev, R., Shevchenko, V., Shvetsov, V., Tert'yakov, V., Trombka, J., Varenikov, A., Vostrukhin, A., Testing polar spots of water-rich permafrost on the Moon: LEND observations onboard LRO *JGR* (2012) **117**, Issue E12, doi:10.1029/2011JE003956
- Morrison, C., (2020). Ultra Safe Nuclear Corporation. Seminar at the Colorado School of Mines, Golden Colorado.
- Needham, D.H., Kring, D.A. 2017. Lunar volcanism produced a transient atmosphere around the ancient Moon. *Earth Planet. Sci. Lett.* 478, 175-178.
- Needham, D.H., Siegler, M., Li, S., Kring, D. 2019. Calculated Thicknesses of Volcanically Derived Water Ice Deposits at the Lunar Poles. 50th Lunar Planet. Sci. Conf., Abstract #1087.
- Nozette, S., Lichtenberg, C.L., Spudis, P., Bonner, R., Ort, W., Malaret, E., Robinson, M., Shoemaker, E.M., The Clementine Bistatic Radar Experiment *Science* (1998) **274**, 1495-1498
- Nozette, S., Spudis, P.D., Robinson, M.S., Bussey, D.B.J., Lichtenberg, C., Bonner, R., Integration of Lunar polar remote-sensing data sets: Evidence for ice at the Lunar south pole. *JGR* (2001) **106**, Issue E10
- Ong et al. 2010: <https://www.sciencedirect.com/science/article/pii/S0019103509005016>
- Overview | Dawn – NASA Solar System Exploration. (n.d.). Retrieved from <https://solarsystem.nasa.gov/missions/dawn/overview/>
- Patterson, G.W., Stickle, A.M., Turner, F.S., Jensen, J.R., Bussey, D.B.J, Spudis, P., Espiritu, R.C., Schulze, R.C., Yocky, D.A., Wahl, D.E., Zimmerman, M., Cahill, J.T.S., Nolan, M., Carter, L., Neish, C.D., Raney, R.K., Thomson, B.J., Kirk, R., Thompson, T.W., Tise, B.L., Erteza, I.A., Jakowatz, C.V., Bistatic radar observations of the Moon using Mini-RF on LRO and the Arecibo Observatory, *Icarus* (2017) **283**, 2-19
- Pätzold, M., Andert, T., Hahn, M. et al. A homogeneous nucleus for comet 67P/Churyumov–Gerasimenko from its gravity field. *Nature* 530, 63–65 (2016). <https://doi.org/10.1038/nature16535>

- Petersen, E. I., Holt, J. W., & Levy, J. S. (2018). High Ice Purity of Martian Lobate Debris Aprons at the Regional Scale: Evidence From an Orbital Radar Sounding Survey in Deuteronilus and Protonilus Mensae. *Geophysical Research Letters*, 45(21), 11,595-11,604. doi:10.1029/2018gl079759
- Philae settles in dust-covered ice. (2015, January 6). Retrieved from <https://blogs.esa.int/rosetta/2014/11/18/philae-settles-in-dust-covered-ice/>
- Prem et al. 2015: <https://www.sciencedirect.com/science/article/pii/S0019103514005569>
- Rivkin, A., Emery, J. Detection of ice and organics on an asteroidal surface. *Nature* 464, 1322–1323 (2010). <https://doi.org/10.1038/nature09028>
- Sanin, A. B., Mitrofanov, I. G., Litvak, M. L., Bakhtin, B. N., Bodnarik, J. G., Boynton, W. V., Chin, G., Evans, L.G., Harshman, K., Fedosov, F., Golovin, D.V., Kozyrev, A.S., Livengood, T.A., Malakhov, A.V., McClanahan, T.P., Mokrousov, M.I., R.D., Starr, Sagdeev, R.Z., Tret'yakov, V.I., Vostrukhin, A. A., Hydrogen distribution in the lunar polar regions. *Icarus*, (2017)283, 20-30. DOI: 10.1016/j.icarus.2016.06.002 Sanin et al. (2017) *Icarus* **283**, 20-30
- Schiller, G. (2016). Innovation at ULA. AIAA Space 2016. [https://ula.bsshost.me/docs/default-source/evolution/innovation-at-ula-\(aiaa-space-2016\).pdf](https://ula.bsshost.me/docs/default-source/evolution/innovation-at-ula-(aiaa-space-2016).pdf)
- Schorghofer & Taylor 2007: <https://agupubs.onlinelibrary.wiley.com/doi/full/10.1029/2006JE002779>
- Schorghofer & Aharonson 2014: <https://iopscience.iop.org/article/10.1088/0004-637X/788/2/169/meta>
- Scott, E., Rodel, P., Thrift, B., (2019). Concepts for an In-Situ, Reusable Construction System for Lunar Landing and Launch Pads. Space Resources Roundtable, Golden, Colorado. https://isruinfo.com/public/docs/srr20_ptmss/6-7%20ISR%20Construction%20of%20Launch%20and%20Landing%20Pads-Scott.zip
- Shearer, C., 2011. LEAG letter to NASA Headquarters. <https://www.lpi.usra.edu/leag/reports/RoboticAnalysisLetter.pdf>
- Sheppard, S. S., Williams, G. V., Tholen, D. J., Trujillo, C. A., Brozovic, M., Thirouin, A., Devogele, M., Fohring, D., Jacobson, R., Moskovitz, N. A. (2018). New Jupiter Satellites and Moon-Moon Collisions. *Research Notes of the AAS*, 2(3), 155. doi:10.3847/2515-5172/aadd15
- Shishko, R., (2019). A Comparison of Previously Published Papers on the Economics of Lunar In Situ Resource Utilization (ISRU). JPL internal report.
- Siegler, M.A., Miller, R.S., Keane, J.T., Laneuville, M., Paige, D.A., Matsuyama, I., Lawrence, D.J., Crotts, A., Poston, M.J. 2016. Lunar true polar wander inferred from polar hydrogen. *Nature* 531, 480-484.

- Sommariva, A., Gori, L., Chizzolini, B., Pianorsi, M., (2020). The Economics of Moon Mining. *Acta Astronautica*. Accepted for publication.
- Sommariva, A., Gori, L., Chizzolini, B., Pianorsi, M., (2019). The Economics of Moon Mining. 11th IAA Symposium on the Future of Space Exploration. Torino, Italy.
- Sori, M.M., Sizemore, H.G., Byrne, S. et al. Cryovolcanic rates on Ceres revealed by topography. *Nat Astron* 2, 946–950 (2018). <https://doi.org/10.1038/s41550-018-0574-1>
- Sowers, G., Dreyer, C., Ice Mining in Lunar Permanently Shadowed Regions. 2019. *New Space* Vol. 7 #4. <https://doi.org/10.1089/space.2019.0002>
- Sowers, G, Morris, G. Lunar Polar Prospecting Workshop: Findings and Recommendations. 2018. http://isruinfo.com/docs/LPP_2018_final_report.pdf
- Sowers, G., 2018, *A Business Case for Mining Propellant on the Moon*, Presentation at 19th Space Resources Roundtable https://isruinfo.com/public/docs/srr19_ptmss/2-2%20Business%20Case%20for%20Mining%20Propellant%20on%20the%20Moon-Sowers.zip
- Sowers, G., A cislunar transportation system fueled by lunar resources, *Space Policy*, (2016) 37, 103-109
- SPD-1, (2017). Space Policy Directive 1. Presidential Memorandum on Reinvigorating America’s Human Space Exploration Program. <https://www.whitehouse.gov/presidential-actions/presidential-memorandum-reinvigorating-americas-human-space-exploration-program/>
- Spohn, T., Breuer, D., & Johnson, T. (2014). *Encyclopedia of the Solar System* (3rd ed.). Amsterdam, Netherlands: Elsevier.
- Stoica, A, Wilcox, B, Alkalai, L, Ingham, M, Quadrelli, M, Salazar, R., Mantovani, J., Henrickson, J., Valasek, J., Sercel, J., (2017). TransFormers for Lunar Extreme Environments: Ensuring Long-Term Operations in Regions of Darkness and Low Temperatures. NIAC Phase II Final Report.
- Stoica, A, Mantovani, J, Wilcox, B, Alkalai, L, Ingham, M, Quadrelli, M, Tamppari, L, Mitchell, K. TransFormers for ensuring long-term operations in lunar extreme environments. 2016. http://isruinfo.com/docs/srr17_ptmss/37-TransFormers%20for%20Long-Term%20Operations%20in%20Lunar%20Extreme%20Environments-Mantovani.zip
- Spudis, P.D., Bussey, D.B.J., Baloga, S.M., Cahil, J.T.S. Glaze, L.S., Patterson, G.W., Raney, R.K., Thompson, T.W., Thomson, B.J., Ustinov, E.A., Evidence of water ice on the Moon : Results from anomalous polar craters from the LRO Mini-RF imaging radar *JGR:Planets* (2013) **118**, Issue 10
- Tajeddine, R., et al. "Constraints on Mimas' interior from Cassini ISS libration measurements." *Science*, vol. 346, no. 6207, 2014, pp. 322-324.

- Tavman, I. H. (1996). Effective thermal conductivity of granular porous materials. *International Communications in Heat and Mass Transfer*, Vol. 23, pp. 169–176.
[https://doi.org/10.1016/0735-1933\(96\)00003-6](https://doi.org/10.1016/0735-1933(96)00003-6)
- Thomas, P., Armstrong, J., Asmar, S. et al. Hyperion's sponge-like appearance. *Nature* 448, 50–53 (2007). <https://doi.org/10.1038/nature05779>
- Titus, T. N. (2003). Exposed Water Ice Discovered near the South Pole of Mars. *Science*, 299(5609), 1048-1051. doi:10.1126/science.1080497
- Tobie, G., Harel, L., Kalousova, K., Kverka, J., Behoukova, M., Bollengier, O., Brown, J.M., Cadek, O., Choblet, G., Dumoulin, C., Grasset, O., Journaux, B., Postberg, F., Sotin, C., Soucek, O., Vance, S. Core-ocean-ice exchange processes in Europa, Ganymede and Callisto. European Planetary Science Congress 2018. Berlin, Germany.
- Ulamec, S., Biele, J., & Trollope, E. (2010). How to survive a Lunar night. *Planetary and Space Science*. <https://doi.org/10.1016/j.pss.2010.09.024>
- Vondrak, R.R., Crider D.H. Ice at the Lunar Poles, *American Scientist*, 91 (2003) 322-29.
- Watson, K., Murray, B.C., Brown, H., The behavior of volatiles on the Lunar surface *JGR* (1961) **66**, Issue 9
- Yoshida, F., & Nakamura, T. (2005). Size Distribution of Faint Jovian L4 Trojan Asteroids. *The Astronomical Journal*, 130(6), 2900-2911. doi:10.1086/497571
- Zhu, C., Crandall, P. B., Gillis-Davis, J. J., Ishii, H. A., Bradley, J. P., Corley, L. M., Kaiser, R. I., (2019). Untangling the formation and liberation of water in the lunar regolith. *Proceedings of the National Academy of Sciences*, 116 (23) 11165-11170; DOI: 10.1073/pnas.1819600116

8.0 Appendix A: Solar System Catalogue

This appendix contains detailed data on some of the solar system bodies contained in our survey. This data is useful as a reference to begin resource utilization planning.

	Mean Distance from Planet (km)	Mean Diameter (km)	Eccentricity	Semi-Major Axis (km) around Parent Planet or Sun	Periapsis of Orbit around Parent Planet or Sun (km)	Apoapsis of Orbit around Parent Planet or Sun (km)
Earth's Moon	384,400	3,574	0.05490	384,400	362,600	405,400
Mercury	N/A	4,880	0.20563	57,909,050	46,001,200	69,816,900
Mars	N/A	6,779	0.09340	227,939,200	206,700,000	249,200,000
Comet 67P	N/A	4	0.65058	518,320,000	186,290,000	850,340,000
Asteroid 24 Themis	N/A	198	0.12442	469,050,000	410,690,000	527,410,000
Asteroid & Dwarf Planet Ceres	N/A	939	0.07601	414,260,000	382,770,000	445,750,000
Asteroid 65 Cybele	N/A	237	0.11205	512,350,000	454,940,000	569,760,000
Jupiter's Ganymede	1,070,000	5,268	0.00130	1,070,400	1,069,200	1,071,600
Jupiter's Callisto	1,883,000	5,021	0.00740	1,882,700	1,869,000	1,897,000
Jupiter's Io	421,600	3,643	0.00410	421,700	420,000	423,400
Jupiter's Europa	670,900	3,121	0.00900	670,900	664,862	676,938
Saturn's Titan	1,221,850	5,149	0.02880	1,221,870	1,186,680	1,257,060
Saturn's Rhea	527,040	1,528	0.00100	527,070	526,543	527,597
Saturn's Iapetus	3,561,300	1,469	0.02830	3,560,840	3,460,068	3,661,612
Saturn's Dione	377,400	1,123	0.00220	377,420	376,590	378,250
Saturn's Tethys	294,660	1,062	0.00010	294,619	294,590	294,648
Saturn's Enceladus	238,020	504	0.00470	237,948	236,830	239,066
Saturn's Mimas	185,520	396	0.01960	185,539	181,902	189,176
Saturn's Phoebe	12,952,000	213	0.16400	12,944,000	10,832,224	15,063,602
Saturn's Hyperion	1,481,000	270	0.10420	1,481,100	1,466,112	1,535,756
Uranus's Titania	435,840	1,578	0.00110	435,910	435,430	436,390
Uranus's Oberon	582,600	1,523	0.00140	583,520	582,703	584,337
Uranus's Ariel	191,240	1,158	0.00120	191,020	190,791	191,249
Uranus's Umbriel	265,970	1,169	0.00390	266,000	264,963	267,037
Uranus's Miranda	129,780	472	0.00130	129,390	129,222	129,558
Neptune's Triton	354,800	2,707	0.00002	354,759	354,753	354,765
Neptune's Proteus	117,600	420	0.00053	117,647	117,585	117,709
Neptune's Nereid	5,513,400	340	0.75070	5,513,787	1,374,587	9,652,987
Dwarf Planet Pluto	N/A	2,377	0.24880	5,906,380,000	30	49
Pluto's Charon	19,571	1,212	0.00020	19,591	19,595	19,587

	Mass (kg)	Escape Velocity (km/s)	Surface Gravity (m/s ²)	Temp Low (K)	Temp High (K)
Earth's Moon	7.34E+22	2.380	1.620	35	373
Mercury	3.30E+23	4.250	3.700	100	700
Mars	6.42E+23	5.027	3.720	120	293
Comet 67P	9.98E+12	0.001	0.001	180	230
Asteroid 24 Themis	2.30E+19	0.087	0.150	115	160
Asteroid & Dwarf Planet Ceres	9.39E+20	0.510	0.280	110	155
Asteroid 65 Cybele	1.78E+19	0.146	0.070	125	170
Jupiter's Ganymede	1.48E+23	2.741	1.428	80	160
Jupiter's Callisto	1.08E+23	2.440	1.235	80	165
Jupiter's Io	8.93E+22	2.558	1.796	143	1922
Jupiter's Europa	4.80E+22	2.025	1.314	50	125
Saturn's Titan	1.35E+23	2.639	1.352	93	258
Saturn's Rhea	2.31E+21	0.635	0.264	53	99
Saturn's Iapetus	1.81E+21	0.573	0.223	90	130
Saturn's Dione	1.10E+21	0.510	0.232	87	
Saturn's Tethys	6.17E+20	0.394	0.145	86	
Saturn's Enceladus	1.08E+20	0.239	0.113	33	145
Saturn's Mimas	3.75E+19	0.159	0.064	77	92
Saturn's Phoebe	8.30E+18	0.102	0.049	75	107
Saturn's Hyperion	5.59E+18	0.074	0.020	93	
Uranus's Titania	3.53E+21	0.773	0.379	60	90
Uranus's Oberon	3.01E+21	0.727	0.346	70	85
Uranus's Ariel	1.35E+21	0.559	0.269	<60	85
Uranus's Umbriel	1.17E+21	0.520	0.200	<75	85
Uranus's Miranda	6.59E+19	0.193	0.079	<60	85
Neptune's Triton	2.14E+22	1.455	0.779	36	42
Neptune's Proteus	4.40E+19	0.170	0.070	<38	51
Neptune's Nereid	2.70E+19	0.156	0.071	50	
Dwarf Planet Pluto	1.30E+22	1.212	0.620	33	55
Pluto's Charon	1.59E+21	0.590	0.288	53	

	Earth Relative Solar Intensity	Solar Constant/Solar Insolation (at Perihelion of planet's orbit, or parent- planet's orbit) (W/m²)	Solar Constant/Solar Insolation (at Aphelion of planet's orbit, or parent- planet's orbit) (W/m²)	Rotation Period for a Solar Day (seconds)	Orbital Period (around Sun or parent Planet) (days)
Earth's Moon	1	1414	1322	2,360,621	27.32
Mercury	6.68	14462	6278	5,067,360	88
Mars	0.431	717	493	88,775	687
Comet 67P	0.0845	890	43	45,940	2355.61
Asteroid 24 Themis	0.1032	183	111	30,147	2027.84
Asteroid & Dwarf Planet Ceres	0.1323	211	156	32,667	1683.15
Asteroid 65 Cybele	0.0865	149	95.2	21,893	2315.04
Jupiter's Ganymede	0.0369	56.4	46.3	618,192	7.16
Jupiter's Callisto	0.0369	56.4	46.3	1,441,930	16.69
Jupiter's Io	0.0369	56.4	46.3	152,842	1.77
Jupiter's Europa	0.0369	56.4	46.3	306,806	3.55
Saturn's Titan	0.011	16.8	13.6	1,377,648	15.95
Saturn's Rhea	0.011	16.8	13.6	390,355	4.52
Saturn's Iapetus	0.011	16.8	13.6	6,853,378	79.32
Saturn's Dione	0.011	16.8	13.6	236,477	2.74
Saturn's Tethys	0.011	16.8	13.6	163,123	1.89
Saturn's Enceladus	0.011	16.8	13.6	118,368	1.37
Saturn's Mimas	0.011	16.8	13.6	81,389	0.94
Saturn's Phoebe	0.011	16.8	13.6	34,560	548
Saturn's Hyperion	0.011	16.8	13.6	chaotic	21.28
Uranus's Titania	0.00272	4.09	3.39	752,198	8.71
Uranus's Oberon	0.00272	4.09	3.39	1,163,203	13.46
Uranus's Ariel	0.00272	4.09	3.39	217,728	2.52
Uranus's Umbriel	0.00272	4.09	3.39	358,042	4.14
Uranus's Miranda	0.00272	4.09	3.39	122,170	1.41
Neptune's Triton	0.00111	1.54	1.49	507,773	5.88
Neptune's Proteus	0.00111	1.54	1.49	96,768	1.12
Neptune's Nereid	0.00111	1.54	1.49	41,738	360.16
Dwarf Planet Pluto	0.00064	1.56	0.56	552,096	90600
Pluto's Charon	0.00064	1.56	0.56	551,837	6.39

9.0 Appendix B: Acronym List

ACES	Advanced Cryogenic Evolved Stage
AoA	Analysis of Alternatives
AST	Office of Commercial Space Transportation
AU	Astronomical Unit
BAA	Broad Area Announcement
BC	Boundary Condition
CAD	Computer-Aided Design
CCDev	Commercial Crew Development program
CDR	Critical Design Review
CDRL	Contract Data Requirements List
CLPS	Commercial Lunar Payload Services
COTS	Commercial Orbital Transportation Services
CRIRSCO	Committee for Mineral Reserves International Reporting Standards
CRS	Commercial Resupply Services
CSM	Colorado School of Mines
DC	District of Columbia
ΔV	Delta V
DEM	Discrete Element Model
DOD	Department of Defense
EDL	Entry, Descent, and Landing
EML1	Earth-Moon Lagrange point number 1
EML2	Earth-Moon Lagrange point number 2
ESA	European Space Agency
FAA	Federal Aviation Administration
FSDD	Full Scope Development and Deployment
FY	Fiscal Year
GEO	See GSO
GPS	Global Positioning System
GPV	General Purpose Vehicle
GSO	Geo-Synchronous Orbit
GTO	Geo-Synchronous Transfer Orbit
HEO	High Earth Orbit

HiRISE	High Resolution Imaging Science Experiment
HLV	Heavy Lift Vehicle
HW	Hardware
IHOP	ISRU-derived water purification and Hydrogen Oxygen Production system
IR&D	Independent Research and Development
IRR	Internal Rate of Return
ISP	Specific Impulse
ISRU	In-Space Resource Utilization
ISS	International Space Station
LAMP	Lyman Alpha Mapping Project
LDA	Lobate Debris Apron
LEO	Low Earth Orbit
LCROSS	Lunar CRater Observation and Sensing Satellite
LH2	Liquid Hydrogen
LHS-1	Lunar Highlands Simulant 1
LN	Liquid Nitrogen
LO2	Liquid Oxygen
LOLA	Lunar Orbiter Laser Altimeter
LRU	Line Replaceable Unit
LTV	Lunar Tanker Vehicle
M2M	Moon to Mars
MEO	Medium Earth Orbit
MESSENGER	MErcury Surface, Space EnviroNment, GeochEmistry and Ranging
MR	Mixture Ratio
MRO	Mars Reconnaissance Orbiter
NASA	National Aeronautics & Space Administration
NextSTEP	Next Space Technologies for Exploration Partnerships
NIAC	NASA Innovative Advanced Concepts
NPV	Net Present Value
Ops	Operations
OTV	Orbital Transfer Vehicle
PDR	Preliminary Design Review
PI	Principal Investigator
PL	Payload

PMDev	Propellant Mining Development
POP	Period Of Performance
PPP	Public Private Partnership
PSR	Permanently Shadowed Region (of the Moon)
PVC	Polyvinyl Chloride
RAM	Reliability, Availability, and Maintainability
R&D	Research and Development
ROS	Return on Sales
SLS	Space Launch System
SpaceX	Space Exploration Technologies Corp.
SRB	Solid Rocket Booster
SSP	Space Solar Power
STEM	Science, Technology, Engineering & Mathematics
STMD	Space Technology Mission Directorate
TBD	To Be Decided
TNO	Trans-Neptunian object
TRL	Technology Readiness Level
TT	Terrain Type
UCF	University of Central Florida
ULA	United Launch Alliance
US	United States
USAF	United States Air Force
USNC	Ultra Safe Nuclear Corporation
WBS	Work Breakdown Structure
wt%	Weight percent
WW%	Water Weight percent
XEUS	eXperimental Evolved Upper Stage